Emulation of Permanent Magnet Machines

Amitkumar Kortagere Sashidhar

A Thesis
in
The Department
of
Electrical and Computer Engineering

Presented in Partial Fulfillment of the Requirements
For the Degree of
D'octor of Philosophy (Electrical and Computer Engineering) at
Concordia University
Montréal, Québec, Canada

March 2020

CONCORDIA UNIVERSITY

SCHOOL OF GRADUATE STUDIES

This is to certify that the thesis prepared

By: Amitkumar Kortagere Sashidhar

Entitled: Emulation of Permanent Magnet Machines

and submitted in partial fulfillment of the requirements for the degree of

D'octor of Philosophy (Electrical and Computer Engineering)

complies with the regulations of this University and meets the accepted standards with respect to originality and quality.

Signed by the final examining committee:

_____ Chair

Dr. Nikolaos Tsantalis

_____ External Examiner

Dr. Brij. N. Singh

_____ External to Program

Dr. Radu G. Zmeureanu

_____ Examiner

Dr. Luiz. A. C. Lopes

_____ Examiner

Dr. Akshay Kumar Rathore

_____ Thesis Supervisor

Dr. Pragasen Pillay

Approved _____

Dr. Yousef R. Shayan, Chair of Department

March 16, 2020 _____

Dr. Amir Asif, Dean,

Gina Cody School of Engineering and Computer Science

ABSTRACT

Emulation of Permanent Magnet Machines

Amitkumar Kortagere Sashidhar, Ph.D.
Concordia University, 2020

Power hardware-in-the-loop (PHIL) based machine emulation is increasingly being recognized as an effective approach for simplifying the testing of electric drive systems. In machine emulation, a power electronic converter emulates the behavior of an electric machine. Since the motor is being emulated, several motor types/ratings, and its corresponding impact on the driving inverter and drive inverter controller can be studied before the actual motor is prototyped (developed). Furthermore, since the machine behavior is emulated, a dynamometer is not required to load the machine and operate it at it's required torque/speed. These two factors, reduce the time to market of the complete drive system significantly, when machine emulation is used. In addition, a machine emulator can also be used to study the response of the driving inverter and it's controller for several transient conditions which are typically avoided when testing on a physical machine, due to fear of equipment damage.

A PHIL based machine emulation is relatively a new technology and therefore there are several open research problems to address. Emulation accuracy is significantly dependent on the details of the machine model used for emulation. Another important research concern is the control strategy for the machine emulator and its interaction with the driving inverter controller. It is necessary to ensure that the machine model detail is not compromised while developing a control strategy for the machine emulator. Validating the developed emulator system for a wide variety of transient drive behavior such as faults, emulation of different machine topologies, etc. is also another important research problem to address.

This PhD research work develops a PHIL based machine emulator system, which uses machine models based on look-up table data, generated from finite element analysis (FEA) tools. The usage of these machine models allows for the emulation of the machine‘s magnetic (eg. saturation) and geometric (eg. cogging-torque) characteristics, thus greatly improving the emulation accuracy and utility. This PhD research work also

develops a control strategy for the machine emulator. The interaction of the emulator control strategy in relation with the driving inverter control strategy is studied and considerations to ensure stable and accurate emulation are proposed. The proposed control strategy developed for the emulator also takes into account the electric drive system transient behavior during the event of driving inverter faults. Experimental setups of the developed emulator systems are used to emulate the behavior of a permanent magnet synchronous machine (PMSM), a variable-flux machine (VFM), an open-winding PM machine. The results obtained from the emulator system are compared with that obtained from a driving inverter feeding a prototype machine to validate the utility and accuracy of the developed emulator systems.

Acknowledgments

No one achieves anything alone! PhD is a journey and the reason I could reach it's destination was due to the help, guidance, motivation and unwavering support of several wonderful people throughout.

I would like to start off by thanking my parents and my brother. My parents and my brother were a constant source of encouragement throughout the course of my PhD. They were cheering for every paper that I published and every stage of my PhD that I passed. This alone was probably one of the biggest sources of motivation for me to try my best and complete my PhD as best I can.

Prof. Pillay gave me an opportunity to pursue my PhD under his supervision for which I will forever be grateful. Apart from his guidance throughout my PhD, I have also learned several other things from him including teaching, preparing reports and presentations, and managing multiple tasks at a time. Prof. Pillay has taught me everything there is to be a good researcher. I am also grateful for the financial support and confidence he has instilled in my during the course of my PhD. I hope to take forward whatever I have learned, all-round from him, into my future as well.

I have a lot of respect and appreciation towards all my PhD committee members, Prof. Lopes, Prof. Rathore and Prof. Zmeureanu. Their questions during the entire course of my PhD journey also significantly helped me shape my thesis. Sincere vote of thanks towards the external examiner Dr. Brij Singh as well.

My desire and drive to do a PhD was due to several wonderful teachers in my masters. They instilled interest in me towards research, and taught me the basics of power and control. I am thankful to all of them, especially, Prof. Narayanan, Prof. Vinod John, and Prof. Nagendra Rao.

I would like to also take this opportunity to thank all my friends in the PEER group. I have learned a great deal from them having had the opportunity to interact with several of them. Special thanks to Sara, Chirag, Gabriel, Rajendra, Mathews, Nazanin and Nazli (and several others whom I might have missed). You did really

make my stay at the PEER lab enjoyable and memorable. I would also like to thank my friends back at India, especially Sudharshan, Saichand and Gopal. Thank you all for being such good friends, mentors and guides. I would also like to take this opportunity to thank all my friends and well wishers at OPAL-RT and ABB as well.

This research work is done as part of NSERC/Hydro-Québec Senior Industrial Research Chair entitled "*Design and Performance of Special Electrical Machines* held by Professor Pragasen Pillay at Concordia University. It is also done as part of the InnovÉÉ/NSERC CRD project entitled "*Emulation and Design of Electric and Hybrid Electric Vehicle Motor Drive Systems*. This project is also supported by OPAL-RT Technologies, Hydro-Qubec and Mentor Infolytica, a Siemens Business. I would like to acknowledge the support of the Natural Sciences & Engineering Research Council of Canada. I would also like to acknowledge the support provided by Fonds de recherche du Québec - Nature et technologies (FRQNT).

Finally, I would like to dedicate my PhD to my mom. I know my mom is brimming with pride wherever she is. Her pride is probably what I have always strived for during my PhD, and will continue to do so throughout my life.

Contents

List of Figures

Chapter 1

Introduction

Electric Vehicles (EVs) are seeing a rise in their popularity over the last 30 years. Several reasons for these include environmental concerns, increased efficiency, better performance, etc. [1–7]. The electric traction drive is the most important component of an EV. A significant amount of work has been done on the design, analysis, and testing of electric traction drives systems [1–10]. In the traction drive of an EV, the type of motor used can depend on various factors relating to power density, efficiency, torque/ power and cost. In addition, several motor designs are custom made depending on the manufacturer and specific application needs [1–5, 8–10]. The driving inverter in an EV can be of different configurations as well. This again depends on the motor topology used, overall cost, reliability and availability of the driving inverter semiconductor devices [1–10]. Due to these reasons and for reasons of safety, testing of the electric traction drive in an EV is extremely important. Several exhaustive tests are therefore needed prior to the commissioning of an electric traction drive system. During these tests, the motor design, the drive inverter and the drive controller, along with its interaction with the other subsystems of the EV, are tested [1–10]

The conventional process of the electric drive system testing is shown in Fig. 1.1. Typically the drive inverter, the test machine and the drive inverter controller are all made from different manufacturers [1–3, 6]. Therefore, testing of the complete drive system is possible only after all the individual components are manufactured and ready. The drive inverter and the drive inverter controller are fairly standardized and/or modularized. However, the test machine of the drive system is custom made and takes a longer time to manufacture. Therefore in several cases, the testing of the complete electric drive system is delayed due to delays in the test machine development [11–13]. In addition, the conventional process of electric drive system testing is also severely

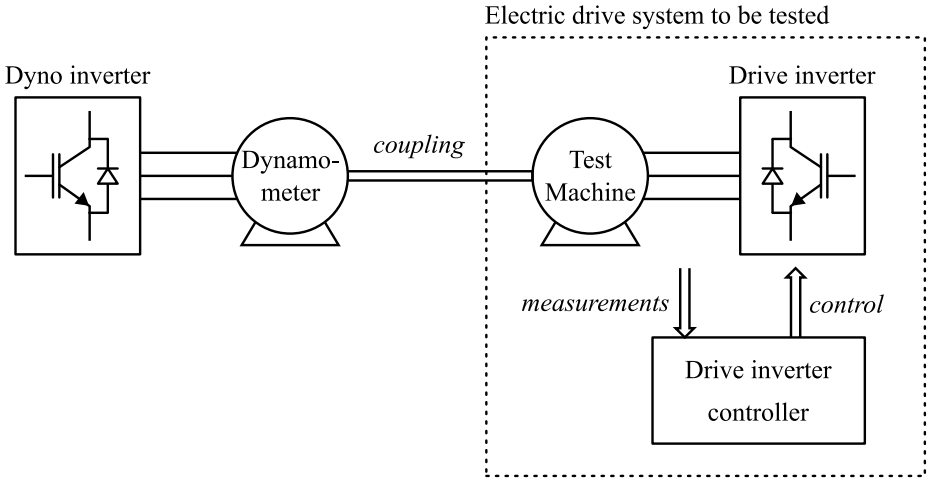

Fig. 1.1: Schematic illustrating the conventional drive system testing methodology.

restricted by the dynamometer (used to load the electric drive system) rating and capability. Typically a standard dynamometer might be used, which might not be rated to the same specifications (load torque and speed) as the test machine. In such a case, it might not be possible to test the electric drive system to its complete range and specifications [13]. With the conventional electric drive system testing methodology, testing the electric drive system for severe transient conditions is often avoided due to fear of equipment damage. Moreover, it might not be practical to introduce faults in the machine or the inverter just for the process of testing.

Power hardware-in-the-loop (PHIL) machine emulation is a testing methodology which is increasingly being recognized as an effective approach for simplifying the testing of electric drive systems [11–30]. In a PHIL based machine emulation system, a set of power converters, termed *the machine emulator*, is controlled in a manner so as to mimic machine behavior. This control of *the machine emulator* is achieved with the help of a detailed machine model running on a real-time controller. A schematic of this system is shown in Fig. 1.2. Details regarding the converter structure for the machine emulator will be discussed over the course of this thesis. With such a PHIL based machine emulator setup, assuming the availability of a detailed machine model, several machines types and ratings can be emulated. There are several works related to the emulation of an induction motor [11, 13, 14, 16, 18–20], a permanent magnet synchronous machine [12,15,17,24,26,28–30] and a switched reluctance machine [25]. A machine emulator system offers several benefits as compared to conventional approach to electric drive system testing [11–30].

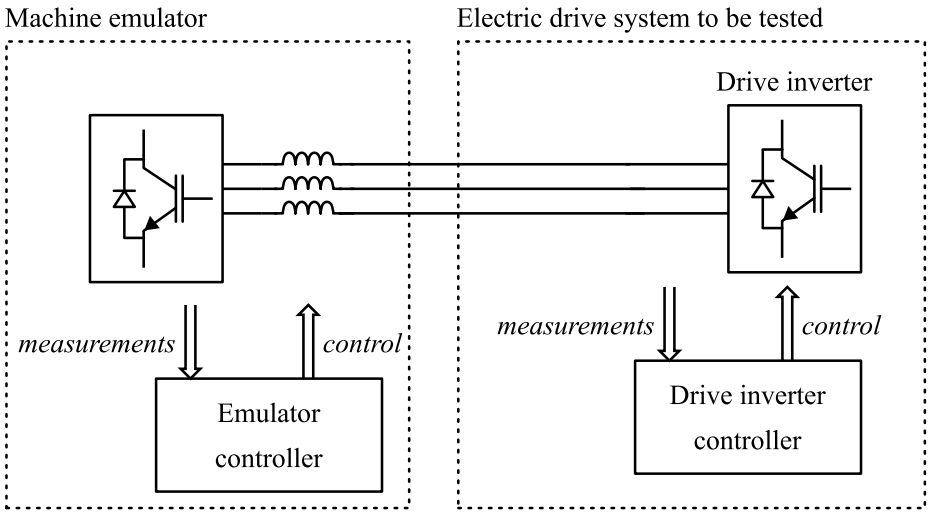

Fig. 1.2: Schematic illustrating the use of a machine emulator for electric drive system testing.

- Since the machine is being emulated, several motor types/ ratings, and its corresponding impact on the driving inverter, and controller can be studied before the actual machine is developed (prototyped), thus reducing the time to market of the electric drive system significantly.

- There is no requirement of a dynamometer test bench to load the machine. A load torque can be applied to the machine model being used in the machine emulator system. Thus, the driving inverter will supply currents to the emulator, similar to that when connected to a prototype machine coupled to a dynamometer. Hence, the driving inverter and controller testing can ensue without the need of a dynamometer arrangement.

- With the emulator system, testing of the driving inverter and controller can be done for severe transient conditions such as faults. Since the machine is emulated, the chance of equipment damage is reduced. Furthermore, machine faults can be easily modeled on an emulated machine. If the conventional method of electric drive system testing were to be used, faults would need to be physically introduced on the test machine. Introducing some faults would mean willfully damaging the machine just for the purpose of testing.

1.1 Research problems in machine emulation

Power-hardware-in-the-loop (PHIL) based machine emulation is a relatively new area of research with several open problems which need be addressed. Addressing these problems would make PHIL based machine emulation an acceptable mode of testing electric drive systems. These open research problem are listed below.

1.1.1 Machine model accuracy

As mentioned earlier, the emulator is controlled to mimic a modeled machine behavior. The motor model used for performing the emulation is implemented on a digital controller, which in several cases is a real-time simulator [11–30]. The detail associated with this motor model is one of the important factors that defines the accuracy of the machine emulation. There has been a lot of work towards simplifying these machine models to allow for a real-time implementation and emulation [11–17, 20, 31–34]. Such simplified models are suitable for steady state emulation but cannot be used to emulate various machine transient conditions such as start-up, saturation, and faults. Emulation of special machines such as a permanent magnet synchronous machine (PMSM) further demands a higher accuracy of machine models. There have been attempts to introduce saturation effects in machine models of PMSMs by utilizing flux/ inductance lookup tables [12, 15]. However, there is still a certain degree of simplification involved in these models as well, to allow for real-time implementation and subsequent use for emulation. There are detailed machine models available in literature [35–39], but such models haven't been used for PHIL based machine emulation. Therefore, there is a need to develop an emulator system using a detailed machine model, which can account for the variation of machine parameters with respect to winding currents and rotor position.

1.1.2 Emulator and test inverter control interaction

An important consideration while performing machine emulation is the control methodology used for the machine emulator. There has been a significant amount of work addressing the issue of emulator control [11–16, 19, 20, 35]. The driving inverter typically works in current control mode [12–16, 30]. Additionally, it is easier to control the machine emulator to directly mimic machine currents, by operating it in current control mode as well [11, 30]. But both converters simultaneously operating in current

control mode has been reported to lead to a control conflict [12–16].

References [11–16, 20, 35] try to address this control conflict in different ways, but each with its own limitations. References [12, 14–16] modify and simplify the machine model to avoid this control conflict. The use of a simplified model for the purpose of emulation reduces the emulation accuracy significantly. Reference [13] tries to maintain the machine model accuracy to a certain extent, but uses a more complicated control methodology for the machine emulator. The filter element connecting the driving inverter and the machine emulator is termed as a coupling element. [13] uses a complicated filter arrangement, as a coupling element, to connect the machine emulator and the driving inverter (test-inverter). Such an approach has several concerns; (i) reduced emulation bandwidth and hence accuracy, (ii) possibility of LC oscillations in the coupling filter arrangement leading to stability issues, and (iii) additional losses in the coupling filter damping resistances leading to a reduced emulator system efficiency.

Therefore, there is a necessity to develop a machine emulator system which does not compromise on the machine model accuracy, uses a simple coupling element connecting the emulator and the driving inverter, and a simple control strategy for the machine emulator. Furthermore, it is important to investigate that the developed machine emulator control does not influence the driving inverter control.

1.1.3 Power converter topology for a machine emulator

The machine emulator is essentially a set of power converters controlled in a manner to mimic machine behavior. The accuracy of machine emulation, apart from being dependent on the machine model being used, is also dependent on the power converter topology used for the machine emulator along with its control. Some works use a standard two-level voltage source converter (VSC) based topology for its machine emulator [11, 13, 30]. There are some papers which use interleaved pulse width modulation (PWM) with multiple inverter legs to achieve a higher switching frequency and hence a higher emulation bandwidth [12, 14–16]. There are other emulator topologies which are built solely with linear amplifiers [40].

Identification of an appropriate power converter topology for the machine emulator, along with its control optimization is another research problem in the area of machine emulation.

1.1.4 Transient studies with the machine emulator system

Most available literature perform emulation of machine behavior for transient conditions such as start-up, speed-reversal, load torque change, etc [11–17, 20, 31–34]. The ability to emulate such transient conditions does test the utility of the machine emulator system to a certain extent. However, there are several other drive transient conditions such as driving inverter faults and emulated machine faults which are also equally important [41–44]. To harness the capabilities of the emulator system completely, it is necessary that the developed emulator system is capable of emulating such severe transient conditions as well.

There is no reported literature pertaining to the emulation of machine behavior for driving inverter faults nor for the emulation of faulted machines. These areas are hence an important topic of research to prove the utility of an emulator system.

1.1.5 Emulation of open-winding PM machines

Open-winding permanent magnet (PM) machines have several advantages over conventional PM machines, such as, operation over a wider speed range, independent phase current control and fault tolerance [3, 45–48]. Due to these advantages, open-winding PM machines are gaining popularity for transportation applications and several other drive systems. Machine emulation can help expedite the process of testing these novel motor topologies as well.

In an open-winding machine all three phases of the machine can be independently controlled [3,45–48]. This would mean that the driving inverter topology used for open-winding PM machines would be different as compared to those used for conventional machines. Furthermore, modifications will be required for the emulator topology and the emulator control strategy as well. There is no reported literature on the emulation of open-winding machine and hence emulation of the same is an important research problem to address as well.

1.2 Objectives

The previous section presented several open research problems in the field of machine emulation. The objective of this PhD research work and the problems that will be addressed as part of this research work are as follows:

a. Development of machine emulator setups:

This PhD research work will aim to develop multiple machine emulator setups built with different power converter topologies. Two topologies for the machine emulator are targeted; (i) a two-level VSC based, and (ii) a linear amplifier based. A new topology built in collaboration with another PhD student, which is a combination of (i) and (ii) will also be presented in this thesis. With the various emulator setups built, investigation can be performed on the emulation of different types of machines, various emulator control strategies, etc.

b. Investigation on emulator control:

Most emulator system control techniques have several issues as mentioned briefly in the previous section. This PhD research will aim to develop a control strategy which addresses the drawbacks of the existing control schemes. The objective is to maintain control simplicity and maximize emulation bandwidth (which translates to maximization of emulation accuracy).

c. Ensuring machine model accuracy:

Machine model accuracy directly translates to machine emulation accuracy. Most PM models used for emulation have some sort of simplification to ease their implementation. This PhD research will look into using existing FEA look-up table based PM machine models for the purpose of machine emulation. Due to use of these detailed machine models, the machine emulator developed would be capable of representing machine behavior due to its magnetic and geometric characteristics.

d. Emulation of machine behavior for severe transients:

The developed machine emulator system in this PhD work, will be used to study machine emulation for severe transient conditions such as driving inverter faults. Modifications to the emulator controller will be proposed to ensure accurate emulation. Furthermore, modifications will also be proposed to the emulator control structure to ensure emulation system safety for these severe transient conditions.

e. Emulation of an open-winding PM machine:

Emulation of open-winding machines have not been reported in literature. This PhD research work will also investigate the emulation of an open-winding PM machine. Modifications will be proposed for the emulator structure to allow

emulation. A novel controller will be proposed to ensure independent control for each of the emulated windings of the open-winding PM machine

1.3 Contributions

The contributions of this PhD research work are summarized below.

- Development of a two-level VSC based machine emulator system.
- Development of a linear amplifier based machine emulator system.
- Investigation of a machine emulator control strategy.
- Emulation of different types of machines, such as, IMs, PMSMs, and VFMs. Emulation of various drive transient conditions.
- Development of a hybrid power amplifier based machine emulator setup (in collaboration with another student).
- Development of a PMSG machine emulator setup (in collaboration with another student).

Journal Papers:

- L. M. Kunzler, **K. S. Amitkumar**, L. A. C. Lopes, P. Pillay and J Bélanger, "Hybrid Linear-Switched Power Amplifier and Control Strategy for Machine Emulation", *in IEEE Transactions on Industrial Electronics* - Under review.
- **K. S. Amitkumar**, P. Pillay and J. Bélanger, "Hardware-in-the-loop Simulations of Inverter Faults in an Electric Drive System for Transportation Applications", *in IEEE Transactions on Transportation Electrification* - Under review.
- **K. S. Amitkumar**, R. Thike and P. Pillay, "Linear Amplifier-Based Power-Hardware-in-the-Loop Emulation of a Variable Flux Machine," *in IEEE Transactions on Industry Applications*, vol. 55, no. 5, pp. 4624-4632, Sept.-Oct. 2019.
- **K. S. Amitkumar**, R. S. Kaarthik and P. Pillay, "A Versatile Power-Hardware-in-the-Loop-Based Emulator for Rapid Testing of Transportation Electric Drives," *in IEEE Transactions on Transportation Electrification*, vol. 4, no. 4, pp. 901-911, Dec. 2018.

- M. A. Masadeh, **K. S. Amitkumar** and P. Pillay, "Power Electronic Converter-Based Induction Motor Emulator Including Main and Leakage Flux Saturation," *in IEEE Transactions on Transportation Electrification*, vol. 4, no. 2, pp. 483-493, June 2018.

- R. S. Kaarthik, **K. S. Amitkumar** and P. Pillay, "Emulation of a Permanent-Magnet Synchronous Generator in Real-Time Using Power Hardware-in-the-Loop," *in IEEE Transactions on Transportation Electrification*, vol. 4, no. 2, pp. 474-482, June 2018.

Conference Papers:

- **K. S. Amitkumar**, P. Pillay and J. Bélanger, "Hardware-in-the-loop Simulations of Inverter Faults in an Electric Drive System," *in IEEE ECCE-2019*, Baltimore, MD, USA, 2019, pp. 353-358.

- **K. S. Amitkumar** and P. Pillay, "Independent Phase Current Control of a Permanent Magnet Motor," *in International Conference on Power Electronics, Drives and Energy Systems (PEDES) 2018*, Chennai, India, 2018, pp. 1-6.

- **K. S. Amitkumar**, R. Thike and P. Pillay, "Power-Hardware-in-the-Loop Based Emulation of a Variable Flux Machine," *in IEEE ECCE-2018*, Portland, OR, 2018, pp. 6454-6460.

- **K. S. Amitkumar**, R. S. Kaarthik and P. Pillay, "A versatile power-hardware-in-the-loop based emulator for rapid testing of electric drives," *in IEEE ECCE-2017*, Cincinnati, OH, 2017, pp. 5468-5474.

1.4 Organization of this thesis

Chapter 2 presents a two-level VSC based machine emulator system. The proposed control for the machine emulator system is first introduced here. Experimental results are presented for the emulation of a PMSM.

Chapter 3 presents a linear amplifier based machine emulator system. The objective is to attain the highest closed loop bandwidth possible. Implementation aspects to achieve the same is presented in this chapter. Experimental results are presented for the emulation of a VFM.

Chapter 4 next presents the emulation of the machine behavior for driving inverter gate-drive failure faults. Modifications are proposed for the emulator control structure and control type. These modifications ensure an accurate emulation and safety of the emulator system and the driving inverter. Experimental results are presented for the emulation of a PMSM in the event of driving inverter faults.

Chapter 5 presents the emulation of an open-wining PM machine. Modifications are proposed to the emulator structure to enable emulation of an open-winding machine. A current control is also proposed for the driving inverter and the emulator to allow emulation of various current harmonics in the emulated machine currents.

Chapter 6 presents two works done in collaboration with other PhD students. The development of a hybrid emulator setup to emulate an IM and the emulation of a PMSG is presented in this chapter.

Chapter 7 presents the conclusion of this thesis and possible future works.

Chapter 2

Development of the machine emulator test-bench

Machine emulation is a testing methodology in which the driving inverter and the controller of an electric drive system are tested, prior to the development of the electrical machine. This chapter presents the methodology followed to develop the machine emulator system. Experimental results obtained for the emulation of a surface-mounted PMSM are also presented in this chapter.

2.1 Overview of the machine emulator structure

A schematic of the proposed power hardware-in-the-loop (PHIL) based machine emulator is presented in Fig. 2.1. The active front-end converter (AFEC) and the emulating converter together act as a four-quadrant power amplifier. This is needed to allow an emulation of both motoring and generating modes of operation. The power converter topologies used for the AFEC stage and the emulating converter stage are standard two-level six switch voltage source converters (VSCs) [11, 13, 14, 16, 20, 24].

The objective of the AFEC control is to maintain the DC link voltage of the emulator at a constant value. The controller design for the AFEC is not discussed here, as it is quite well established [49]. The AFEC control should be as fast as possible to ensure that the emulating converter is also able to achieve its desired response. The semiconductor devices used within the two-level VSCs of the emulator system have switching frequency of 20 kHz. The switching frequency and a phase reactor of 1 mH being used for the AFEC, leads to a design with a current loop bandwidth of around 1.5 kHz and a DC link voltage loop control bandwidth of around 300 Hz. Details

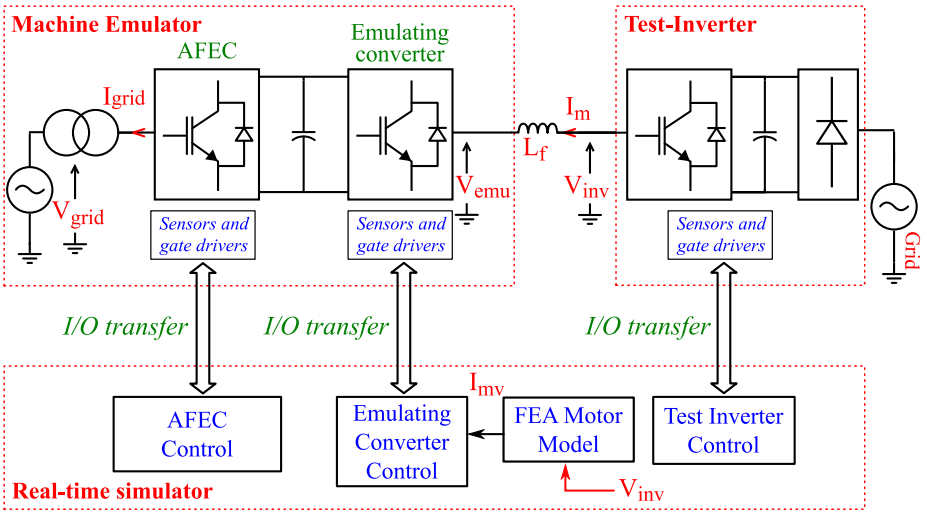

Fig. 2.1: Schematic of the proposed PHIL based machine emulator system.

regarding the control structure and the exact controller gains used for AFEC control, can be obtained using the expressions presented in [49].

The objective of the emulating converter (as indicated in Fig. 2.1) is to draw currents from the test inverter, as specified by the simulated machine model on the real-time simulator; indicated as 'FEA Motor Model' in Fig. 2.1. This simulated motor model is fed by the the test-inverter output voltage, marked as V_{inv} (in Fig. 2.1). Further, as will be explained in Section 2.2, the FEA motor model contains the machine geometric and magnetic data. Therefore, the currents generated by this motor model, indicated by I_{mv} (in Fig. 2.1), would be an accurate representation of the actual physical machine when designed using the same FEA data.

If the test inverter and the machine emulator are connected to the same three phase supply, a transformer (as indicated in Fig. 2.1), will be needed to prevent common-mode currents or circulating currents from flowing in the power converter assembly. As shown in Fig. 2.1, for the system implemented, the control for the AFEC, the emulating converter and the test inverter are implemented on the same real-time simulator platform, OP4510 [50]; however, the test inverter control does not interact with the machine emulator controller.

2.2 System description

2.2.1 Control methodology

With reference to Fig. 4.1, the machine emulator has two back-to-back converters; one which acts as an AFEC and the other which acts as an emulating converter. The machine emulator is connected to the test-inverter. Typically the test-inverter works in current control mode [12–16]. Emulating converter control has also been discussed to some extent in [11–15].

Most detailed machine models implemented in real-time are voltage-fed current-out models; they take voltage as inputs and output the machine current drawn [31, 35–37]. When such models are used for emulation purposes, the ease of current control for the emulating converter is evident. However, as stated earlier, the test-inverter works in current control mode as well. Both the converters, the test-inverter and the emulating converter working in current control mode, could possibly lead to control oscillations, thus jeopardizing the stability of the entire emulation system [12, 14, 15].

There are two ways in which this challenge is addressed in the literature, with certain limitations. (i) [13] uses a voltage-fed current-out model, with an LCL coupling filter arrangement. Having an LCL filter would allow voltage control mode of the emulating converter, thus resolving the control interaction issue, mentioned earlier [13]. There is however a challenge associated with generating this voltage reference. Additionally, the complication in the emulator control reduces the emulation bandwidth, which in turn reduces the emulation accuracy significantly. Furthermore, the LCL filter arrangement also adds several other challenges to the emulation system such as, LCL resonance, and requirement of damping resistances which will reduce the system efficiency. (ii) References [12, 14–16], on the other hand use an inverted machine model, which is a current-in voltage-out model. This means for every line current drawn by the machine model, a corresponding terminal voltage of the machine model can be obtained, and this voltage can further serve as a reference for the emulating converter voltage control. This again resolves the control interaction issue mentioned earlier. The inverted machine model as discussed in [12, 14–16] is an approximate model. This model does not contain all details related to the machine geometry and magnetics that can be obtained from FEA software. Hence, the emulation that would be performed with these approximate machine models would also be of a lower accuracy.

For the emulator system proposed as part of this research work, a voltage-in current-out model (presented in [35–38]) is used. This machine model, as will be explained

further in Section 2.2.2 contains information relating to the machine magnetic and geometric characteristics, obtained beforehand in the form of look-up tables. Since the proposed emulation system uses this machine model, the resulting emulation performed would have a high degree of accuracy as well. Furthermore, a simple L-filter is used to connect the machine emulator and the test-inverter. Unlike [11–15] a simple current control methodology is used for the emulating converter of the proposed machine emulator system. Section 2.2.3 explains the design methodology and analysis associated with both converters working in current control mode in tandem. Control oscillations are avoided by making the current control of the emulating converter much faster than the current control of the test-inverter. The simple current control methodology with the L-filter allows for a simple practical realization for the proposed emulation system. Additionally, the use of detailed machine models leads to an accurate emulation as well.

2.2.2 Machine model for the proposed emulator

Machine parameters for a PMSM, depends on winding currents and the rotor's position. Detailed nonlinear look-up table based machine models which can account for these dependencies have been proposed in literature [35–38], and can be implemented on a real-time simulator to perform accurate machine simulations. Implementation details of the same for CHIL simulations are presented in [35–38], however there is no reported literature pertaining to the use of these detailed look-up tables based models for PHIL simulations such as machine emulation.

Emulation accuracy depends on the accuracy of the machine model used. Hence to perform an accurate emulation, this PhD work uses the machine models presented in [35–38] for the purpose of machine emulation. These models are voltage-in current-out based and hence output currents for a given applied voltage to the model. Thus an emulator system when using this machine model would need to operate in current control mode as well. This is discussed in detail in Section 2.2.3. The mathematical behavior of these models is defined in (1).

$$\mathbf{I}(t+\Delta t) = \mathbf{L}_{inc}(\theta, \mathbf{I})^{-1} \left(\int_{t=0}^{t+\Delta t} (\mathbf{V}(t^{'}) - R\, \mathbf{I}(t^{'}))dt^{'} - \mathbf{\Phi}(\theta, \mathbf{I}) \right) \tag{1}$$

where θ is the rotor position, $\mathbf{I} = (I_a, I_b, I_c)$ is the output current vector, $\mathbf{V} = (V_a, V_b, V_c)$ is the voltage vector R is the phase resistance, $\mathbf{\Phi}(\theta, \mathbf{I})$ is the vector of the magnet flux linking each phase defined as a function of the rotor position and the

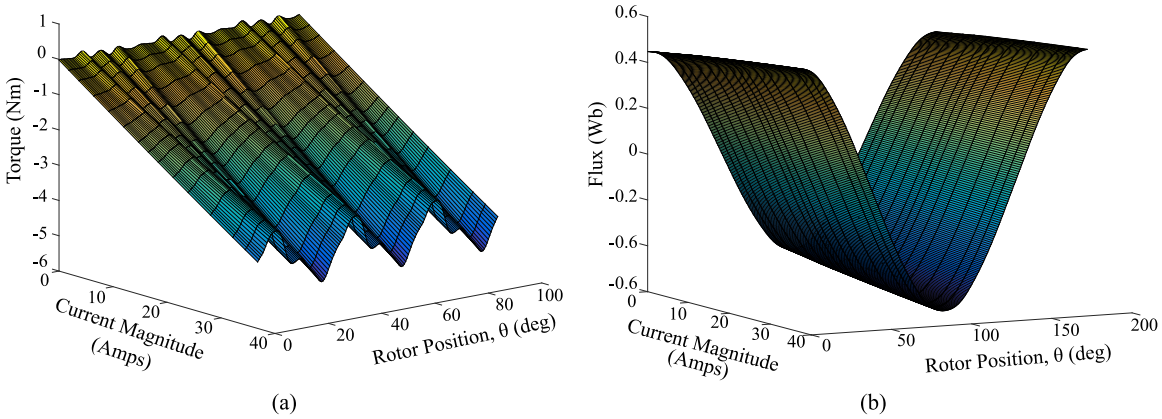

Fig. 2.2: (a) Torque look-up table generated from MotorSolve®; contains information relating to variation of generated torque for change of rotor position (θ) and current magnitude, at a fixed value of advance angle (β); and (b) Phase flux-linkage look-up table generated from MotorSolve®; contains information relating to variation of phase flux-linkage for change of rotor position (θ) and current magnitude, at a fixed value of advance angle (β)

current vector, and $\mathbf{L}_{inc}(\theta, \mathbf{I})$ is the incremental inductance vector.

This chapter presents the emulation of a surface mounted PMSM. The design associated with a prototype surface-mounted PMSM, was initially performed in MotorSolve®, and was subsequently used to generate the machine torque and flux tables [36]. The look-up tables for the machine torque and phase-flux linkages are shown in Fig. 2.2.These look-up tables are defined for a variation of the current magnitude, current advance angle β (only one advance angle is shown in the figures), and the rotor position θ. This look-up table is directly read by the machine model, ensuring detailed modeling of a variety of machine characteristics such as saturation, slot harmonics, and spacial torque ripple (cogging torque).

2.2.3 Proposed control design

The control methodology used is a simple current control technique which allows a simple realization of the emulation system. As mentioned earlier the control for the AFEC is well established [49] and will not be discussed here. The control structures of the emulating converter and the test-inverter are shown in Fig. 2.3. From Fig. 2.3(b) and Fig. 2.3(c), it is evident that both the converters are operating in current control mode. An inference can be made from the figure that there is only one independent current reference ($I^*_{m\_q}$ and $I^*_{m\_d}$) for the current control of both converters. The

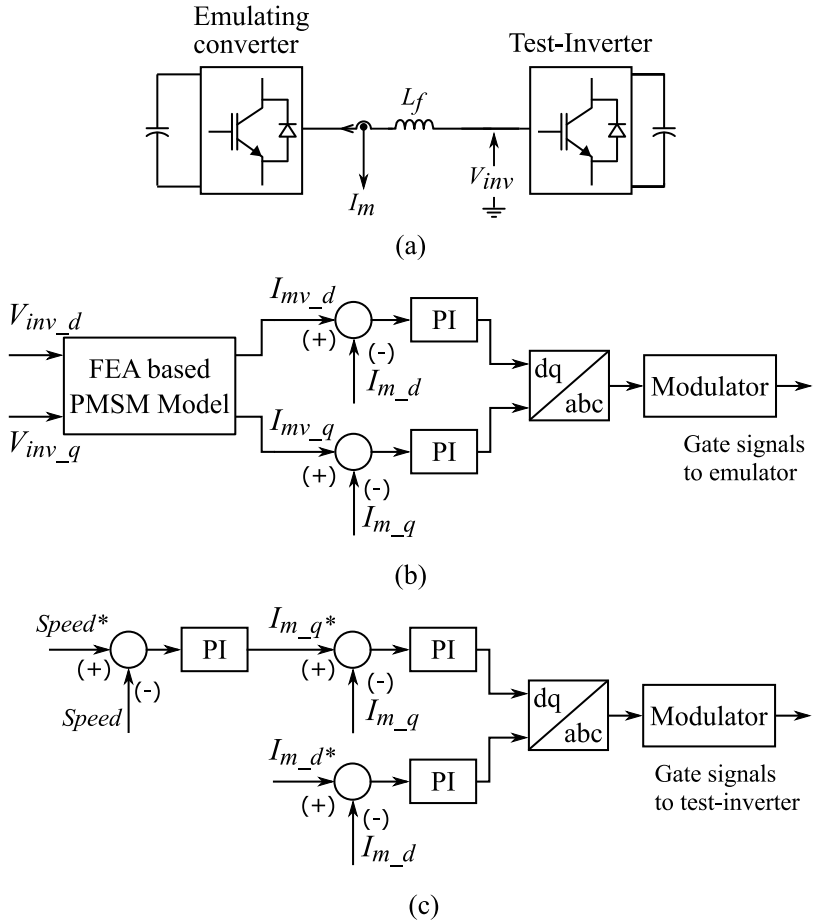

Fig. 2.3: (a) Emulating converter and the test-inverter with the sensed variables for control, (b) control scheme for the emulating converter, (c) control scheme for the test-inverter.

emulating converter current control references (I_{mv_q} and I_{mv_d}) are derived based on the FEA PMSM model; which is driven by the test-inverter measured voltages (V_{inv_q} and V_{inv_d}); which is again obtained as a result of the test-inverter current control action. This will be further elaborated upon in this section. However, at this stage, it can be reasoned that the emulating converter needs to have a higher current loop bandwidth compared to the test-inverter current loop bandwidth. This ensures the machine emulator dynamics to stabilize before a new reference set-point change from the test-inverter current control. This is the crux of the proposed control scheme for the emulation system. The design calculations that follow, along with real-time simulations in the subsequent section, show the validity of the proposed control methodology.

The first step of the control design exercise is to design the emulating converter

current loop. This current controller is designed to have the highest possible bandwidth for the designed emulation system. The voltage equations for the d-axis and the q-axis are given as shown in (2) and (3). These equations show that the *plant* model is essentially the coupling inductance used, L_f with the feed-forward terms and cross-coupling terms added.

$$-V_{emu\_d} = Ri_d + L\frac{di_d}{dt} - \omega L i_q - V_{inv\_d} \tag{2}$$

$$-V_{emu\_q} = Ri_q + L\frac{di_q}{dt} + \omega L i_d - V_{inv\_q} \tag{3}$$

The control block diagram for the d-axis emulating converter current control is shown in Fig. 2.4. The feed-forward terms are subtracted so as to ensure that the current loop has a first order response as defined by the coupling inductance, L_f.The AFEC is controlled to maintain the DC link voltage of 350 V, which yields a DC link voltage gain, $G = 175$. The inverter switching frequency is 20 kHz. Therefore, the value of T_d, which corresponds to half the switching period of the inverter, is 25 μs. A simple first order filter approximation is used for the current sensor with a gain of unity and a time constant $T_{fi} = 20$ μs. Furthermore, the sampling time of the digital controller T_s is 20 μs. R_f and L_f correspond to the resistance and inductance of the L-filter, considered 300 $m\Omega$ and 3 mH, respectively.

The *PI* controller zero is positioned to cancel the L-filter pole, since this is the slowest pole. The closed loop transfer function of the emulating converter current loop, subsequent to this pole zero cancellation, can be derived as shown in (4). This is a simplified second order transfer function representation of the emulating converter current loop.

$$\frac{I_{m\_d}}{I_{mv\_d}} = \frac{\frac{K_i\, G\, (1+s\, T_{fi})}{R_f\, (T_d+T_s+T_{fi})}}{s^2 + \frac{s}{T_d+T_s+T_{fi}} + \frac{K_i G}{R_f (T_d+T_s+T_{fi})}} \tag{4}$$

Equation (4) can then be compared with a standard second order transfer function. This gives (5), which can be used to calculate the bandwidth of the system for a desired damping, say a critically damped response (ζ =0.707).

$$2\,\zeta\,\omega_n = \frac{1}{T_d + T_s + T_{fi}} \tag{5}$$

For the known values of T_d, T_s, and T_{fi}, the bandwidth of the system is calculated

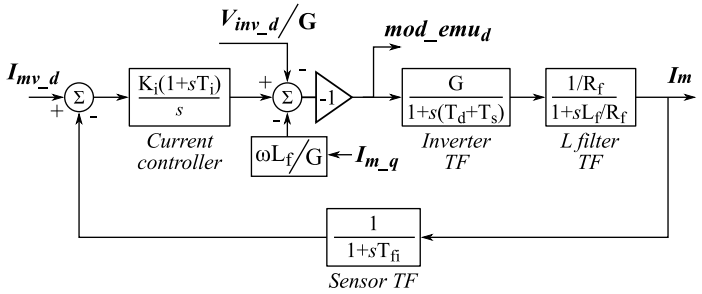

Fig. 2.4: Block diagram of the emulating converter current loop.

to be around 1800 Hz. This is the fastest current loop bandwidth possible for the current emulation system specifications, for a critically damped response case. It is possible to improve the response to a certain extent by reducing the damping, but is not attempted here. The bandwidth of 1800 Hz for the current controller leads to the following choice of the controller gains for the emulating converter; $K_i = 14$ and $T_i = 0.01$.

Fig. 2.4 shows that the current reference for the emulating converter is the current drawn by the virtual FEA machine model (Fig. 2.3(c)). Furthermore as mentioned earlier, the inputs for this FEA machine model are the test-inverter voltages which are generated due to the test-inverter current control. It can therefore be reasoned that the emulating converter current loop is a nested loop within the test-inverter current loop. This nested loop structure is shown in Fig. 2.5. The PMSM transfer function has been approximated as a first order transfer function with L_s signifying the mean value of the machine stator inductance for the purpose of controller design.

After the design of the emulating converter current controller, this control loop (shown in a dotted boundary in Fig. 2.5(a)) can be reduced to a simple first order transfer function. The time constant of this transfer function, τ, is basically representative of the designed emulating converter bandwidth of 1800 Hz. For the design exercise presented here, $\tau = 84.5\mu$s. Thus, the test-inverter current loop can further be reduced to Fig. 2.5(b). The inverter approximation and all other associated delays remain the same as that of the emulating converter. In the PMSM transfer function, the values of R_s and L_s are 0.1718 Ω and 3.4 mH respectively. Based on these values the test-inverter current controller gains, K_{mi} and T_{mi}, can be computed.

The test-inverter current controller gains, are computed based on the magnitude and phase plots of the test-inverter inner current loop shown in Fig. 2.6. This bode plot brings about an important conclusion of this design exercise. The test-inverter

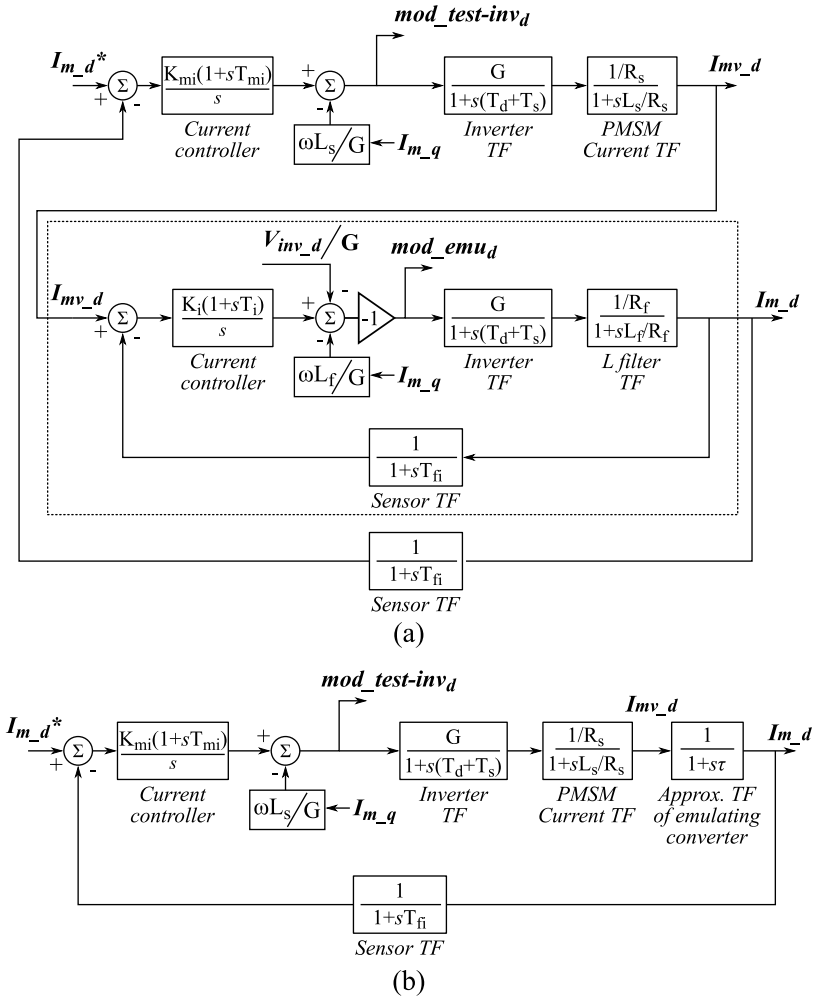

Fig. 2.5: (a) cascaded emulating converter current control loop within the test-inverter current control loop (b) first order transfer function approximation of the emulating converter current control loop within the test-inverter current control loop.

current loop bandwidth needs to be a few times lower than the emulating converter current control bandwidth to ensure a positive gain margin and thus stability. The test-inverter having a current loop bandwidth, four times smaller than the emulating converter current loop bandwidth, yields controller gains $K_{mi} = 5$ and $T_{mi} = 0.013$.

This design exercise proved the viability of the emulating converter current control proposed in this chapter. Real-time simulation results will be presented in Section 2.3 to validate the proposed control and the calculated controller gains. Section 2.3 will also present an analysis of the ratio between the test-inverter current control bandwidth to the emulating converter current loop bandwidth and its impact on emulation.

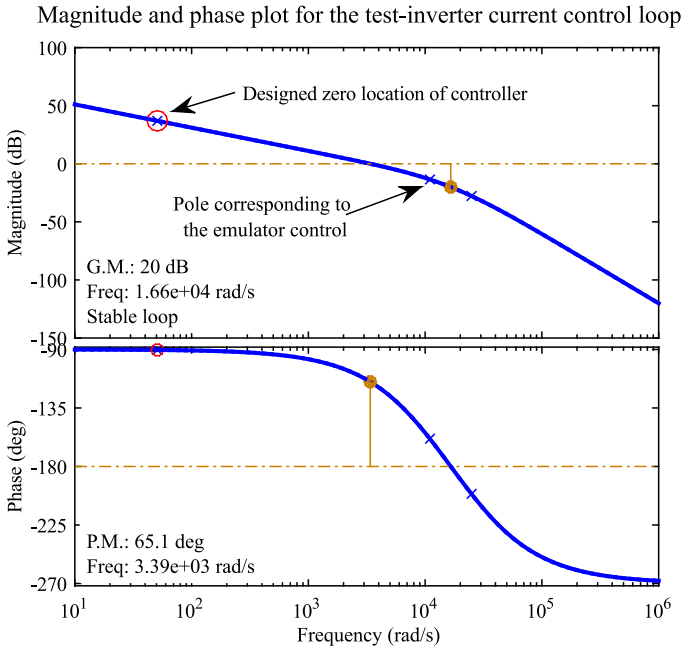

Fig. 2.6: Magnitude and phase plot of the test-inverter current loop.

2.2.4 Coupling filter (*L*-filter) design

The primary reason for choosing an inductance for the coupling filter is the resulting simplicity of the emulation system. The value of the coupling filter inductance has a bearing on the bandwidth of the machine emulator system. A large value of inductance would limit the emulation bandwidth, thus reducing the emulation accuracy as well. A small value of inductance on the other hand would lead to a large ripple current in the emulated current waveform, again reducing the emulation accuracy.

Taking into consideration the resulting current ripple during machine emulation, the coupling inductance value is close to the machine mean inductance. This would ensure that the ripple current drawn by the emulator is also close to the ripple current drawn by the physical prototype machine. However, the current control proposed for the emulator does not require this condition to be met. If the coupling filter inductance is not equal to the machine mean inductance, then except the ripple current, all lower order harmonics (including fundamental) would still match between the emulated machine and the prototype machine.

Another factor which drives the choice of the coupling inductance value is the resulting voltage rating of the emulator. Looking at Fig.2.1 it is clear that the voltage rating of the emulating converter is influenced by the choice of the coupling inductance.

Having a larger value of the coupling inductance than the machine mean inductance, would lead to a smaller voltage rating of the emulating converter in motoring mode but a larger voltage rating in generating (or braking mode). Therefore for the PMSM emulator presented here, from an emulator voltage rating perspective as well, it is optimal to choose a value of the coupling inductance close to the machine mean inductance value.

In a surface mounted PMSM the d-axis and the q-axis inductance are equal, therefore the coupling inductance value can be easily chosen. If the machine emulated is an interior PMSM or an inset PMSM, the values of the d-axis and the q-axis inductances are not equal. In such cases the L-filter value can be chosen to be an average of the d-axis and the q-axis inductances. This would again be an ideal choice for the coupling filter inductance to obtain a good comparison between the emulated current waveforms and the physical machine current waveforms.

2.2.5 Implementation aspects

This section presents some of the implementation aspects associated with both the real-time simulations presented in Section 2.3 and the experimental implementation described in Section 2.4.

A. Terminal voltage sensing of the driving inverter:
   Sensing of the switching voltage at the terminals of the inverter is a concern. The machine model look-up tables have various aspects pertaining to its geometry and magnetics modeled, hence the emulator could draw several lower order harmonics. Placing filters might add phase delays to these harmonics and subsequently compromise the accuracy of machine emulation. Therefore in this implementation, the terminal voltages are directly sensed by voltage sensors which have a high bandwidth of 100 kHz [51]. Additional filters are not added and the sensed switching voltages (V_{inv_q} and V_{inv_d}) are directly fed to the FEA machine model within the real-time simulator (RTS) environment. The FEA machine model is implemented on the FPGA of the real-time simulator and the measured voltages are directly transferred to the machine model within the FPGA. The sampling time of the sensed voltages due to the ADC card sampling is 2.5 μs [50]. Since the sensor bandwidth is quite high and since the sensed voltages are directly transferred to the machine model on the FPGA, the concern associated with switching voltage sensing is reduced. The accuracy with

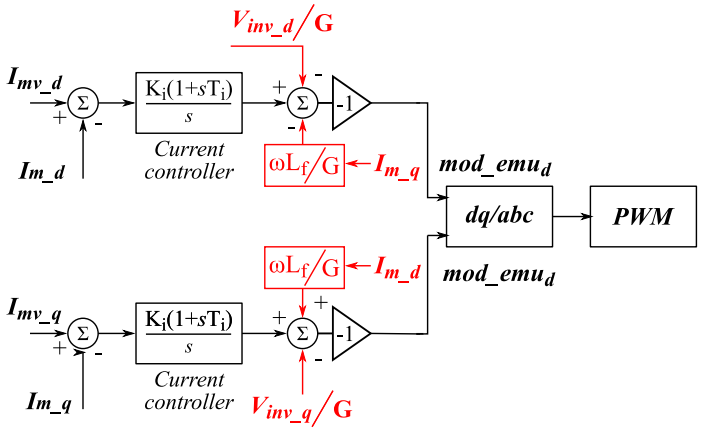

Fig. 2.7: Block diagram of the emulator current controller implementation with feed-forward and cross-coupling terms

this switching voltage sensing method reduces as the switching frequency of the driving inverter increases. Experimental results obtained for a low drive inverter switching frequency of 5 kHz did not add any errors due to the terminal voltage sensing.

B. Reference frame position for dq transformations:
The electric angle of the machine model, θ_e is used for the abc-dq transformations of emulator control. This is easily obtained by multiplying the rotor mechanical position, θ_m with the number of pole pairs. Both these angles are readily available using the machine model implemented within the RTS environment. This is a much easier alternative than using a PLL for the measured switching voltage of the driving inverter. To reduce switching voltage noise, filters might need to be used leading a phase error for the various transformations.

C. Feed-forward terms for emulator control:
Feed-forward gains do not affect the computed controller gains computed earlier in Section. 2.2.3, but are required for the implementation. The block diagram for the current controller for the emulator is shown in Fig. 2.4. These feed-forward and cross-coupling terms for the d-axis and the q-axis are given as (6) and (7), respectively.

$$V_{off\_d} = -\frac{V_{inv\_d}}{G} - \frac{\omega\, L_f\, I_{m\_q}}{G} \tag{6}$$

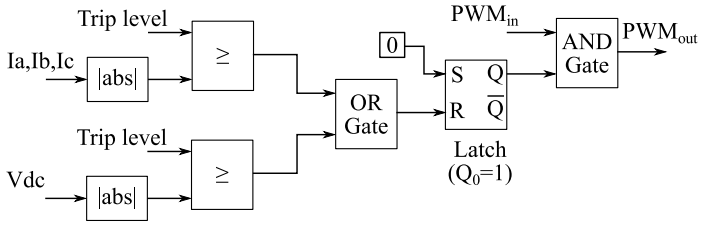

Fig. 2.8: Software protection logic to detect faults and block gating pulses to all inverters

$$V_{off\_q} = -\frac{V_{inv\_q}}{G} + \frac{\omega\, L_f\, I_{m\_d}}{G} \tag{7}$$

The cross-coupling terms with currents can be easily added. The feed-forward terms contain the d-axis and the q-axis voltage components of the inverter switching voltage. The measured switching voltages are initially transformed to their d and q axis components. Low pass filters remove the switching voltage components from these dq quantities.

D. Over-current and over-voltage protection (software):
The experimental setup will describe a hardware protection circuit to block gating pulses in the event of a fault. However, in addition a software latch circuit is also developed to block pulses in the event of fault. This software logic takes a much longer time to act ($\approx 20\mu s$) than the hardware protection circuit ($\approx 1\mu s$), but still acts as a fail safe if the hardware circuit fails to trip. A schematic block diagram of this fault is shown in Fig. 2.8. The same circuit is repeated for all three two-level inverters in the emulation system.

2.3 Real-time simulations

Real-time simulation results are presented in this section to validate the control and functioning of the proposed PMSM emulation system. A real-time simulator is used to implement the *plant* i.e. the various power converters of the machine emulation system. Another real-time simulator is used to implement the constituent control systems of the proposed machine emulation system. This resource allocation of the system on the real-time simulators is shown in Fig. 2.9. Measurements and gating signals are transferred over input-output lines via analog and digital pins of the real-time simulators.

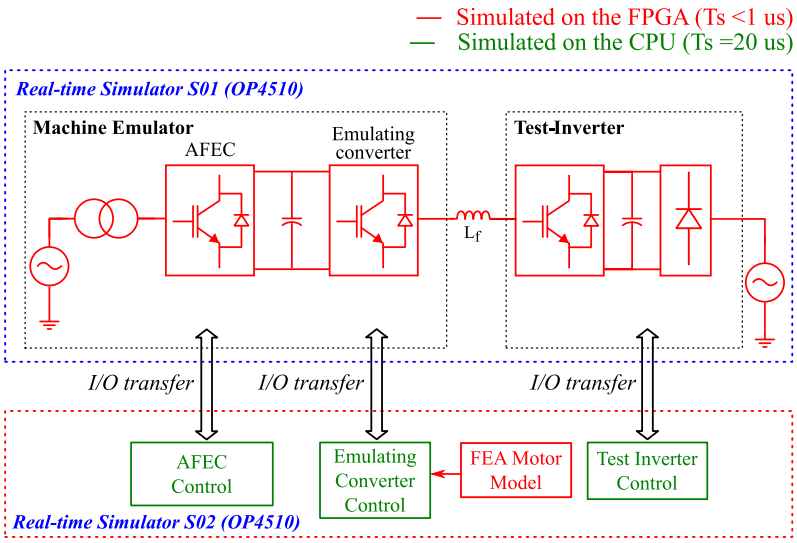

Fig. 2.9: Real-time simulator resource allocation of the PHIL machine machine emulator system.

Both the real-time simulators used are OP4510 [50]. These simulators have both CPU cores and FPGAs which are needed to perform simulations such as this one [35,38]. The power electronic converters on the real-time simulator S01, are implemented on the FPGA, to achieve a low simulation time step ($< 1\ \mu$s), and thus an accurate real-time simulation. The controllers for the various power converters are implemented on the CPU cores of the real-time simulator S02. Relevant tool-boxes from OPAL-RT® are used to allow this implementation. The PMSM FEA model, which uses look-up table data as discussed in Section 2.2.2, is also implemented on the real-time simulator S02. As shown in Fig 2.9, this FEA motor model current is the reference for the emulating converter control.

Section 2.2.3 discussed the selection of the emulating converter current loop's bandwidth being much higher than that of the test-inverter's, for a stable operation. To understand the impact of this further, the emulating converter current loop bandwidth is varied for a fixed bandwidth of the test-inverter current loop. Real-time simulations are performed for all cases. Fig. 2.10 shows the variation of the emulated machine q-axis current, for varying emulating converter bandwidths. The test-inverter current loop bandwidth is kept fixed at 350 Hz. A trace in Fig. 2.10 also shows the q-axis response of a physical PMSM drive for comparison. It can be clearly seen that as the emulator control bandwidth is reduced and brought closer to the test-inverter current loop bandwidth, the emulation loses accuracy or even compromises the stability

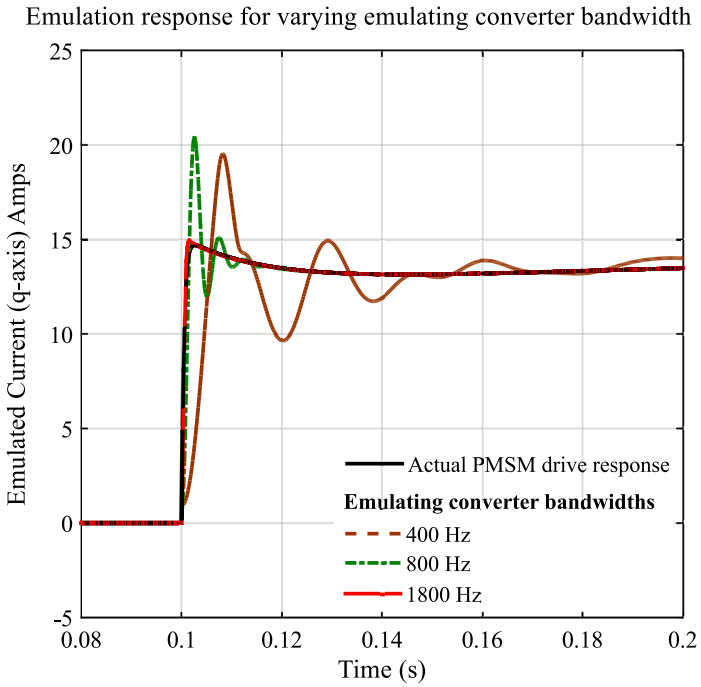

Fig. 2.10: Machine emulator current q-axis response for a fixed test-inverter current loop bandwidth of 350 Hz and varying bandwidth of the emulating converter current loop.

of the system. Hence for an accurate emulation, when the emulating converter and the test-inverter are both working in current control mode, it is recommended that the emulating converter current loop bandwidth is at least five times higher than the test-inverter current loop bandwidth. With reference to Fig. 2.6, this translates to a gain margin of at least 20 dB and a phase margin of at least 65°.

Fig. 2.11(a) presents the real-time simulation results pertaining to the PMSM emulator system, machine startup. The figure shows that the designed bandwidth of the emulation system is sufficient to emulate the PMSM model transient behavior. In Fig. 2.11(a), the machine is accelerated from 0 rpm to 1000 rpm, close to the rated speed of the machine. Fig. 2.11(b) on the other hand presents the results pertaining to the PMSM speed reversal. Again, the results show the sufficiency of the designed system bandwidth to emulate the PMSM transient behavior. In the presented result, the machine speed is reversed from -600 rpm to 600 rpm. The PMSM model current and the emulated current are placed on a different zero axis to ensure that both currents are clearly visible without any overlap.

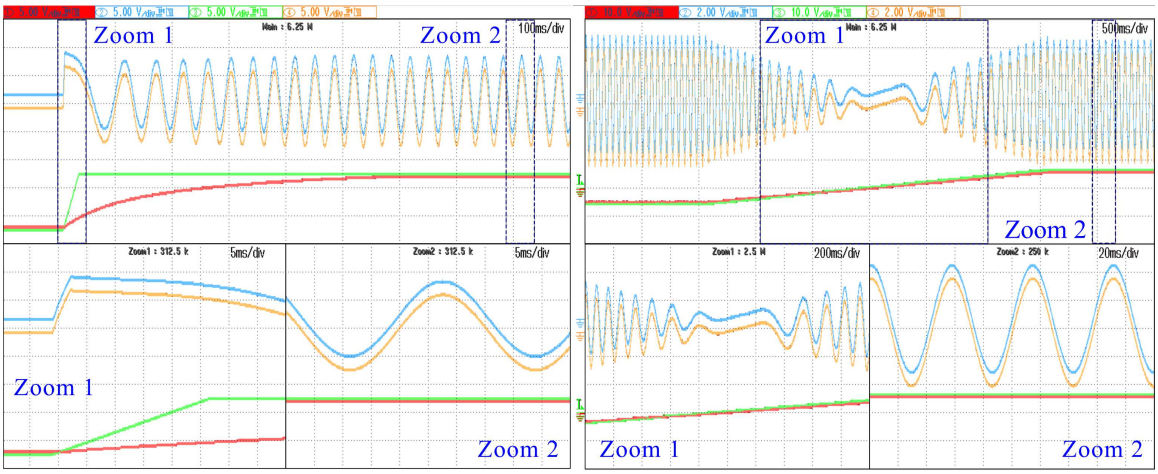

Fig. 2.11: (a) Real-time simulation of the PMSM emulator system, emulating machine start-up; CH1: PMSM speed (Scale: 100 rpm/div), CH2: PMSM model current (Scale: 2 A/div), CH3: reference speed for the PMSM model (Scale: 100 rpm/div), CH4: emulated current of PMSM (Scal: 2 A/div) (b) Real-time simulation of the PMSM emulator system, emulating machine speed reversal; CH1: PMSM speed (Scale: 100 rpm/div), CH2: PMSM model current (Scale: 2 A/div), CH3: reference speed for the PMSM model (Scale: 100 rpm/div), CH4: emulated current of PMSM (Scale: 2 A/div).

2.4 Experimental setup

The proposed PHIL based emulator system consists of two two-level converters connected back-to-back, acting as a four-quadrant power amplifier. As shown in Fig. 4.1, one of the two-level converters acts as a front-end converter and the other converter acts as the emulating converter, controlled to emulate the machine behavior. Fig. 2.13 shows the two two-level VSCs, real-time simulator (RTS) to control the system, the protection circuitry of the overall system, and the transformer connected at the AFEC end, to provide necessary isolation. The two-level VSCs consist of 1200 V, 50 A half bridge modules (SKM50GB123D). The switching frequency of the AFEC and the emulating converter is chosen as 15 kHz. The developed machine emulator was tested up to 15 kVA.

In the event of an over current or an over voltage fault, the protection circuit disconnects the emulator from the grid and blocks all the gating pulses. A schematic implementation of this protection circuit is shown in Fig. 2.12. OP-AMPs with a high slew rate (15 $V/\mu s$) are used to ensure that the protection circuit acts as fast as possible ($< 5\mu s$), thus working much faster than the software protection described

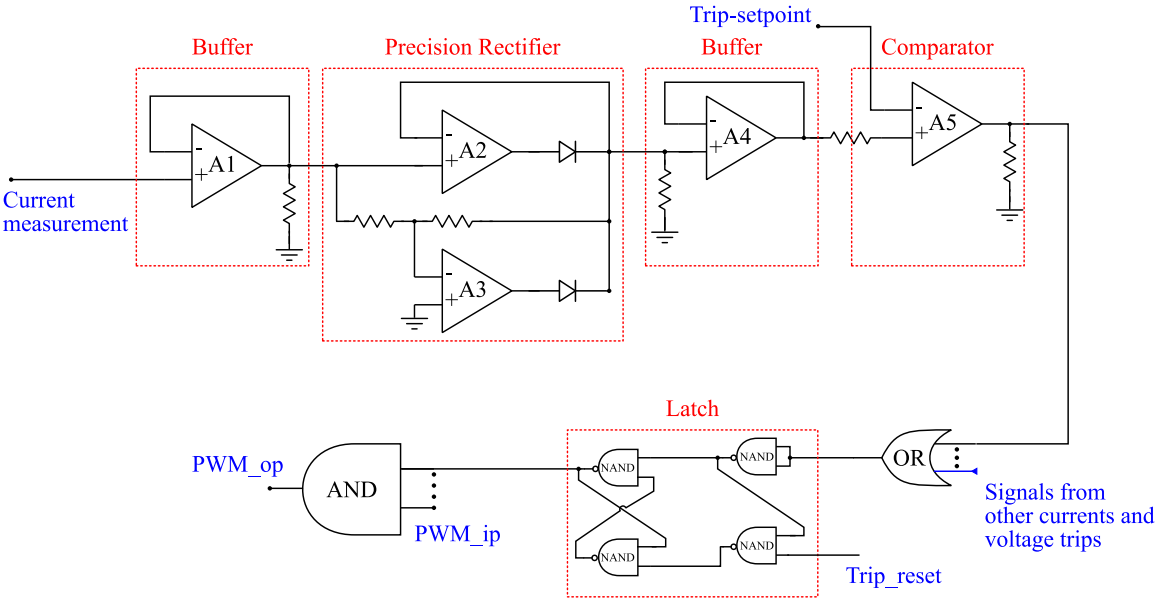

Fig. 2.12: Schematic diagram of the designed protection board

earlier. This hardware protection circuit works as a fail-safe in the event of the software protection failure.

The emulating converter is connected to the inductive-filter, which is further connected to the test-inverter. The test-inverter, for the results presented here, is also a two-level converter composed of similar switches as the emulator system. As discussed earlier a value of 3 mH is used for the L-filter. The test-inverter's controller assumes that the current through the L-filter is the same as that which would be drawn if it were connected to a physical machine. The emulating converter on the other hand is controlled to ensure that the current through this L-filter is equal to a simulated machine model current. Results relating to the emulation are presented in the following section.

The control for the emulator system and the test-inverter are both implemented on an OP4510 based real-time simulator [50]. The voltages and current sensor modules used are OP5511 [51], which transfer sampled quantities to the the RTS. The FEA based machine model [37], as discussed earlier, is used for the machine emulation. The machine model is implemented on the FPGA of the real-time simulator which is run at a time step of 5 ns. The look-up table data associated with the machine geometry/inductances are implemented on the DDR3 RAM block of the FPGA board. Details of the machine model implementation on the RTS are described in [35–38]. In addition to the machine model, the proposed emulator system also requires several

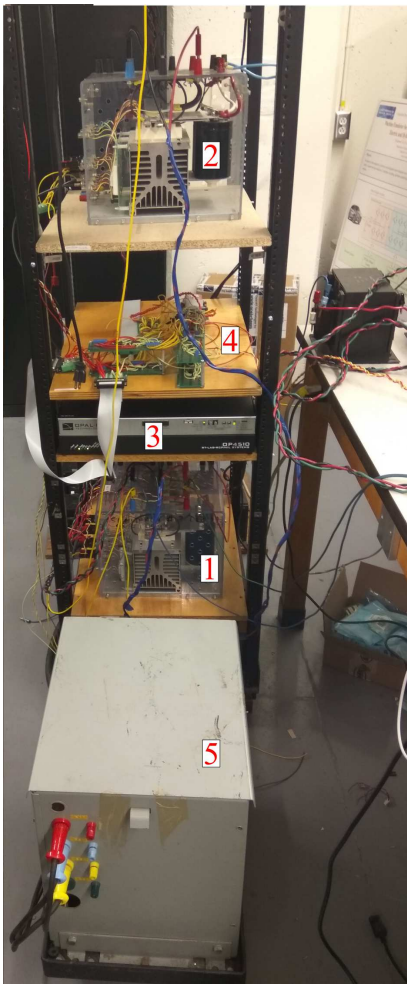

Fig. 2.13: (a) Experimental setup for the developed emulator system; (1) emulating converter, (2) active front-end converter (AFEC), (3) RTS to control the emulator system, (4) protection circuit for the emulator system, and (5) Transformer for isolation.

controllers, signal conditioning and gating pulse generation to implement the emulating converter control, the driving inverter control, and the active front end converter control. Matlab-Simulink® is used for the control implementation on the RTS, at a time step of 20 μs. This time step translates to a sampling frequency of 50 kHz for the power hardware of emulator system, which is adequate. Implementing the complete control and machine model on the real-time simulator, as discussed allows for a systematic and simple deployment of the proposed machine emulator control system.

A physical surface-mounted PMSM, coupled to a DC dynamometer is shown in Fig. 2.14. The 220 V, 1200 rpm surface-mounted PMSM has a stator resistance of

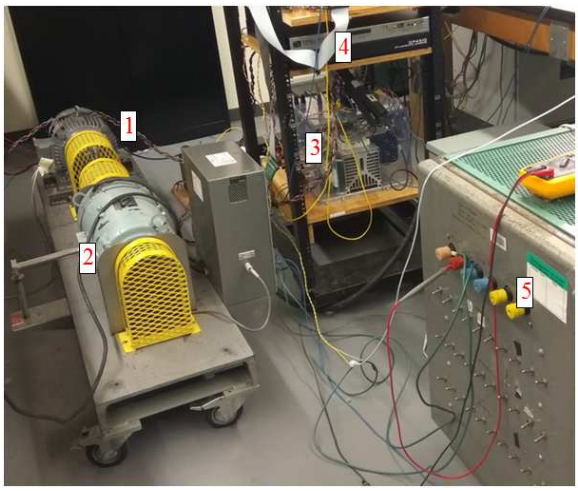

Fig. 2.14: Experimental setup for the physical surface mounted PMSM coupled to a DC dynomometer; (1) the surface mounted PMSM, (2) the coupled DC dynamometer, (3) driving inverter for the PMSM, (4) RTS with the PMSM vector control algorithm, (5) load box to load the DC dynamometer.

0.1718 Ω, d-axis and q-axis inductances of around 3.36 mH, and inertia of 0.0334 kgm^2. The machine is coupled to a 15 hp dc dynamometer. The dynamometer is connected to a resistance bank to load the PMSM machine. The test-inverter driving the (emulated) PMSM is programmed with a conventional vector control algorithm as shown in Fig. 2.3(c). The current loop bandwidth is designed to be 350 Hz and the speed loop bandwidth is designed to be around 50 Hz. Experimental results obtained from the physical dynamometer setup are validated against that obtained from the emulator system in Section 2.5.

2.5 Experimental results

This section validates the proposed emulator system by emulating several transient conditions such as machine start-up, speed-reversal, load torque change and low current control bandwidth operation. Since a detailed look-up table based machine model is used in the proposed machine emulator system, several transient conditions and machine magnetic and geometric (eg: torque ripple) behavior can be emulated. The impact of torque ripple on the machine current waveform is emulated by operating the driving inverter at a low current loop bandwidth. This emulation is possible only due to the use of a detailed look-up table based machine model for the proposed emulator system. The results obtained from the proposed machine emulator system are further

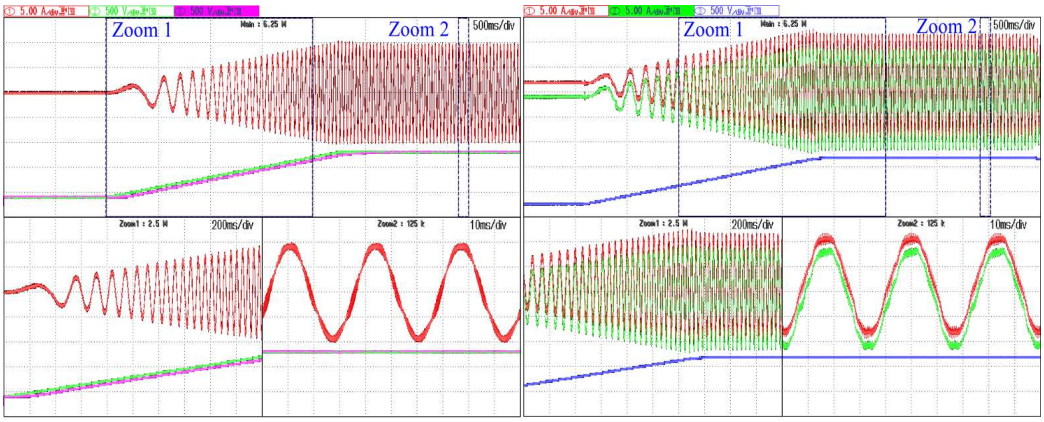

(a) (b)

Fig. 2.15: (a) Experimental results obtained for a physical PMSM start-up, when coupled to a DC dynamometer; CH1: PMSM current (Scale: 5A/div), CH2: speed set-point (Scale: 500 rpm/div), CH3: measured speed of the PMSM (Scale: 500 rpm/div); (b) Experimental results obtained for start-up from the emulation system; CH1: emulated line current (Scale: 5A/div), CH2: reference current for emulation (Scale: 5A/div), CH3: emulated PMSM speed (Scale: 500 rpm/div).

compared with a physical machine. Error plots are additionally shown to prove the emulation accuracy.

Fig. 2.15 presents results relating to machine start-up from zero to rated speed obtained from the physical dynamometer setup and the emulator system. As can be seen there is a close match between the two results, proving effective emulation capabilities of the system. CH1 (in Fig. 2.15(b)) shows the emulated current and it closely follows the FEA machine model current shown in CH2 (in Fig. 2.15(b)). (CH1 and CH2 currents are at a different offsets to visually differentiate between the two). Fig. 2.19(a) additionally shows the absolute error between the current drawn by the physical machine (shown in Fig. 2.15(a)) and the current drawn by the proposed machine emulator system (shown in Fig. 2.15(b)). This error being small, less than 5%, validates the ability of the designed emulator system for performing accurate emulation.

Fig. 2.16 presents the results relating to machine speed reversal obtained from the physical dynamometer setup and the emulation system. The speed set-point is changed from 600 rpm to -600 rpm. Fig. 2.17 on the other hand presents results relating to a sudden load change obtained from the physical dynamometer setup and the emulation system, respectively. Fig. 2.19(b) and Fig. 2.19(c) are the absolute errors between the current drawn by the physical machine and the current drawn by

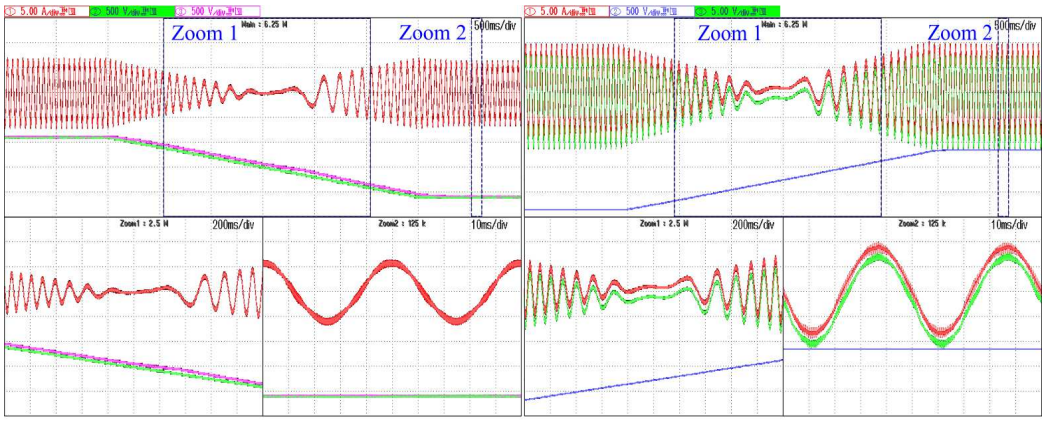

(a) (b)

Fig. 2.16: (a) Experimental results obtained for a physical PMSM speed-reversal, when connected to a DC dynamometer; CH1: PMSM current (Scale: 5A/div), CH2: reference for the speed set-point (Scale: 500 rpm/div), CH3: measured speed of the PMSM (Scale: 500 rpm/div); (b) Experimental results obtained for speed reversal from the emulation system; CH1: emulated line current (Scale: 5A/div), CH2: reference current for emulation (Scale: 5A/div), CH3: emulated PMSM speed (Scale: 500 rpm/div).

the proposed emulator system, for the speed reversal condition and the sudden load change condition, respectively. A close match between the dynamometer results and the emulation system results, for the various transient conditions, proves the capability of the proposed system to emulate various motor transients. Again the error being less than 5% validates the ability of the designed emulator system for performing accurate emulation. Furthermore, Fig. 2.16(b) and Fig. 2.17(b) present both the FEA reference model current and the emulated currents in CH2 and CH1 respectively.

An important contribution of this chapter is the development of an emulation system which can emulate a machine based on its geometric and magnetic data. This has been explained in Section 2.2. Fig 2.18(a) and Fig 2.18(b) are results obtained from a physical surface mounted PMSM. The machine is driven at a fixed speed of 200 rpm and is lightly loaded. For the result presented in Fig 2.18(a), the current controller (see Fig. 2.3(c)) bandwidth is 350 Hz. Due to the current loop action, and a relatively high bandwidth, the torque ripple (due to rotor position variation) is absorbed by the controllers and the current waveform is largely sinusoidal. On the other hand, in Fig 2.18(b), the current loop bandwidth is intentionally reduced to 200 Hz. The distortion in the current waveform, due to the inadequacy of the current controller bandwidth to nullify the effect of torque ripple, is clearly visible.

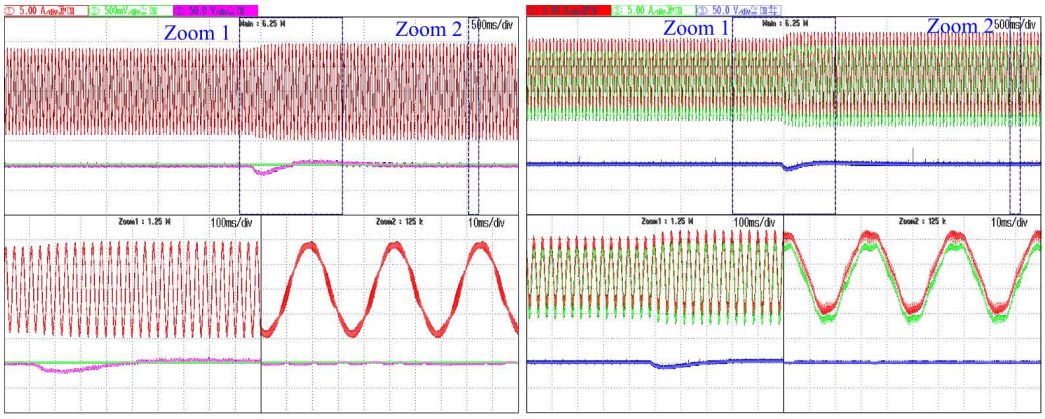

Fig. 2.17: (a) Experimental results obtained for a sudden load change of the physical PMSM, when connected to a DC dynamometer; CH1: PMSM current (Scale: 5A/div), CH2: reference for the speed set-point (Scale: 50 rpm/div), CH3: measured speed of the PMSM (Scale: 50 rpm/div) (b) Experimental results obtained for sudden load change from the emulation system; CH1: emulated line current (Scale: 5A/div), CH2: reference current for emulation (Scale: 5A/div), CH3: emulated PMSM speed (Scale: 100 rpm/div).

As mentioned earlier, the accuracy of the emulation system depends on the machine model used. Consider a simple dq model being used for the purpose of emulation. In such a model, information relating to the torque ripple (due to varying rotor position) is not present, hence the emulation cannot take it into account as well. Thus, Fig 2.18(c) which uses such a dq based model for emulation shows sinusoidal currents for even a low current control bandwidth of 200 Hz (refers to the test-inverter current control bandwidth). Now consider a FEA based machine model used for emulation, as proposed in this chapter. Such a model contains information relating to torque ripple due to the rotor position variation in a look-up table based form. Fig. 2.18(d) shows results obtained from the proposed emulation system using this FEA machine model as a reference. It can be seen that the current waveform is closer to the actual PMSM running at the same bandwidth condition, shown in Fig. 2.18(b). This highlights the importance of using a detailed FEA based machine model for emulation, proposed as part of this PhD work.

To additionally prove the accuracy of emulation the absolute errors between current drawn by the physical machine (Fig. 2.18(b)) and the current drawn by the machine emulator system (Fig. 2.18(d)) for the case of low speed low current loop bandwidth, is plotted in Fig. 2.19(d). As in the previous results, the error in this case is also less

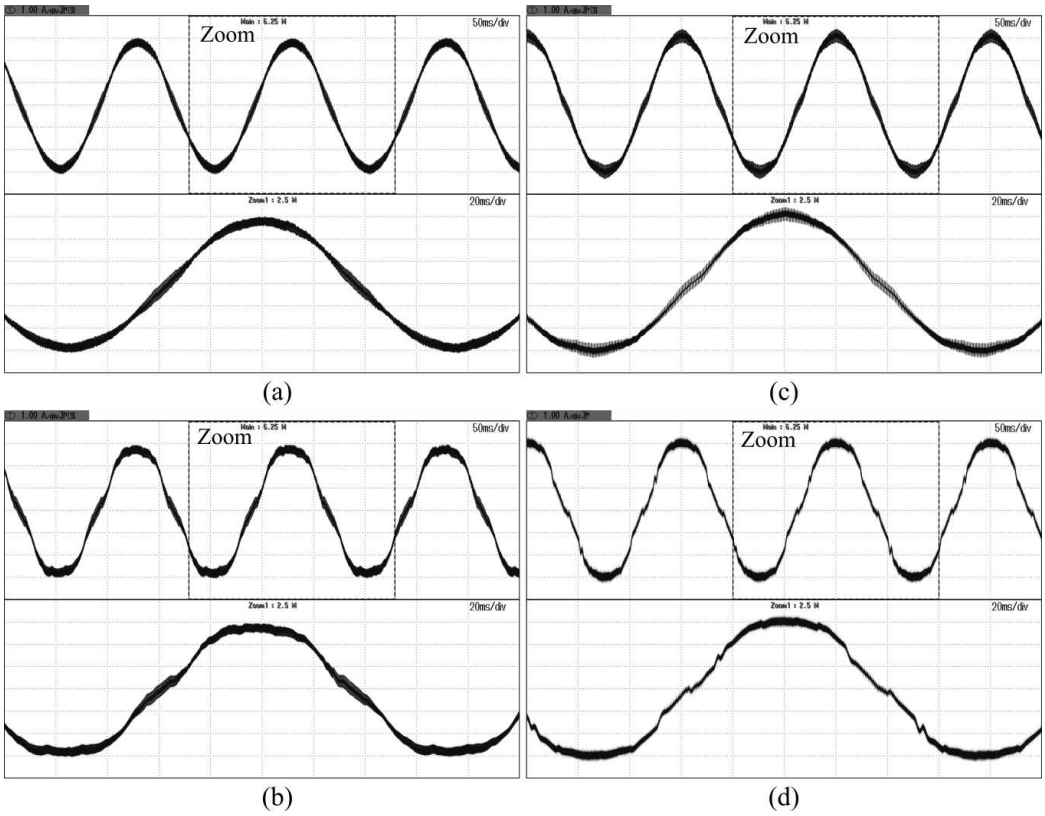

Fig. 2.18: Experimental results obtained from the physical PMSM for low speed (200 rpm) and light load conditions (a) current drawn by the physical PMSM when current control bandwidth is set at 350 Hz (b) current drawn by the physical PMSM when the current control bandwidth is set at 200 Hz. Experimental results obtained from the emulated PMSM for low speed (200 rpm), light load conditions and a low test-inverter current control bandwidth (200 Hz) (c) current drawn by the emulation system when using a simple *dq* machine model (d) current drawn by the proposed emulation system using an FEA based machine model.

than 5% proving the utility of the proposed emulator system to emulate a wide variety of transient conditions, accurately.

2.6 Summary

This chapter presented the power structure and control design for a PHIL based machine emulator system. The machine emulator system consists of two back-to-back two-level converters controlled to mimic machine behaviour. The proposed machine emulator system used FEA look-up table data based machine models which were shown to improve the emulation accuracy significantly. The main findings of this

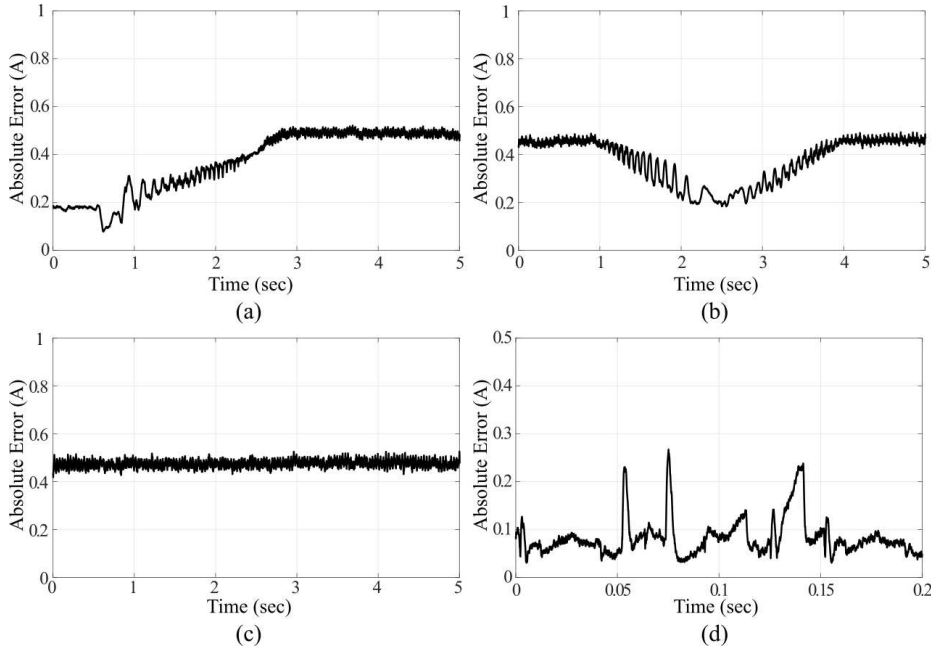

Fig. 2.19: Absolute error between current drawn by the physical machine and current drawn by the proposed machine emulator system for; (a) machine start-up; obtained over the same acquisition window as Fig. 2.15, (b) machine speed-reversal; obtained over the same acquisition window as Fig. 2.16, (c) sudden load change on the machine; obtained over the same acquisition window as Fig. 2.17, and (d) low-speed low current loop bandwidth operation of the machine; obtained over the same acquisition window as Fig. 2.18.

chapter are summarized as follows:

A. The proposed machine emulator system uses flux and torque look-up tables obtained from an FEA tool allowing the machine emulator to emulate a variety of transient conditions, and mimic the machine magnetic (eg: saturation) and geometric (eg: torque ripple) behavior. This is particularly important to perform a high-quality high-accuracy emulation. Experiential results were presented to show how a simple *dq*-model of the machine reduces emulation accuracy.

B. The proposed machine emulator system uses a simple current control for the emulator system along with an inductive-filter to connect the machine emulator with the driving inverter. This allows for a simple practical realization of the emulator system. The conflict between the emulator current control and the test-inverter (driving inverter) current control is avoided by selecting the emulator bandwidth to be much higher than the driving inverter current controller

bandwidth. Analysis, both experimental and real-time are presented to validate this conclusion.

C. This chapter also presented the importance of emulation bandwidth on the emulation accuracy. Since two-level converters are used for the purpose of emulation in this chapter, the maximum emulation bandwidth is also limited to around 2 kHz. Furthermore since dq-control is on the fundamental frame, only currents harmonics of up around 200 Hz can be faithfully controlled to their required values. This will be a concern when the fundamental frequency is high, pushing the lower order harmonics to a higher value as well. The solution is to increase the emulation bandwidth further. To address this requirement, emulation with linear amplifiers will be presented in the next chapter.

The functioning of the proposed machine emulator system was initially validated using real-time simulations. Subsequently experimental results were obtained from the developed machine emulator and physical surface-mounted PMSM coupled to a DC dynamometer. These results were compared for a variety of transients such as start-up, speed reversal, and load change. Additionally, absolute error plots between the physical machine currents and the emulated machine currents were also presented. A close match between the results obtained from the physical machine and the results obtained form the machine emulator system were shown to prove the validity and utility of the proposed machine emulator system.

Chapter 3

Linear amplifier based emulation of a variable flux machine

The previous chapter presented the control for a machine emulator system and the methodology of using machine look-up table based FEA data, within a machine model, for controlling the emulator system. The emulator system presented had an emulation bandwidth of around 2 kHz, limited due to the switching frequency of the power converters used within the emulator system (15 kHz). This chapter will develop a machine emulator system with linear amplifiers emulating machine behavior. Linear amplifiers have a high bandwidth and hence the developed emulator system is expected to have a high emulation bandwidth as well. Aspects of controller implementation to allow the realization of a high emulation bandwidth will be investigated in detail. The developed emulator system will be used to emulate a variable-flux machine (VFM). Emulation results will be compared with results obtained from a prototype machine to comment on the emulation accuracy.

3.1 System description of the VFM emulator

The schematic diagram of the linear amplifier based machine emulator is shown in Fig. 3.1. A block diagram of the control circuit is also shown in the same figure. The system description remains the same as shown in Chapter 2. It is however repeated here briefly, for the sake of clarity.

The driving inverter controller (shown in Fig. 3.1) requires speed (ω^*) or torque (T^*) set-point, and the measured currents drawn by the linear amplifiers (I_{motor}). A standard vector control can then be implemented to generate gating pulses for the

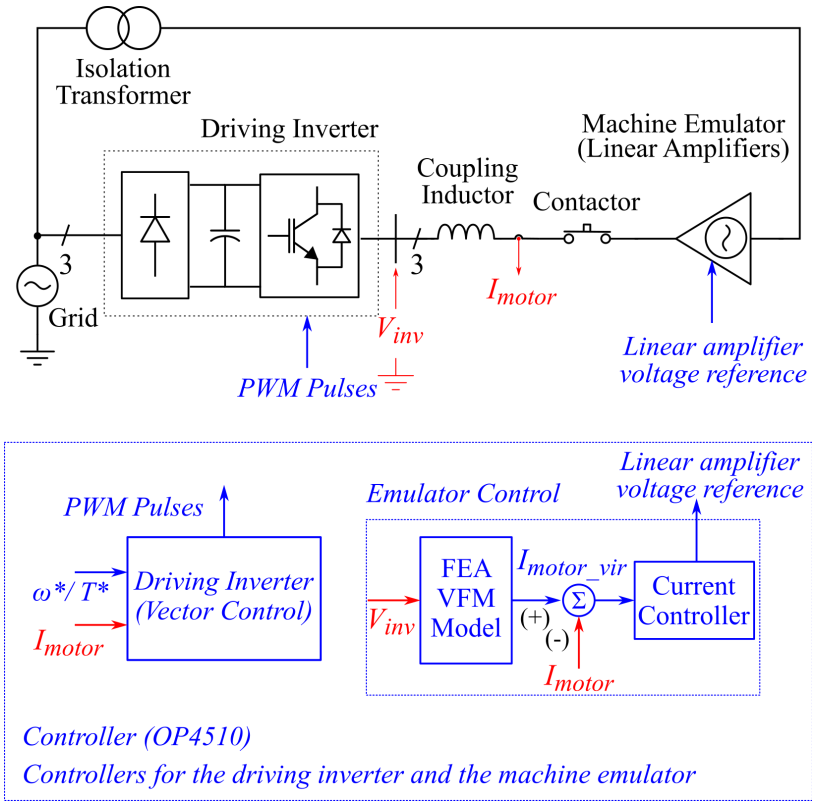

Fig. 3.1: Schematic diagram of the proposed linear amplifier based VFM emulator system

driving inverter. The details are discussed in [52, 53]. The switching voltage output of the driving inverter is then measured and given as an input to the look-up table based FEA VFM model. Look-up table based machine models were developed for real-time simulations and controller hardware-in-the-loop (CHIL) simulations in [38, 39]. The same model is updated with the look-up tables of flux, inductance and torque variation of a VFM and used for the purposes of emulation in the system shown in Fig. 3.1. This machine model generates a current reference for the current controller within the emulator control shown in Fig. 3.1. The current controller generates a voltage reference for the linear amplifier enabling them to mimic the machine behavior defined in the look-up table based FEA VFM model.

The interface/coupling element connecting the linear amplifiers and the driving inverter is an inductance. This allows for a simple practical realization of the emulator system. It is preferred that the value of the coupling inductance is close to the machine average inductance [24]. For the VFM emulated in this chapter, the machine mean inductance is quite large, at around 50 mH. Having a physical coupling inductance at

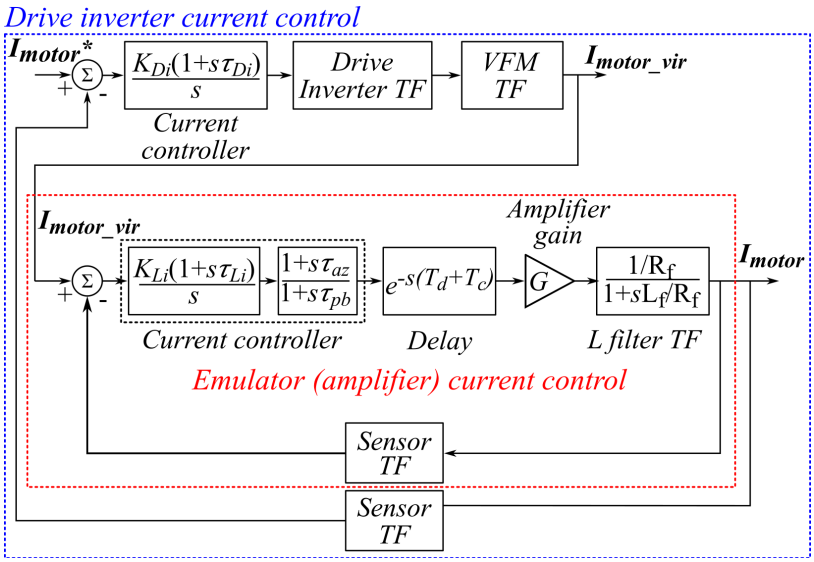

Fig. 3.2: Block diagram of the linear amplifier current control loop within the driving inverter current control loop

this value would be impractical. Hence a much smaller value of 5 mH is chosen. Since the linear amplifiers are controlled to draw currents similar to the machine model currents, the dynamics associated with the inductance deviation are compensated by the current control action of the linear amplifiers.

3.2 Controller design for the machine emulator

Similar to the current control technique discussed in Chapter 2, the same control technique is used for the linear amplifier based machine emulator discussed in this chapter as well. This chapter will revisit the current control when high bandwidth linear amplifiers are used as power amplifiers within the machine emulator system. This will involve a detailed control design and a low sample-time controller implementation. Furthermore, this chapter will also validate the current control presented in Chapter 2 for the emulation of a VFM at different magnetization levels.

Fig. 3.1 shows the controllers for the driving inverter and the machine emulator. It can be seen that these controllers do not directly interact with each other and hence can be implemented on separate controller platforms, which is desirable. Both controllers, of the driving inverter and the machine emulator, are essentially operating in *current control* mode.

The interaction of the current control loop of the emulator with the current control

loop of the driving inverter is shown in Fig. 3.2. The output voltage of the driving inverter, V_{inv} (which is the result of the driving inverter control) is fed to the *VFM Machine Model*, which in turn generates a current reference, I_{motor_vir}, for the machine emulator control. This results in a cascade current control structure as shown in Fig. 3.2. The emulator current control is an inner loop within the driving inverter current control loop.

The current control for the machine emulator (linear amplifiers) comprises a standard PI controller and a lead-lag compensator, to control the d-axis and q-axis components of the current. The controller design is to obtain the maximum possible bandwidth within the hardware limitations. This ensures that several lower order harmonics of the machine current waveform, can be faithfully emulated.

The linear amplifiers used in this chapter have a bandwidth of 200 kHz. In addition, the linear amplifiers also have an on-delay of around 600 ns [54]. Hence, the total delay due to the linear amplifiers can be lumped as T_d and represented as e^{-sT_d}. The value of T_d is considered as 1 μs for the purpose of the control design presented in this chapter. Fig. 3.2 also shows the delay associated with the implementation of the emulator control on the real-time simulator, e^{-sT_c}. To achieve the maximum closed loop bandwidth of the emulator current control loop, e^{-sT_c} should be at its minimum value. Achieving a low controller time step is not trivial, and is explained in the following section.

3.2.1 Control implementation modifications to achieve low time-step implementation

The real-time simulator (RTS) used for implementing the control is OP4510® [55]. Prior to commenting on the capability of the OPAL-RT system to achieve a low time-step, its hardware structure needs to be explained briefly. The RTS used for this project has CPU cores and an FPGA board. Implementing the control on the CPU cores is simple and can be done directly with MATLAB/SIMULINK® and a few custom library block sets from RT-LAB®, the accompanying software of the RTS. There is a quick learning curve associated with this process and the time to realize a simulation model in real-time is quick as well. However, the time-step for the real-time simulation (or computation time) when the controller is implemented on the CPU cores is limited to $15 - 20\mu s$. This time step which is significantly larger than the on-time delay of the linear amplifier, is thus a factor which limits the maximum

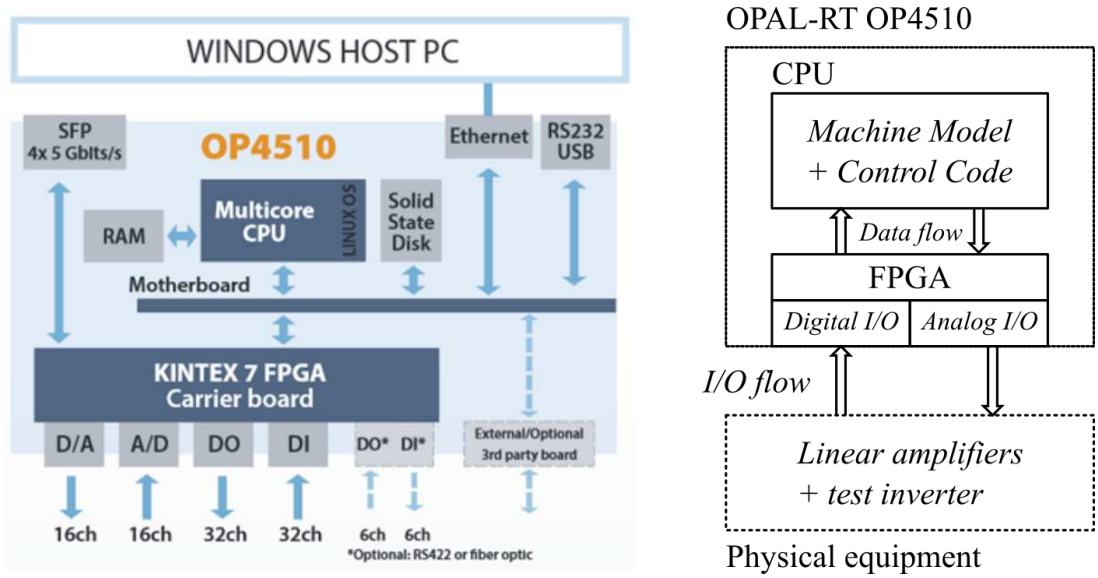

(a) (b)

Fig. 3.3: (a) Schematic illustration of computational resources in OP4510(b) Information flow in the OPAL-RT

achievable bandwidth as well.

As mentioned earlier, the RTS has both CPU cores and an FPGA board. An illustration of the same is shown Fig. 3.3. In order to connect to a real world object such as a power amplifier, control signals are transferred to and from the RTS to the power amplifier using I/O cards. The I/O cards operation is controlled by the onboard FPGA of the RTS. In the event of the machine emulator control being implemented on the CPU cores of the RTS, there is an additional time required for information flow from the CPU cores to the onboard FPGA, which essentially leads to a high computation time step of $15 - 20\mu s$. Moving the machine emulator control from the CPU cores to the FPGA board can reduce the simulation time-step significantly. FPGA boards allow parallel implementation, allowing an extremely low time step of $< 1\mu s$. Therefore, the control for the machine emulator, along with the FEA based VFM machine model, are both implemented on the FPGA board of the OP4510®. The control algorithm is implemented using fixed-point arithmetic on the FPGA board using VIVADO®.

The control time step is now reduced to 500 ns. The analog-to-digital converter (ADC) and the digital-to-analog (DAC) boards on the OP4510® additionally have a conversion time of 2.5 μs and 1 μs, respectively. Hence the computation time T_c, when the control and the machine model are both implemented on the FPGA board, reduces

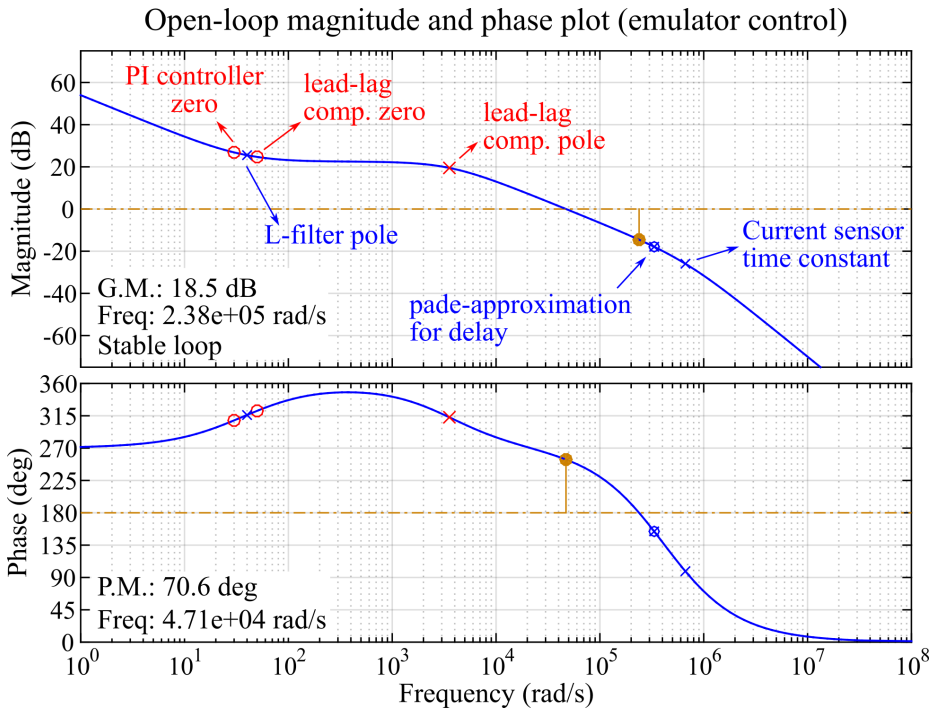

Fig. 3.4: Magnitude and phase plots for the emulator current control open-loop transfer function

to approximately 5 μs. This is the minimum value of T_c that can be achieved with the RTS used in this PhD thesis, and hence allows maximum emulation bandwidth for the developed system. The control implementation directly on the FPGA board using VIVADO® is more rigorous, but allows the possibility to reach a high emulation bandwidth.

3.2.2 Controller design: type and gains

The open-loop transfer function of the emulator current control loop is represented as shown in (8). $C(s)$ is the compensator to be designed and is represented in (9). The computation time step delay and the linear amplifier delay (defined earlier) are T_c and T_d, and are 5 μs and 1 μs, respectively as explained earlier. The linear amplifier gain, G, is equal to 20. For the machine emulator implemented here, the values of L_f (coupling inductance) and R_f (coupling resistance) are 5 mH and 200 $m\Omega$, respectively. The current sensors used in the system have a bandwidth of 100 kHz. The current sensor is approximated in (8) as a first order transfer function with a

time constant of 1.5 μs, calculated based on the sensor bandwidth.

$$EMU(s) = C(S).G.e^{-sT_c}e^{-sT_d}\frac{\frac{1}{R_f}}{1+s\frac{L_f}{R_f}}\frac{1}{1+sT_{fi}} \tag{8}$$

$$C(s) = \frac{K_{PI}(1+s\tau_{PI})}{s}\frac{1+s\tau_{az}}{1+s\tau_{pb}} \tag{9}$$

The compensator for the emulating converter current control loop, $C(s)$ is described in (9). It consists of a standard PI controller and a *lead-lag* compensator. As mentioned earlier, the objective is to achieve the highest bandwidth possible, respecting the system limitations. The magnitude and the phase plots of the emulator current control open loop transfer function (the transfer function shown in (8)), is presented in Fig. 3.4. The compensator gains are computed as $K_{PI} = 5$, $\tau_{PI} = 0.033$, $\tau_{az} = 0.02$ and $\tau_{pb} = 0.0003$. The choice of the compensator allows a high bandwidth realization at 7.5 kHz. The high bandwidth for the emulator current control will result in high emulation accuracy as well. Fig. 3.4 further shows that the high emulator bandwidth is primarily possible due to the low time-delays associated with the controller computation time-step and the linear amplifier delay.

As stated earlier, the emulator current control loop is an inner loop within the driving inverter current control loop. The closed loop transfer function of the emulating converter current control loop can be approximated as simple first order transfer function with a time constant τ_{CL} calculated based on the designed bandwidth of 7.5 kHz. The closed loop transfer function of the emulating converter current control loop is therefore given by (10), where $\tau_{CL} = 21.22$ μs.

$$EMU\_CLTF(s) = \frac{1}{1+s\,\tau_{CL}} \tag{10}$$

The driving inverter current controller can then be subsequently designed. The various transfer functions in the driving inverter current loop of Fig. 3.2, are described as follows. The drive inverter is approximated as a first order transfer function with a gain corresponding to $V_{dc}/2 = 200$ and a time constant corresponding to the sum of the PWM sampling time and the controller sampling (computation) time, which is 120 μs (τ_d). For the purpose of the control design exercise presented here, the machine is approximated as a simple dq model with machine d-axis inductance of 50 mH (L_d) and machine phase resistance of 1.3 Ω (R_s). The open loop transfer function of the driving inverter current control loop can be represented as (11), where $C(s)$ is the

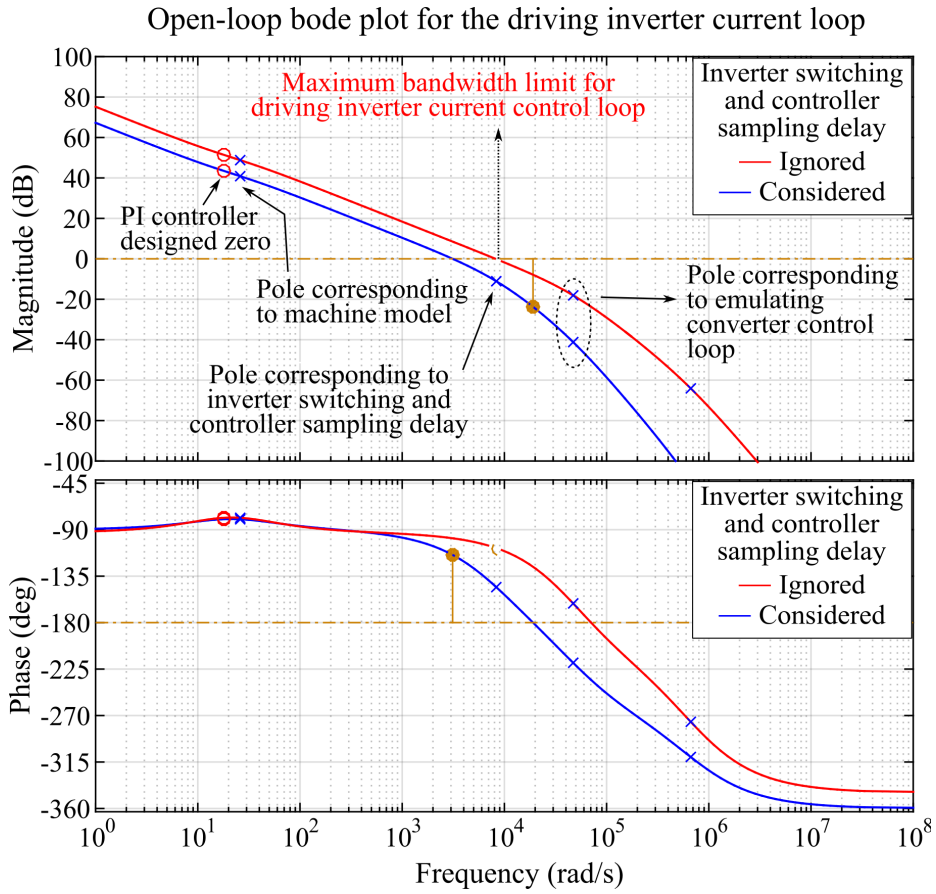

Fig. 3.5: Magnitude and phase plots for the driving inverter current control open-loop transfer function

driving inverter current controller, a standard PI controller as shown in Fig. 3.2.

$$DRIV(s) = C(S).\frac{\frac{1}{R_s}}{1+s\frac{L_d}{R_s}}\frac{\frac{V_{dc}}{2}}{1+s\,\tau_d}\frac{1}{1+s\,T_{fi}}\frac{1}{1+s\,\tau_{CL}} \tag{11}$$

The magnitude and phase plots for the driving inverter current control loop are shown in Fig. 3.5. The *red-trace* is for the case when inverter switching and controlling sampling delay (τ_d), are ignored. This helps understand the case of the maximum driving inverter control bandwidth for a given machine emulator current control bandwidth. The pole corresponding to the inner emulator control loop action limits this driving inverter bandwidth. The maximum driving inverter bandwidth is limited to around 1.5 kHz which is about five times smaller than the emulator current control bandwidth of 7.5 kHz, as designed in this chapter. This relation is in agreement with the findings in [24] as well. Hence, the capability of having a high current control

bandwidth of the machine emulator system leads to the possibility of testing driving inverters with high current control bandwidths as well.

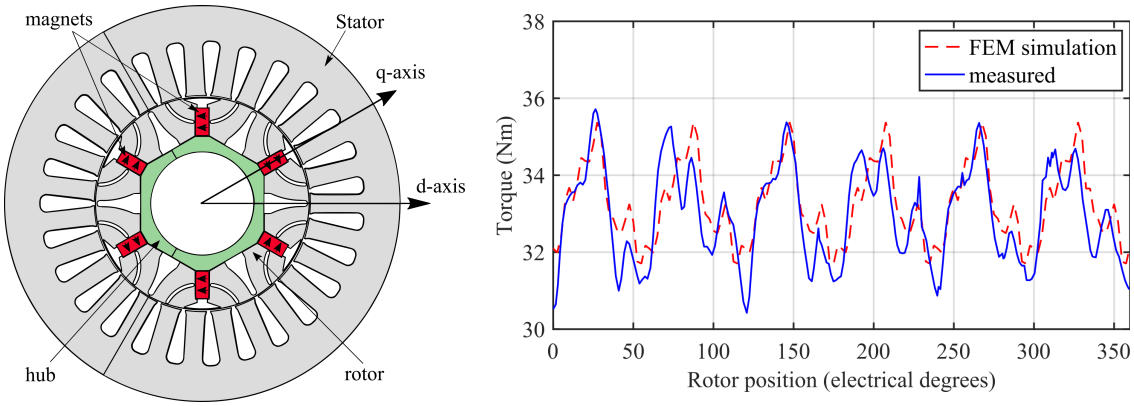

Fig. 3.6: (a) Cross section of the VFM being emulated, (b) Comparison of the torque waveforms at the rated current and 78° torque angle for an electrical cycle at 100% magnetization state.

For the system implemented in this chapter, the driving inverter is switching at 5 kHz. The controller sampling time is 20 μs. This leads to an overall delay of $\tau_d = 120$ μs (approximated as a first order transfer function). This reduces the achievable bandwidth from the driving inverter (*blue-trace* in Fig. 3.5) to around 500 Hz. This is of course within the maximum possible bandwidth of the driving inverter for a given machine emulator bandwidth.

3.3 VFM model for emulation

Section 3.1 explained that the machine emulator system developed in this chapter uses a FEA look-up table based VFM machine model to control the emulator operation. Therefore, to comment on the accuracy of emulation, with respect to results obtained from a prototype machine, it is important that the FEA machine model accuracy be validated first.

Fig. 3.6a shows the cross section of the VFM model, used for emulation. A physical prototype of the same machine has been developed earlier [52, 53]. A current pulse in the d-axis is sufficient to change the magnetization level of the machine, allowing control of the air gap flux [53]. This additional degree of control provides many benefits in servo-drives and electric vehicle applications [52, 53, 56]. The VFM

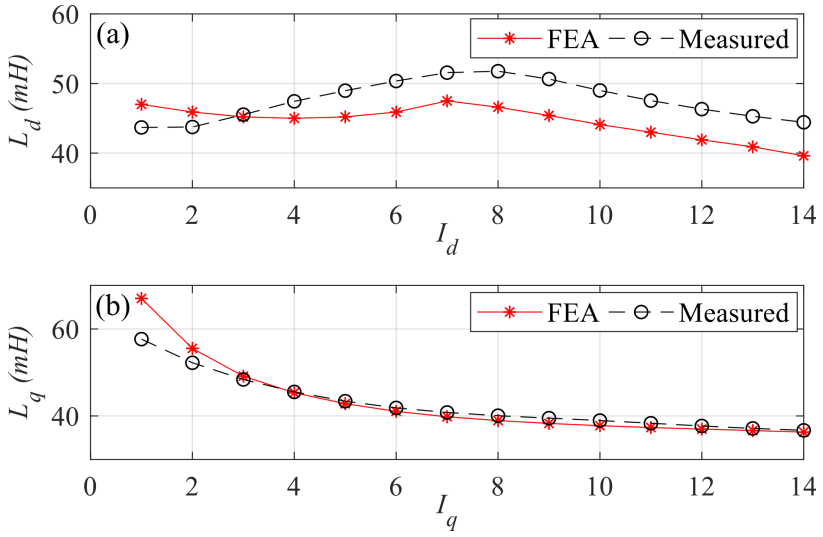

Fig. 3.7: Comparison of FEA inductances with experimental measurement at 100% magnetization state. (a) L_d. (b) L_q.

shown is modeled in a FEA software, MotorSolve®, and the look-up tables obtained for inductance variation, torque variation, and flux variation, against the variation of current magnitude, rotor position, and current advance angle, are used for the emulated VFM model. To validate the accuracy of the FEA look-up table which in turn defines the accuracy of the emulation as well, a comparison is done for a few results obtained from the FEA tool against the measured results obtained from the prototype machine.

Fig. 3.6b shows the comparison of the torque waveforms at 100% magnetization state obtained from the FEA model and the measurement from a prototype VFM for rated current and a fixed torque angle of 78°. A vector controlled drive in [57] is used for this measurement from the prototype machine. It can be seen that there is a close match between the FEA model and the experimental results. A current reference based technique proposed in [58] is used to measure the prototype machine inductances. Fig. 3.7 shows the comparison of the d-axis and the q-axis self-inductances obtained from the machine FEA model and the experimental results obtained from the prototyped machine when the magnets are fully magnetized. A similar comparison of experimental and FEA model inductances for a magnetization state of 75% is shown in Fig. 3.8a. Fig. 3.8b on the other hand shows the comparison of the machine cross-coupling inductances obtained from the FEA machine model and the experimental results at full magnetization level.

Figs. 3.6b–3.8b show an acceptable agreement between the FEA machine model

and the prototype VFM. Hence the VFM emulator system presented in this chapter is expected to be able to emulate machine behavior close to the prototype VFM as well. Since the VFM emulator uses a FEA look-up table based model, it is expected to emulate machine's geometric behavior, as shown in Fig. 3.6b, and magnetic behavior, as shown in Figs. 3.7– 3.8b.

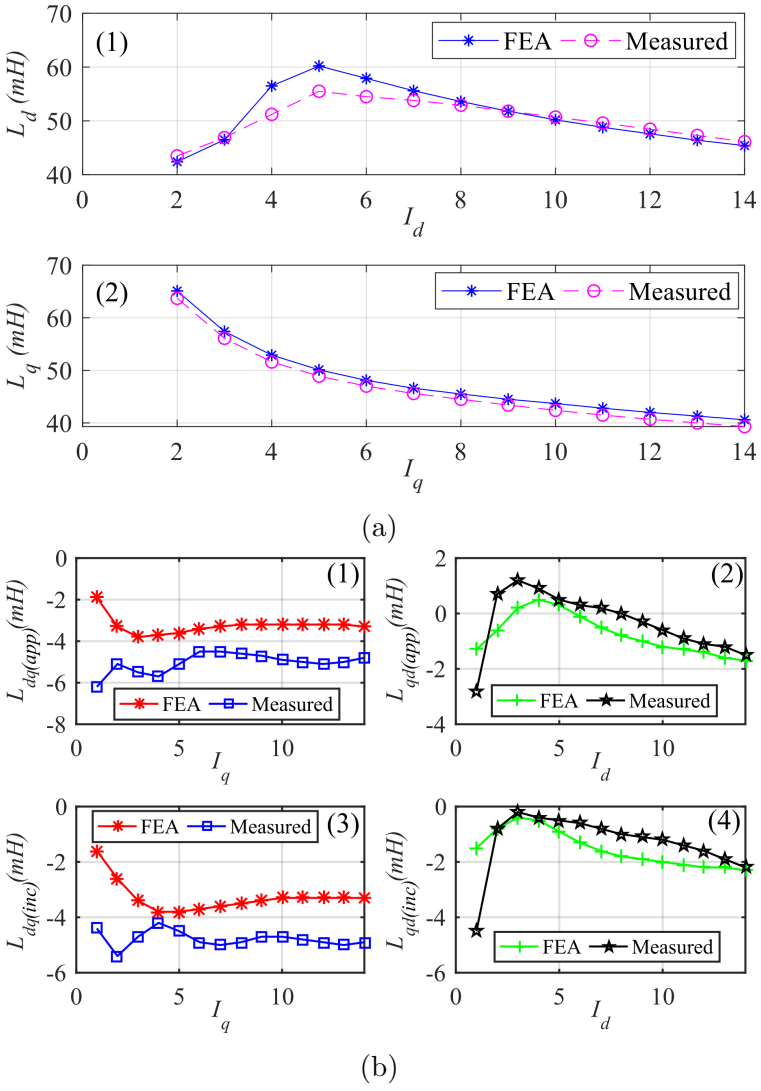

Fig. 3.8: (a) Comparison of FEA apparent inductances with experimental measurement at 75% magnetization state (1) L_d (2) L_q; (b) Comparison of FEA cross-coupling inductances with the experimental measurement at 100% magnetization state (1) $L_{dq(app)}$ at $i_d = 8A$ (2) $L_{qd(app)}$ at $i_q = 8A$ (3) $L_{dq(inc)}$ at $i_d = 8A$ (4) $L_{qd(inc)}$ at $i_q = 8A$.

3.4 Experimental setup

The experimental setup of the proposed VFM machine emulator system is shown in Fig. 3.9(a). Linear amplifiers are used to emulate the machine behavior. The linear amplifiers, AE-TECHRON®-7548, have a power sinking capability of 1.2 kVA and a bandwidth of 200 kHz [54]. Linear amplifiers are much more expensive as compared to switched amplifiers discussed in the previous chapter, but they offer a much higher bandwidth as compared to switched amplifiers. Hence, for the given specifications of a controller, linear amplifiers provide with the highest closed loop emulation bandwidth.

Three linear amplifiers are used in the machine emulator system, each emulating one phase of the machine. The three linear amplifiers are connected in a star-configuration, i.e., the neutrals of the three linear amplifiers are connected together. The high bandwidth provided by the linear amplifiers enables them to mimic various machine transient behavior. The linear amplifiers are connected to the driving inverter, with coupling inductances of 5 mH, on each phase. The driving inverter used is a standard two-level converter topology composed of IGBT switches (SKM50GB123D). The switching frequency chosen for the driving inverter is 5 kHz. Fig. 3.9(a) also shows a protection circuit developed for the system. This circuit isolates the linear amplifier from the driving inverter and blocks gating pulses to the driving inverter in the event of an over-current or an over-voltage fault, within the emulation system. In addition, an isolation transformer is used to connect the linear amplifiers to its supply grid. This is needed to ensure that there are no common mode or circulating currents flowing in the circuit.

Control for the linear amplifiers and the driving inverter are implemented on an OPAL-RT based real-time simulator (RTS), OP4510®, also shown in Fig. 3.9(a). As discussed earlier, the digital simulator time step needs to be minimized to ensure maximum emulation bandwidth. To achieve this, the machine emulator control, which comprises of the FEA based VFM machine model and current controllers, are both implemented on the FPGA board of the RTS. This enables a low time-step for the machine emulator controller implementation ($< 5\mu$s). The machine model used in the proposed machine emulator system uses a FEA lookup table data generated from MotorSolve®, and hence contains all machine magnetic and geometric data. The drive converter control, which is a basic vector control for a VFM drive is implemented on the CPU of the real-time simulator (OP4510). Since the current loop bandwidth of the driving inverter is quite low, a higher time step for the driving inverter control

(a)

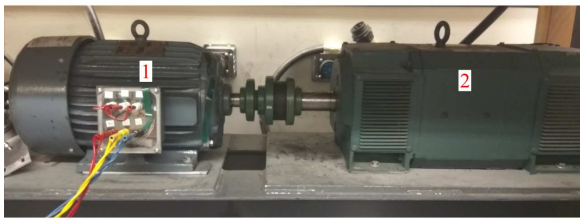

(b)

Fig. 3.9: (a) Experimental setup of the emulator system (1) Linear amplifiers emulating the VFM (2) Driving inverter (3) Controller for the VFM emulator (4) protection circuitry (5) link inductors and (6) isolation transformer; (b) Experimental setup of the VFM drive (1) The VFM machine (2) coupled DC dynamometer.

implementation (30 μs) suffices.

The results obtained from the VFM emulator system are compared with that obtained from a prototype VFM coupled to a DC dynamometer, shown in Fig. 3.9(b). This prototype machine is designed based on the FEA data shown earlier in Section 3.3 [52]. The coupled DC dynamometer is used to load the prototype VFM. The drive inverter and the controller for the prototype VFM drive and the VFM emulator system are maintained the same. To ensure a proper comparison between the results obtained from the emulator and that obtained from the prototype machine, the drive inverter has vector controlled implemented with the same controller bandwidths to ensure the machine (or emulated machine) operates at the required torque or speed.

3.5 Experimental results

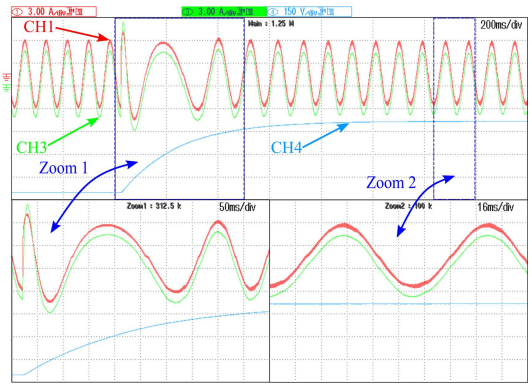

(a) Experimental results of emulator response for a step change in torque; CH1: emulated machine phase current, CH3 reference current for emulation generated within the real-time controller, CH4 emulated machine speed.

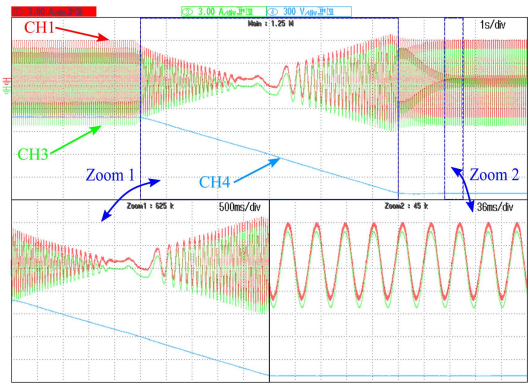

(b) Experimental results of emulator response for a step change in speed reference; CH1: emulated machine phase current, CH3: reference current for emulation generated within the real-time controller, CH4: emulated machine speed.

Fig. 3.10: Experimental results comparing emulator response against the machine model response [CH1: 3 A/div, CH3: 3 A/div, CH4, 150 rpm/div, Time scale: Main window 200 ms/div; Zoom1 50 ms/div; Zoom2 16 ms/div]

As mentioned in Section 3.4, the results obtained from the emulator are compared with that obtained from the prototype VFM drive. This comparison would prove; (a) the bandwidth sufficiency of the developed emulator system to emulate VFM transient conditions, (b) the accuracy of the machine model used for the purpose of emulation, and (c) adequate separation between the current loop bandwidth of the emulation system and the current loop bandwidth of the drive inverter system.

Fig. 3.10a and Fig. 3.10b are the experimental results obtained from the VFM emulator system for different control modes of the drive inverter. These results are essentially to prove the capability of the developed emulator system to emulate machines operating in different control modes. In Fig. 3.10a the drive inverter operates in torque control mode. A torque step command is given from a negative value to a positive value of half the rated torque. In Fig. 3.10b the drive inverter operates in speed control mode. The reference speed of the machine is gradually changed from a negative value to a positive value of half the rated speed. These results show the capability of the emulator system to operate in both control modes. CH3 (in Fig. 3.10a and Fig. 3.10b) is the current drawn by the VFM model within the RTS

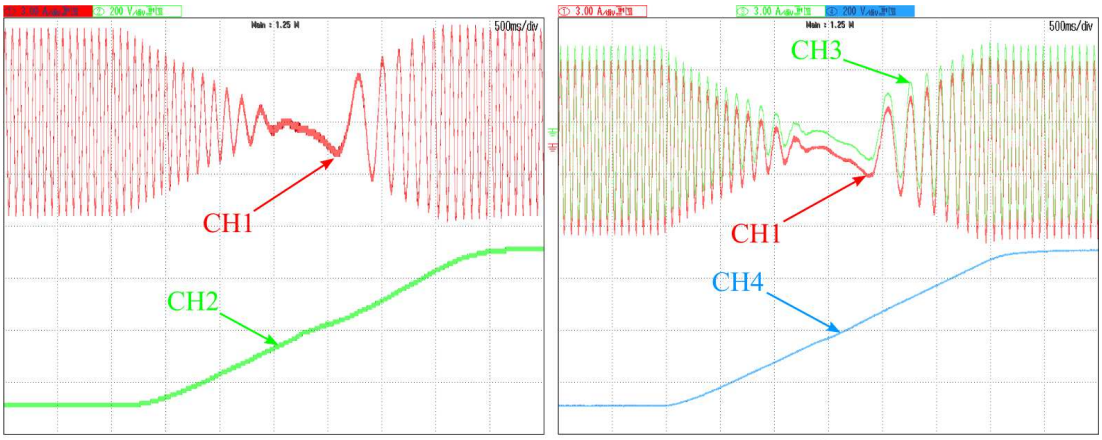

Fig. 3.11: Experimental results obtained for machine speed reversal (a) prototype VFM speed reversal, CH1: phase current, CH2: motor speed (b) emulated VFM speed reversal, CH1: emulated machine phase current, CH3: reference current for emulation system generated within the real-time controller, CH4: emulated machine speed. [CH1= 3 A/div, CH2= 200 rpm/div, CH4= 3 A/div, Time scale 500 ms/div]

environment. This is nothing but the current I_{motor_vir} indicated in Fig. 3.1. CH1 is the measured current drawn by the emulator system (I_{motor} shown in Fig. 3.1). A good match between CH1 and CH3 proves the current control operation of the emulating converter. CH3 and CH1 indeed overlap. They have been placed on different DC offsets to visibly differentiate between the two. In addition, Fig. 3.10a and Fig. 3.10b also show the zoomed versions to better visualize the transient response. The zoomed windows and regions of the zoom, are also shown in the same figures.

As discussed earlier, to validate the the proposed emulator system, experimental results pertaining to various machine transient conditions are obtained from the emulator system and the prototype machine and compared. Fig. 3.11 presents the results obtained for speed reversal of the prototype machine and the machine emulator. Fig. 3.12 presents results obtained when the load on the VFM is suddenly increased, leading to a drop in speed and a subsequent control back to its rated value. In addition, a step change in torque, from zero to half the rated value is applied for both, the prototype machine and the machine emulator system. Experimental results for this transient condition are shown in Fig. 3.13. All these cases are run when the machine is at its 100% magnetization level. Fig. 3.11, Fig. 3.12 and Fig. 3.13 clearly show that there is a close match between the results obtained from the prototype machine and the machine emulator system proving its accuracy. Fig. 3.11(b), Fig. 3.12(b) and

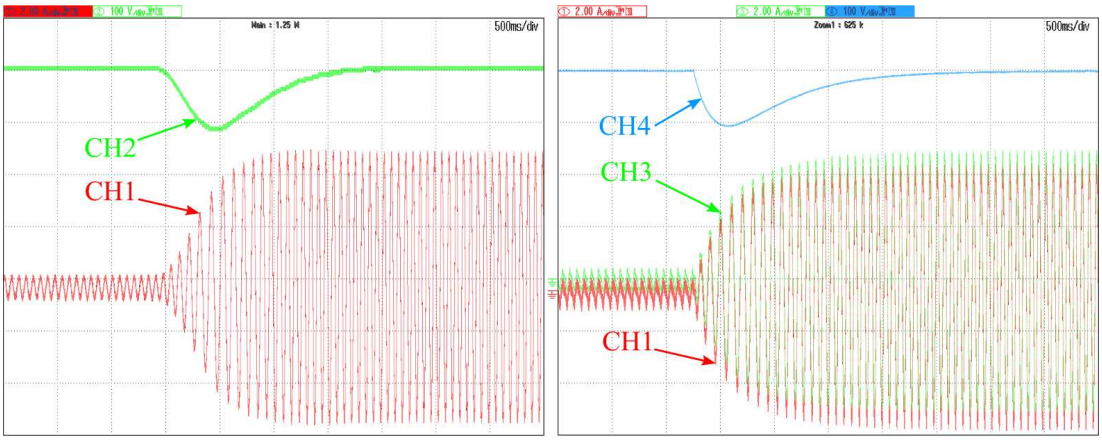

Fig. 3.12: Experimental results obtained for 100% magnetization level, (a) prototype VFM sudden load increase, CH1: phase current (Scale 3 A/div), CH2: motor speed (Scale 200 rpm/div) (b) emulated VFM sudden load increase, CH1: emulated machine phase current (Scale 3 A/div), CH3: reference current for emulation system generated within the real-time controller (Scale 3A/div), CH4: emulated machine speed (Scale 200 rpm/div). [Time scale: 500 ms/div]

Fig. 3.13(b) show both, the current drawn by the machine emulator system and the current drawn by the VFM machine model implemented in the RTS, on different DC offsets.

As mentioned earlier, air gap flux in a VFM can be controlled by changing the magnetization level of the magnets. This leads to a change in machine parameters. FEA simulations and measurements are performed for a different magnetization level, 75%, of the VFM. These look-up tables are used in the VFM machine model implemented in the RTS, to perform emulation of the VFM at this magnetization level. As in the earlier case, experimental results pertaining to various machine transient conditions are obtained from the emulator system and the prototype machine at this magnetization level. Fig. 3.14 presents the results obtained for speed reversal of the prototype machine and the machine emulator, and Fig. 3.15 presents results obtained when the load on the VFM is suddenly increased. It can be clearly seen that there is a close match between the results obtained from the prototype machine and the machine emulator system. Fig. 3.14(b) and Fig. 3.15(b) show both, the current drawn by the machine emulator system and current drawn by the VFM machine model implemented in the RTS, on different DC offsets.

Transient results presented in this section prove the bandwidth sufficiency of the proposed VFM machine emulator system. These transient results are compared with

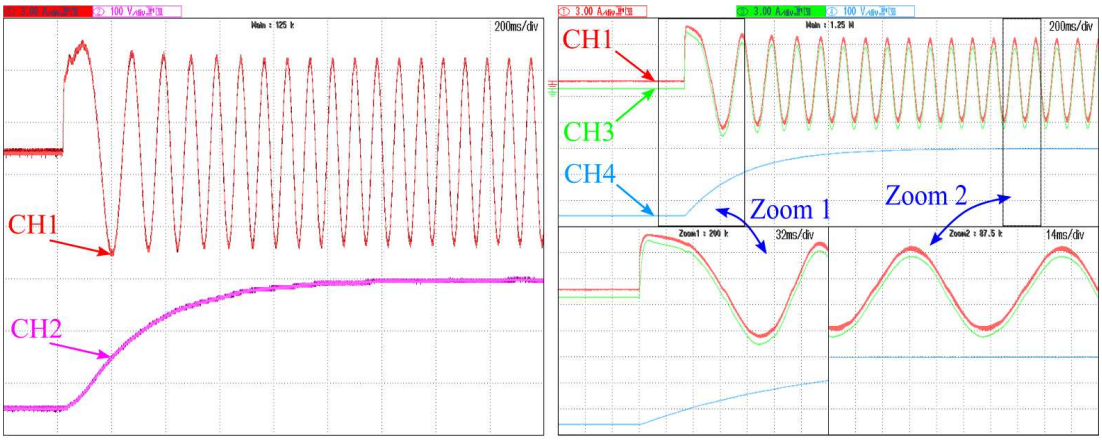

Fig. 3.13: Experimental results obtained for 100% magnetization level (a) prototype VFM torque step response, CH1: phase current, CH2: motor speed (Scale 200 rpm/div) (b) emulated VFM torque step response, CH1: emulated machine phase current, CH3: reference current for emulation system generated within the real-time controller, CH4: emulated machine speed. [CH1= 5 A/div, CH3= 5 A/div, CH4= 200 rpm/div, Time scale: Main window 200 ms/div; Zoom1 32 ms/div; Zoom2 14 ms/div]

that obtained from a prototype machine to ensure emulation accuracy. Results are also presented at different magnetization levels to highlight the flexibility of the proposed emulation system.

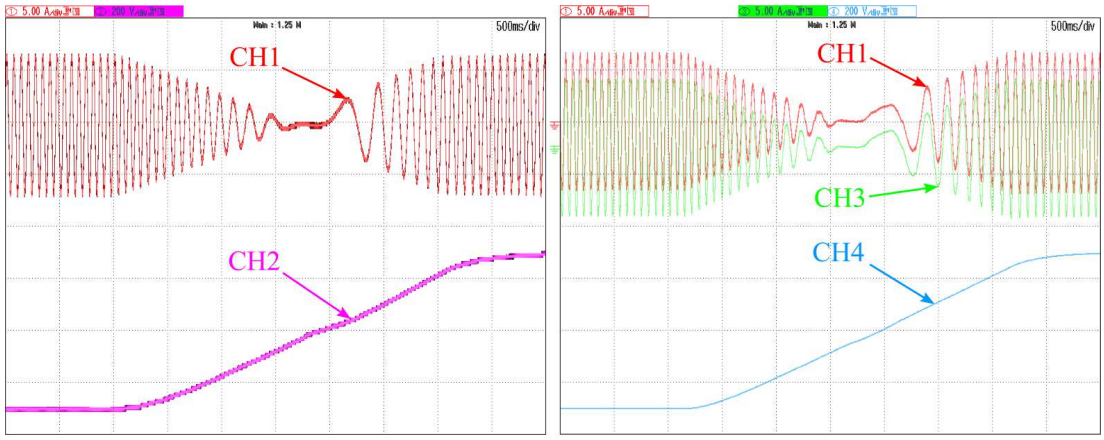

Fig. 3.14: Experimental results obtained for 75% magnetization level (a) prototype VFM speed reversal, CH1: phase current (Scale 5 A/div), CH2: motor speed (Scale 200 rpm/div) (b) emulated VFM speed reversal, CH1: emulated machine phase current (Scale 5 A/div), CH3: reference current for emulation system generated within the real-time controller (Scale 5A/div), CH4: emulated machine speed (Scale 200 rpm/div). [Time scale: 500 ms/div]

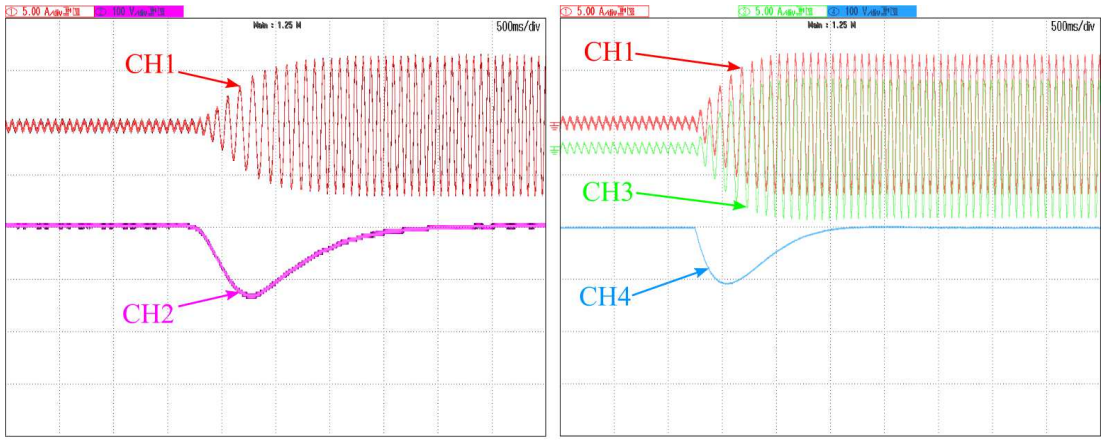

Fig. 3.15: Experimental results obtained for 75% magnetization level, (a) prototype VFM sudden load increase, CH1: phase current (Scale 5 A/div), CH2: motor speed (Scale 200 rpm/div) (b) emulated VFM sudden load increase, CH1: emulated machine phase current (Scale 5 A/div), CH3: reference current for emulation system generated within the real-time controller (Scale 5 A/div), CH4: emulated machine speed (Scale 200 rpm/div).[Time scale: 500 ms/div]

3.6 Summary

This chapter presented a power-hardware-in-the-loop (PHIL) based emulation variable flux machine (VFM) realized with the help of linear amplifiers. A high closed loop emulation bandwidth of 7.5 kHz was achieved through the use of a linear amplifier (which has a high open-loop bandiwdth of 200 kHz) and a low time step controller implementation ($< 5\mu s$). The main summarizing comments of this chapter are as follows.

A. Similar to the previous chapter, machine emulator system in this chapter uses flux and torque look-up tables obtained from an FEA tool as well. This again enables a high accuracy emulation which can account for various machine geometric and magnetic characteristics. In the specific case of a VFM, since the magnetization level of the magnetic can be changed, multiple FEA look-up tables will need to be stored for the machine model at different states. This chapter showed the emulation of a VFM at two different magnetization states.

B. The emulator system presented in this chapter used high performance high bandwidth linear amplifiers for the emulation. Control design of the machine emulator and its implementation is looked at in detail to achieve a high current control bandwidth of 7.5 kHz. This high emulation bandwidth results in a high emulation accuracy as well. Furtherore, a high emulation bandwidth also means that drive inverters with high current control bandwidth can be tested with this emulation system.

C. Multiple experimental results for various machine transient conditions were presented in this chapter. A close match between the results obtained from the emulated machine and the prototype machine, proves the accuracy of the emulation system and also validates the bandwidth sufficiency to emulate these transient behaviors.

The developed emulator system will be used to emulate a machine for several drive inverter transient behavior (faults) in the next chapter. This will again prove the adequacy of the achieved emulation bandwidth in this chapter. Modifications to the emulator control will also be presented to enable fault emulation in the next chapter.

Chapter 4

Machine emulation to investigate driving inverter faults

One of the advantages of machine emulation, as discussed in Chapter 1, is to emulate machine behavior in the event of faults. Since the machine is emulated, these fault conditions can be tested more freely, with a reduced concern of equipment (machine) damage. Several publications in the literature, have studied CHIL simulations in the event of drive inverter faults [59–62]. However, there is no reported literature studying machine emulation, for such transient fault conditions. Driving inverter faults result in sharp transient events in the current drawn by the emulated machine. Emulation of such transient condition necessitates, (i) a detailed machine model to ensure emulation accuracy, and (ii) a high emulation bandwidth to ensure tracking during transient conditions.

This chapter validates the emulator system and its control presented in Chapter 2 and Chapter 3 for emulation machine behavior in the event of driving inverter faults. In the process of implementing the emulator control for drive inverter faults, this chapter also addresses the following improvements:

- A PI controller for emulator current control was used in the earlier chapters. During drive inverter faults, the current drawn by the emulator system consists of several lower order harmonics and a PI controller would not suffice for zero steady state (or low steady state error) for all lower order harmonics. This chapter proposes using resonant controllers tuned at the resonant frequencies of the corresponding lower order harmonic current, in addition to the PI controller for achieving a low steady state error for all frequencies of interest.

- The possibility of maintaining current control in the event of driving inverter faults ia also explored in this chapter. Suitable modifications are proposed to the emulator control to ensure safety of the emulator system and the driving inverter.

4.1 System description

A schematic of the machine emulator is shown again in Fig. 4.1. A current control strategy is used to ensure that the current drawn by the emulator system is equal to the current outputted by the machine model implemented in the real-time simulation environment. To achieve this, the driving inverter voltage, V_{inv} is measured and inputted to a look-up table based machine model implemented within the real-time simulator environment. This machine model generates a virtual current reference, I_{motor_vir}. An emulator control is subsequently designed to ensure that the current drawn by the machine emulator, I_{motor} is equal to the virtual current reference generated by the machine model, I_{motor_vir}. The drive inverter control, if vector control is used, also operates in current control mode. It's control objective is to inject currents (I_{motor}) into the emulated machine so that the emulated machine operates at the required speed or torque as specified by its controller.

Chapter 3 also discussed that to ensure a stable and accurate machine emulation, the emulator current control needs to be at least five times faster than the current control of the driving inverter. PI controllers are used for the emulator control. The controller and the virtual machine model are both implemented on the FPGA of the real-time simulator to minimize the controller sampling time and hence maximize emulation bandwidth. A current emulation bandwidth of 7.5 kHz is achieved for the machine emulator.

4.1.1 Drive inverter faults

Several driving inverter faults can occur in a traction system. The performance of the traction motor in these fault conditions has been detailed in several publications [41–44]. These faults can be broadly characterized as driving inverter short-circuit faults and driving inverter open-circuit faults [41–44]. In the event of short circuit faults, large currents are drawn by the traction motor or the drive inverter, thus activating the over-current trip and shutting down the system. In open-circuit faults (resulting due

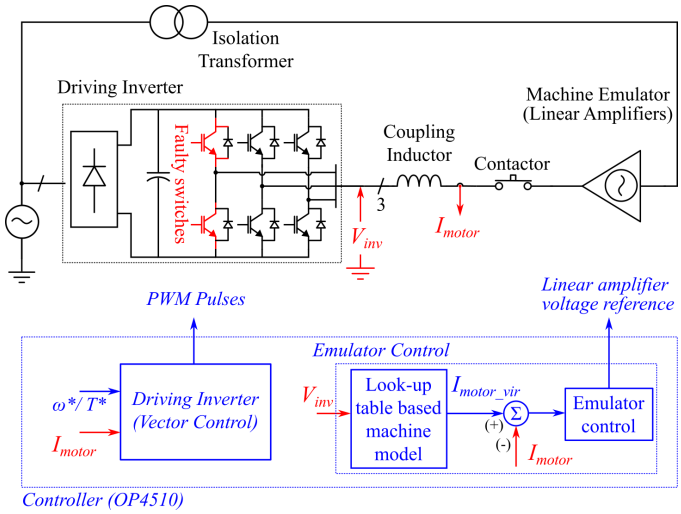

Fig. 4.1: Schematic diagram of the PHIL machine emulation system

to a gate-drive failure) on the other hand, the traction drive can continue to operate but at a reduced power capability.

With respect to emulation, a short-circuit fault in the driving inverter will lead to a high currents drawn by the emulator, which would result in its over-current limit action protecting both systems (the emulator and the driving inverter). Hence, the emulation of such faults is of less interest. The driving inverter fault, that is of particular concern, especially since current control is being used for the emulator control, is a device open-circuit fault of the driving inverter. Furthermore, as mentioned earlier, in the event of a gate-drive failure fault of the driving inverter, the drive is still in operation at reduced power. Since the drive and the emulator are still operational for such faults, it is necessary to study the effectiveness of emulation for these operating conditions. This chapter will investigate the effectiveness of machine emulation to emulate machine behavior in the event of driving inverter open-circuit faults caused by gate-drive failure of one or more switches.

Consider a gate drive fault in the upper switch of A-phase as shown in Fig. 4.4. In the event of this fault, the IGBT of the upper switch does not conduct any current. During this fault, if the polarity of the A-phase current is positive (currents measured coming out of the drive inverter), it is clamped to zero, whilst the negative half cycle of the current is relatively unaffected. The DC offset created in A-phase needs to be accommodated in the currents of B-phase and C -phase, hence these currents will have DC offsets as well. There will therefore be fundamental frequency torque pulsations which will lead to speed oscillations when the machine is being controlled

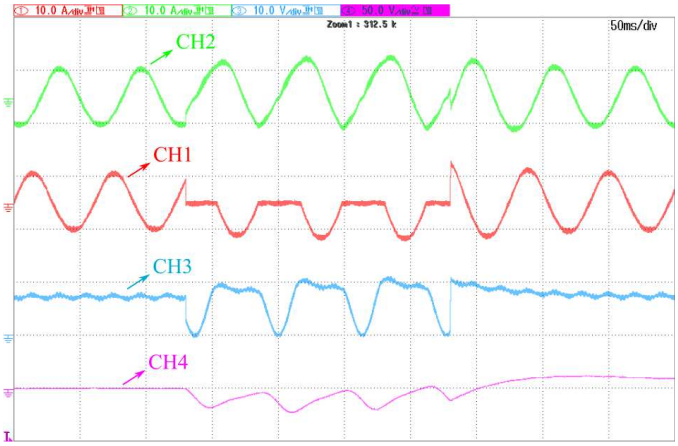

Fig. 4.2: Simulation results for a fault in the upper phase of A-phase; CH1 current in the faulted phase of the inverter (Scale 10 A/div), CH2 current in the healthy phase of the inverter (Scale 10 A/div), CH3 Torque ripple due to the fault (Scale 10 Nm/div), and CH4 speed oscillations due to the fault measured in AC coupling mode (Scale 50 rpm/div)

in torque-control mode. Simulation results obtained for this fault condition is shown in Fig. 4.2. The DC offsets in the current, the corresponding fundamental frequency torque pulsation and speed oscillations are evident from the results. A fault in the lower switch of the A-phase will yield similar results, the only difference will be that the positive half of the A-phase current will be relatively unaffected and the negative half will be clamped to zero. A theoretical background explaining the current waveform for the corresponding driving inverter faults are presented in [41].

Consider now a fault on both gate units of switches of A-phase as shown in Fig. 4.1. By extension of the description presented above, the positive and negative half of the currents will both be clamped to zero. This will force the currents in the two healthy phases to be equal and opposite to each other. Such a fault will again lead to severe torque pulsations and speed oscillations. Simulation results presented in Fig. 4.3 support this. The last fault considered is a complete gate unit failure wherein all the switches of the inverter are turned off. The currents in all three phases immediately fall to zero since the diodes in the drive inverter are all reverse biased. The measured output voltage of the driving inverter terminals should now be equal to the back-emf of the machine. Based on the inertia of the emulated machine, it should come to a standstill eventually.

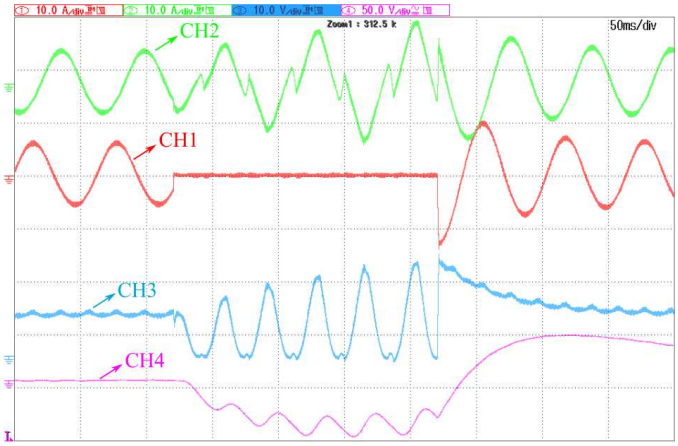

Fig. 4.3: Simulation results for a fault in both switches of A-phase; CH1 current in the faulted phase of the inverter (Scale 10 A/div), CH2 current in the healthy phase of the inverter (Scale 10 A/div), CH3 Torque ripple due to the fault (Scale 10 Nm/div), and CH4 speed oscillations due to the fault measured in AC coupling mode (Scale 50 rpm/div)

4.2 Modifications to emulator operation during drive inverter open-circuit faults

The schematic diagram of the PHIL based machine emulator system is shown in Fig 4.1. As discussed earlier, the terminal voltage of the drive inverter is measured and input to the look-up table based machine model which subsequently generates a current reference for the emulator current control. This section looks into the feasibility of continuing with the same emulator control methodology and voltage sensing procedure even during drive inverter faults.

4.2.1 Drive inverter terminal voltage sensing

Terminal voltage is sensed using an onboard analog-digital (ADC) card, controlled by the FPGA board of the OP4510 [55]. The card has a conversion time of $2.5\mu s$. This essentially translates to a delay of $2.5\mu s$ for voltage sensing. Furthermore, the voltage sensors have a high bandwidth of 100 kHz. Hence, during normal operation, when the inverter switching frequency is low (considered 5 kHz in this chapter), there is negligible delay and filtering to the measured switching voltage. This implies that the current reference generated by the machine model for emulation, is an accurate representation of the current that would be drawn by a physical machine prototype.

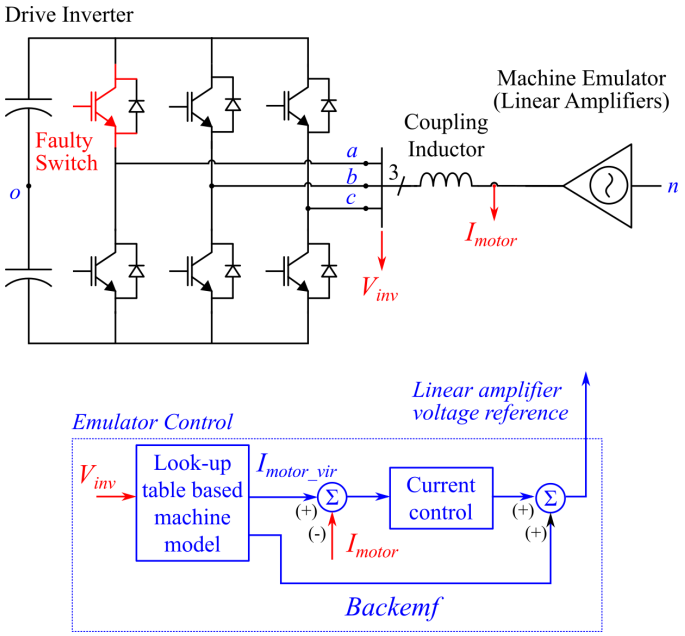

Fig. 4.4: A schematic of a faulty drive inverter connected to a machine emulator

Hence, this methodology of voltage sensing for emulation, works during the normal operation of the drive inverter.

With reference to Fig. 4.4, the voltages measured are the driving inverter line-line voltages, v_{ab}, v_{bc} and v_{ca}. These line voltages are in-turn defined as the difference between the corresponding drive inverter pole to dc link mid-point voltages, v_{ao}, v_{bo} and v_{co}. Drive inverter faults were shown in Fig. 4.2 and Fig. 4.3. These results show that during drive inverter faults, the current is clamped to zero in the affected phase. Hence, v_{ao} or v_{bo} or v_{co} could be floating. This implies that the corresponding line-line voltages, with the affected phase are not directly defined as well. Fig. 4.4 clearly shows that the emulator control is dependent on the drive inverter terminal voltage sensing. Hence, it is important to prove that the terminal voltage is "defined" during fault conditions to ensure the possibility of the emulator control strategy shown in Fig. 4.4.

Consider the fault marked in the top switch of A-phase, as shown in Fig. 4.4, A-phase current i_a is zero during the positive half cycle. In this duration the voltage v_{ao} isn't defined and hence the line-line voltages v_{ab} and v_{ca} cannot be defined directly as well. The machine emulator neutral to drive inverter pole mid-point voltage, v_{no} can be represented as (12).

$$v_{no} = \frac{v_{ao} + v_{bo} + v_{co}}{3} \tag{12}$$

$$v_{ao} = v_{no} + e_{an} \tag{13}$$

Equation (13) is valid when A-phase is clamped to zero. e_{an} is the emulated back-emf of the machine A-phase. Combining (12) and (13), the A-phase pole voltage during fault when $i_a \not< 0$ is given by (14). The faulted phase pole voltage can therefore be defined as a function of the corresponding phase back-emf of the emulated machine, and the pole voltages of the other two healthy phases of the drive inverter.

$$v_{ao} = \frac{3}{2}\, e_{an} + \frac{1}{2}\, v_{bo} + \frac{1}{2}\, v_{co} \tag{14}$$

The line-line voltage during the fault and when $i_a \not< 0$ can then be represented as (15) and (16), respectively.

$$v_{ab} = \frac{3}{2}\, e_{an} - \frac{1}{2}\, v_{bo} + \frac{1}{2}\, v_{co} \tag{15}$$

$$v_{ca} = \frac{1}{2}\, v_{co} - \frac{3}{2} e_{an} - \frac{1}{2}\, v_{bo} \tag{16}$$

Hence, it is clear that line-line voltages can be defined even during fault conditions, as a function of the back-emf of the emulated machine and the healthy pole voltages of the drive inverter. Therefore, voltage sensing during fault conditions, is possible for the emulator control shown in Fig. 4.1. Similar expressions for the line-line voltages, as shown in (15) and (16) can also be developed for other fault conditions discussed earlier, to validate the suitability of current control for machine emulation. During the fault where there is a complete gate-unit failure, the inverter pole voltages and subsequently the line-line voltages can be defined as a function of the machine back-emfs alone.

4.2.2 Drive inverter current controller improvement

In the event of faults as discussed in the previous subsection, the currents drawn from the drive inverter are no longer sinusoidal. The affected phase current is either clamped to the positive half cycle or the negative half cycle or both, during the event of these faults. Hence the three phase currents can have several lower order harmonics. This would mean that the *dq* currents would have several lower order harmonics as well. The closed loop bandwidth with the controller proposed in Chapter 3 is shown in Fig. 4.5. The closed loop gain of this controller is 0 dB only at DC. At higher frequencies, this closed loop gain is less than zero, as low as -3 dB at the designed

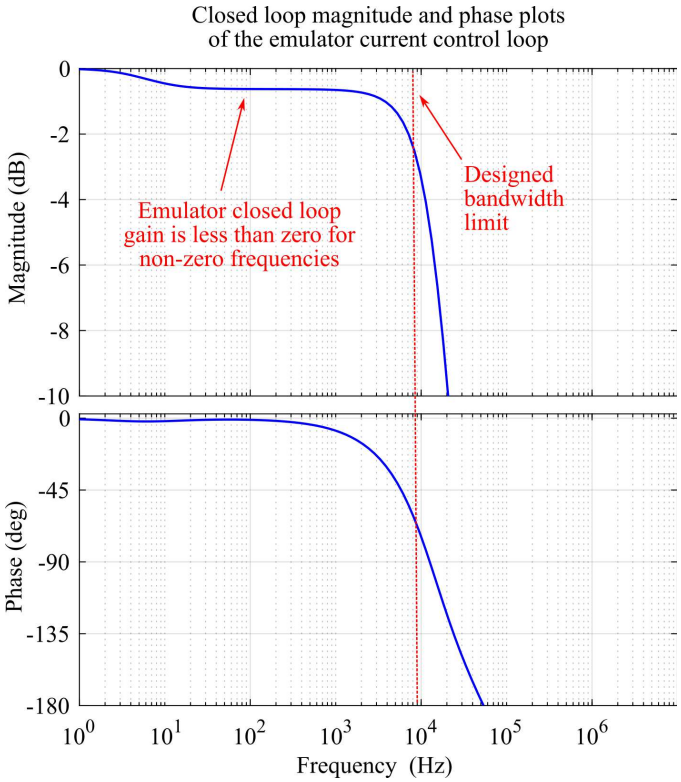

Fig. 4.5: Closed loop magnitude and phase plots for the emulator current control

bandwidth limit. This implies that for these frequencies there would be a steady state error. Since emulated currents during the drive inverter faults have several lower order harmonics, using the same controller would result in a poor emulation accuracy.

The harmonic spectrum of the q-axis current in the event of this fault is shown in Fig. 4.6. As can be seen, there are several lower order harmonics. The designed controller has 0 dB closed loop gain only for DC, therefore there will be zero steady state error for the DC component alone. To address the requirement of a zero steady state error at frequencies other than DC, the control structure needs to be changed.

Proportional resonant (PR) controllers can present a high open-loop gain for selective frequencies required. Such controllers have often been used for grid-connected applications wherein the frequency of the grid is fixed at 50 Hz or 60 Hz [63–66]. In drive applications the fundamental frequency changes and this complicates the use of PR controllers, wherein they need to adapt and change their resonant frequency depending on the fundamental frequency of operation. The emulator controller can be modified to include both, the existing PI controller to obtain zero steady state error for DC operation and resonant controllers tuned at the specific harmonic order for

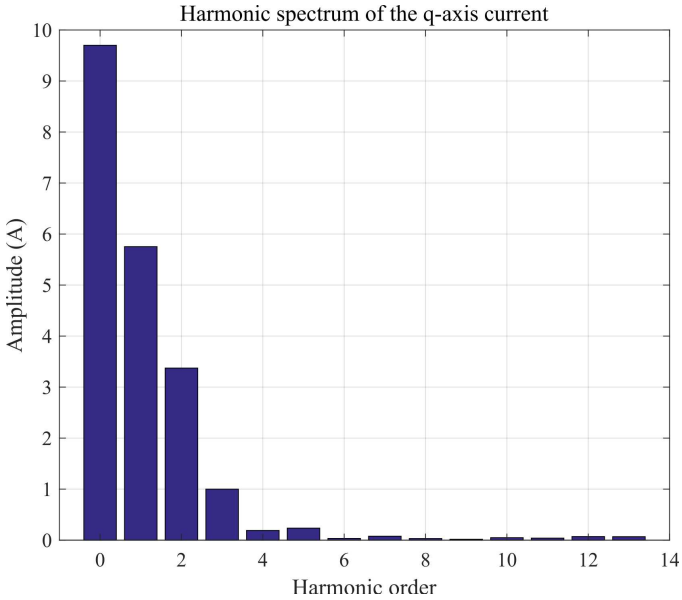

Fig. 4.6: Harmonic spectrum of the q-axis current in the event of an A-phase top switch fault

which zero steady state error is required. The structure of the proposed controller modification is illustrated in Fig. 4.7(a).Such a proposed controller modification would achieve the objectives of attaining zero steady state error at DC and other lower order harmonic frequencies of interest.

As mentioned earlier, since the fundamental frequency of the drive operation changes, the resonant controller cannot be represented as a static transfer function but rather an adaptive one which changes its resonant frequency based on the fundamental frequency of operation. For a synchronous machine drive such as a PMSM, the machine speed is equal to the synchronous speed as well. Therefore, based on the speed of the emulated machine and its number of pole pairs, the fundamental frequency of operation of the drive can be easily obtained. This is shown in Fig. 4.7(b). As the machine accelerates and the fundamental frequency changes, the resonant controller transfer function automatically changes to ensure that it still acts for the harmonic orders of interest. With the machine emulated being a PMSM, it always operates at a synchronous speed i.e., the machine speed is always equal to the synchronous speed.

From the harmonic spectrum of the q-axis current (shown in Fig. 4.6) it is evident that there is DC, fundamental, second and third harmonic components. The PI controller would be able to achieve zero steady state error for the DC component, but a resonant controller would be required at the fundamental frequency, second

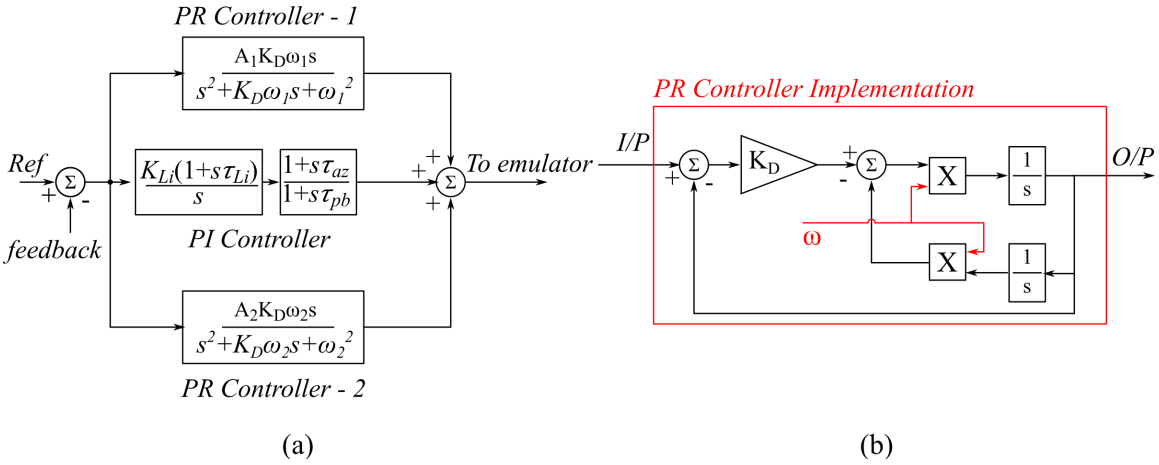

Fig. 4.7: (a) Modified controller to ensure accurate emulation during fault conditions (b) Implementation of resonant controller to be adaptive with respect to fundamental speed

harmonic, and the third harmonic. This proposed modified controller is shown in (17), where A_1-A_3 are the gains of the three resonant controllers, K_{D1}-K_{D3} are the damping factors of the three resonant controllers and, ω_1-ω_3 are the resonant frequencies of the three resonant controllers. With the controller implementation shown in Fig. 4.7(b), these gains can be changed in relation with the machine fundamental frequency.

$$C^*(s) = \frac{K_{PI}\,(1+s\,\tau_{PI})}{s}\frac{1+s\,\tau_{az}}{1+s\,\tau_{pb}} + \frac{A_1\,K_{D1}\,\omega_1\,s}{s^2+K_{D1}\,\omega_1\,s+\omega_1^2} + \frac{A_2\,K_{D2}\,\omega_2\,s}{s^2+K_{D2}\,\omega_2\,s+\omega_2^2} + \frac{A_3\,K_{D3}\,\omega_3\,s}{s^2+K_{D3}\,\omega_3\,s+\omega_3^2} \tag{17}$$

$$EMU(s) = C^*(s)\,G\,e^{-sT_c}\,e^{-sT_d}\,\frac{\frac{1}{R_f}}{1+s\,\frac{L_f}{R_f}}\,\frac{1}{1+s\,T_{fi}} \tag{18}$$

The rated speed of the machine emulated in this chapter is 1200 rpm, implying that its rated fundamental frequency is 40 Hz. At this rated frequency operating point, the dq axis current harmonic components should be at DC, fundamental, second and third harmonics for the A-phase top switch driving inverter fault, as shown earlier in Fig. 4.6. The resonant controllers need to therefore be designed for the frequencies of 40 Hz, 80 Hz and 120 Hz, in addition to the existing PI controller which is achieving zero steady state error for DC component of the dq-axis currents. With the new controller shown in (17), the open loop transfer function obtained for the emulator current

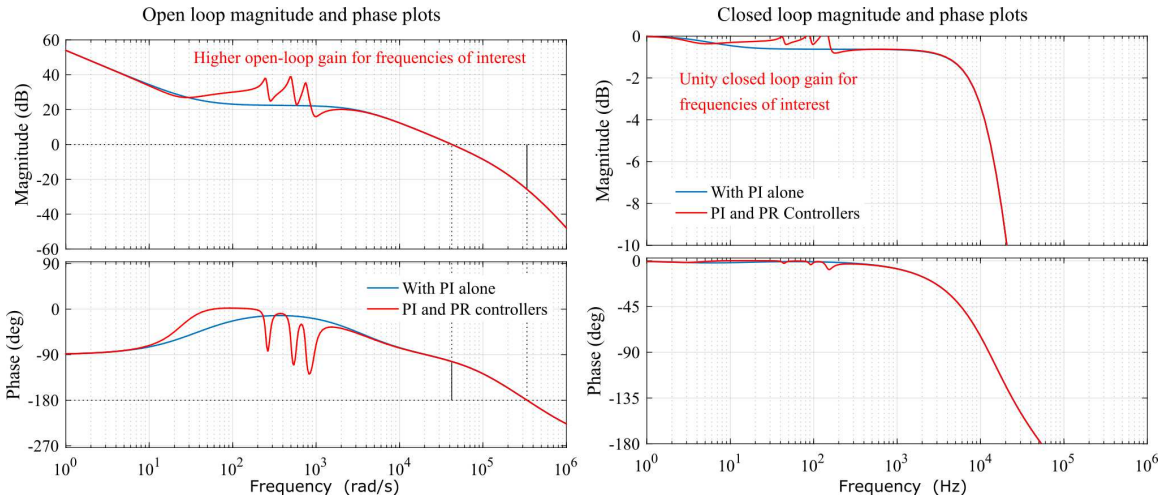

Fig. 4.8: (a) Open-loop magnitude and phase plot for the emulator current control loop (b) Closed-loop magnitude and phase plot for the emulator current control loop

control loop is shwon in (18). The open-loop and the closed loop magnitude and phase plots for the emulator current control loop are shown in Fig. 4.8. A comparison with the proposed controller of this chapter with the controller presented earlier in Chapter 3 is also presented in the same figure. The open-loop magnitude plot of Fig. 4.8(a) shows that the proposed controller of this chapter adds around 20 dB gain to the frequencies of interest, i.e., 40 Hz, 80 Hz and 120 Hz. This would imply a lower steady state error for these frequencies. Furthermore, the additional resonant controllers added effectively modify the open-loop magnitude and phase plots only around the frequencies of interest. The closed loop gain margin, phase margin and the bandwidth still remains the same. The closed loop magnitude plot shown in Fig 4.8 further supports the benefit of using resonant controllers. As can be seen from this figure, the closed loop gain around the frequencies of interest is 0dB, implying that there will be zero steady state error in the dq-axis emulator current control loops for DC, fundamental, second harmonic and the third harmonic.

The proposed control will therefore lead to a high accuracy of emulation even for drive inverter fault conditions, during which there are several lower order harmonic components. Experimental results presented in Section 4.4 provides the validation. The design exercise showed the magnitude and phase plots with resonant controller only for a fundamental frequency of 40 Hz. However, the resonant frequency of the resonant controllers can be easily changed based on the machine fundamental frequency by using the representation shown earlier in Fig. 4.7(b). The fundamental

frequency is measured my measuring the speed of the machine. Therefore, when the machine starts up, the resonant frequencies of the resonant controllers automatically change as the machine accelerates.

4.2.3 Drive inverter safety while emulating machine behavior for drive inverter faults

The earlier section presented PI and resonant controllers for emulator current control. Essentially during current control, the current drawn by the machine emulator is controlled to be equal to the reference current outputted by the machine model. Fig. 4.4 showed that the machine back-emf is added as a feed-forward term, but the emulator still operates in current control. During drive inverter fault conditions, for one switch or two switches, this current control can still be maintained without any risk of drive inverter damage. The current reference reduces to zero during the half cycle of current that is clamped to zero. The emulator control action and its high and bandwidth and selective frequency action, ensures that the current drawn by the emulator is clamped to zero during this period as well. Section 4.4 will present experimental results to prove the emulator operation during these fault conditions.

However, in the event of a complete gate-unit failure, the drive inverter operates as a diode-bridge rectifier. A diode bridge rectifier allows power flow only from its AC side to its DC side (i.e. from the emulator side to the DC bus side of the driving inverter). Therefore, maintaining current control for the emulator, post-fault, might end up charging up the DC bus of the drive inverter. This would damage the drive inverter. Furthermore, the emulated machine behavior would not be similar to a prototype machine experiencing this same type of fault. Simulation results explaining the same are shown in Fig. 4.9. As can be seen, as soon as the fault occurs, the drive inverter is converted to a diode bridge rectifier and the current should fall to zero immediately. This is visible in the results as well. However, a sensor non-ideality, such as an offset, would make the error to the PI regulator non-zero. Thus, the PI regulator will integrate this error and would continually increase the reference to the machine emulator. Eventually the output voltage of the emulator will forward bias the drive inverter diodes and start charging the DC bus capacitance of the drive inverter. Without an immediate disconnection of the driving inverter upon this fault detection, there could be damage to the driving inverter. Furthermore the results also clearly show that the emulated speed of the machine keeps increasing in the opposite direction

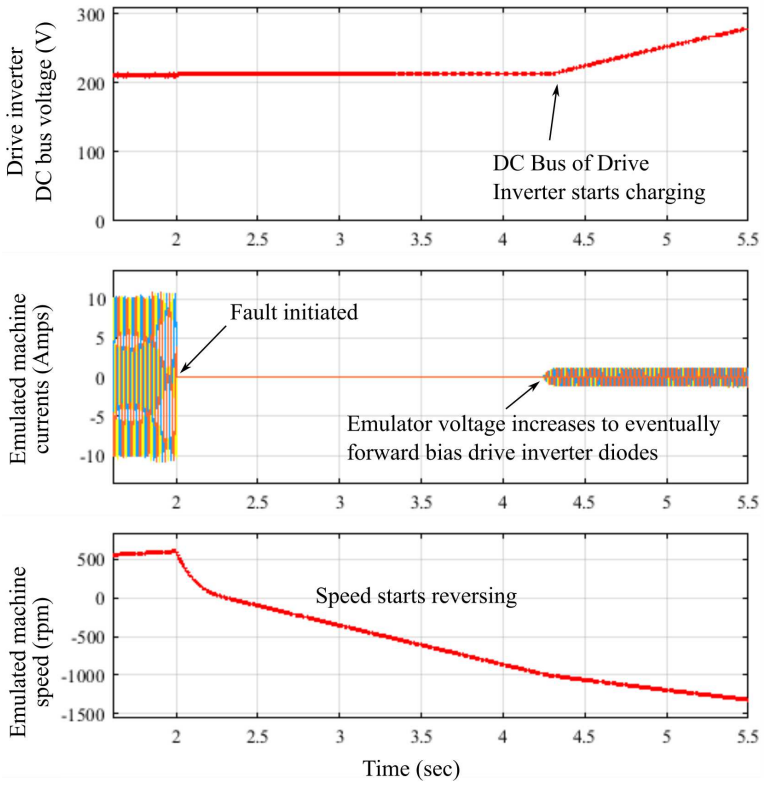

Fig. 4.9: Drive inverter voltage increase and inaccurate emulation for the case of complete gate-unit failure, when emulator current control is sustained

subsequent to the fault. It is also clear from Fig. 4.10 that the emulated voltage of the machine, post fault, is not equal to the back-emf of the machine, which would be the case when a physical prototype machine experiences such a fault. Therefore, looking at Fig. 4.9 and Fig. 4.10, it is clear that current control cannot be maintained during the event of this particular fault. There is hence a necessity to switch to voltage control mode during the event of this particular fault.

Looking at Fig. 4.4, the emulator is operating in current control mode. But, the back-emf if given directly as a voltage reference of the power amplifier (bypassing the current controller), converts the emulator to operate in voltage control mode. The first step is to detect this fault. There is no communication between the drive inverter controller and the emulator controller, therefore there is no possibility to communicate to the emulator that a fault has occurred in the driving inverter sensing its gating signals. The emulator needs to sense the fault by measuring its currents and the emulated machine model signals only. This complicates the process of fault detection.

During this fault, two things happen at the emulator end, (a) the measured

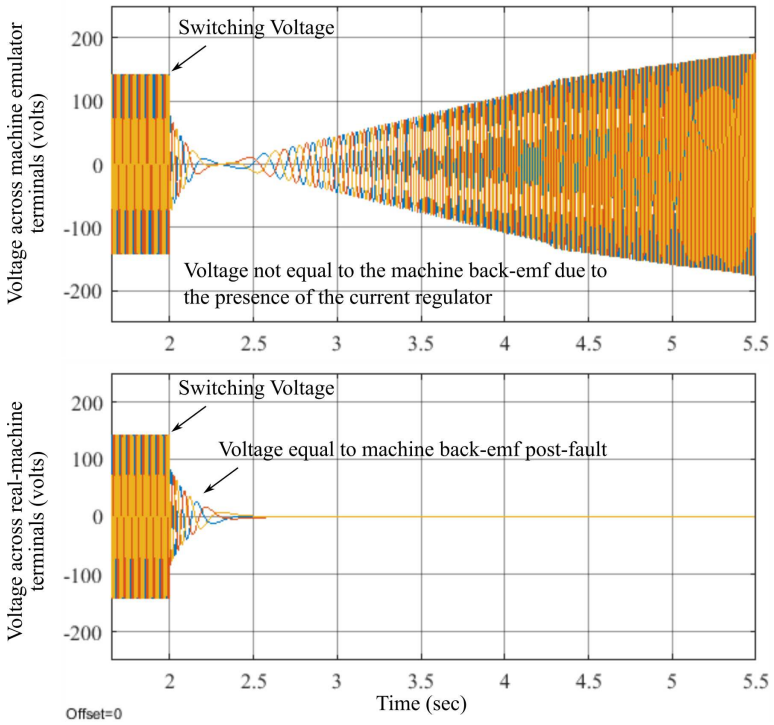

Fig. 4.10: Voltage across the emulator terminals compared with the voltage across real machine terminals during the event of a gate drive failure of the drive inverter

current reduce to below a certain threshold value (threshold value decided based on the machine switching ripple current), and (b) the speed of the emulated machine reduces. Condition (a) alone could occur at no-load operation of the emulated machine. Condition (b) alone could be satisfied if the machine speed reference changes to a lower value. But (a) and (b) together will be satisfied only when the complete gate-unit failure of the drive inverter occurs. A simple algorithm to detect this fault is shown in Fig. 4.11. This algorithm ensures that both the conditions discussed above are satisfied.The main advantage of this fault detection algorithm is that it does not require any communication between the drive inverter controller and the emulator controller. It solely detects faults based on the measured currents at the emulator end, alone.

Taking this fault detection algorithm into account, the emulator control described in Fig. 4.4, can be modified. As mentioned earlier, the emulator control should switch from current control to voltage control subsequent to detection of the drive inverter gate unit failure. This is illustrated in Fig. 4.12, wherein the fault detection from Fig. 4.11 generates a signal to transfer reference generation for the emulator. In case of

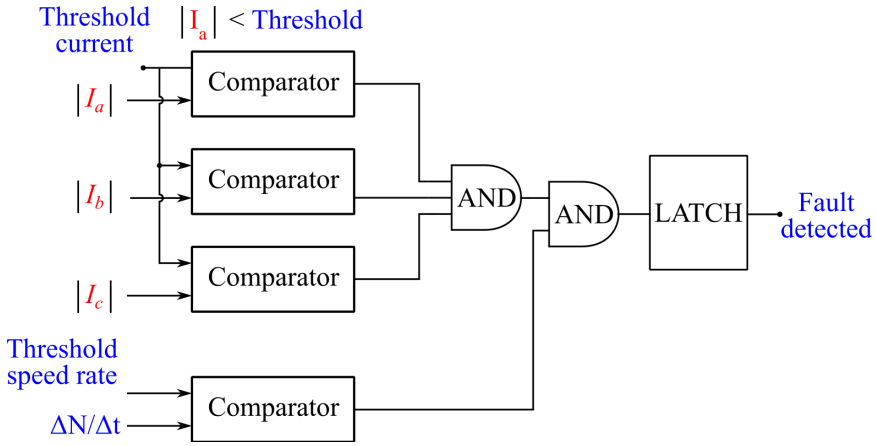

Fig. 4.11: A fault detection algorithm to detect complete gate-unit failure of the driving inverter based on measured emulated currents and emulated machine speed.

the fault, the current controller is disabled, and only the machine back-emf generates a direct voltage reference for the machine emulator, thus transferring from the current control mode to voltage control mode subsequent to the fault detection. The algorithm can also be extended to other three phase open-circuit faults of the system such as the opening of a breaker connecting the driving inverter and the machine emulator.

Experimental results will be presented in Section 4.4 to validate the operation of this fault detection algorithm for the drive inverter complete gate unit failure fault. Experimental results for emulator operation in current control for other gate-drive failure faults will be presented in Section 4.4 as well.

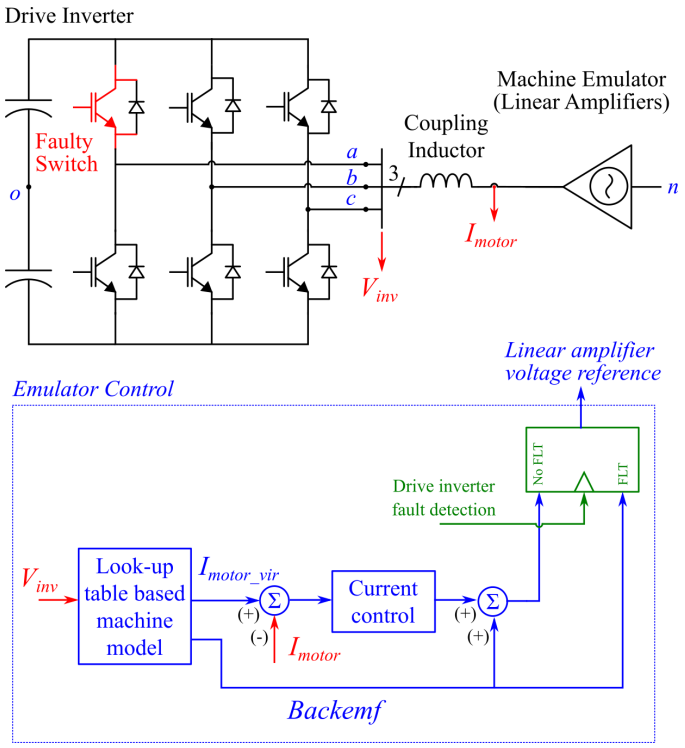

Fig. 4.12: Modified controller implementation for the emulator taking the fault-detection algorithm adn the controller mode changeover into account

4.3 Experimental setup

The experimental setup remains the same as discussed in Chapter 3 and hence it is not repeated here. High-performance linear amplifiers are used along with a low time-step controller implementation to ensure a high closed loop current control (emulation) bandwidth of 7.5 kHz. The results obtained from the emulator setup are compared against a $220-V$, 1300 rpm surface mounted PMSM coupled with a DC dynamometer, to very proposed emulator control and mode accuracy and utility.

4.4 Experimental results

This section presents experimental results for the emulation of a PMSM in the event of driving inverter faults. In order to first validate that the presence of resonant controllers does not affect the transient response of emulator, experimental results for a step torque command change are shown in Fig. 4.13. The torque changes from a negative reference value to a positive one. The speed of the machine changes according

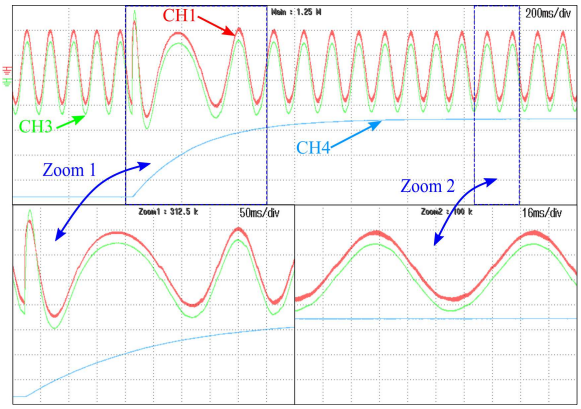

Fig. 4.13: Experimental results of emulator response for a step change in torque; CH1: emulated machine phase current (Scale: 5 A/div), CH3 reference current for emulation generated within the real-time controller (Scale: 5 A/div), CH4 emulated machine speed.Experimental results comparing emulator response against the machine model response (Scale: 200 rpm/div) [Time Scale 200 ms/div]

to the load. The results show that the emulated current is capable of tracking the reference machine model current during the entire range of change of changing speed.

For the various driving inverter faults discussed earlier in this chapter, experimental results are presented to prove the accuracy and utility of the proposed emulator control in the event of these transient conditions. The drive inverter is operating in torque control during the entire duration of operation. The speed at which the machine rotates depends on the load torque which is either applied by a DC dynamometer for the prototype PMSM, or a mathematical model for the emulated PMSM.

Fig. 4.14 presents the experimental results obtained for A-phase top switch gate drive failure of the driving inverter. As discussed earlier, the switch does not turn on and hence the current gets clamped to zero during the negative half cycle, in the faulty phase. The results obtained for the faulty driving inverter feeding a prototype PMSM and the emulated PMSM are shown in Fig. 4.14(a) and Fig. 4.14(b), respectively. Current control is maintained for the emulator during the event of this fault. The machine model outputs an appropriate current reference to ensure machine emulation during this transient condition. Furthermore, the proposed control with multiple resonant controllers assisting the PI controller along with the detailed machine model, ensures an accurate machine emulation, which is evident comparing the two results. To perform a more detailed comparison the harmonic spectra of the current drawn by the faulty drive inverter leg when connected to a prototype machine and when connected to the emulator is presented in Fig. 4.15. As mentioned earlier, the currents

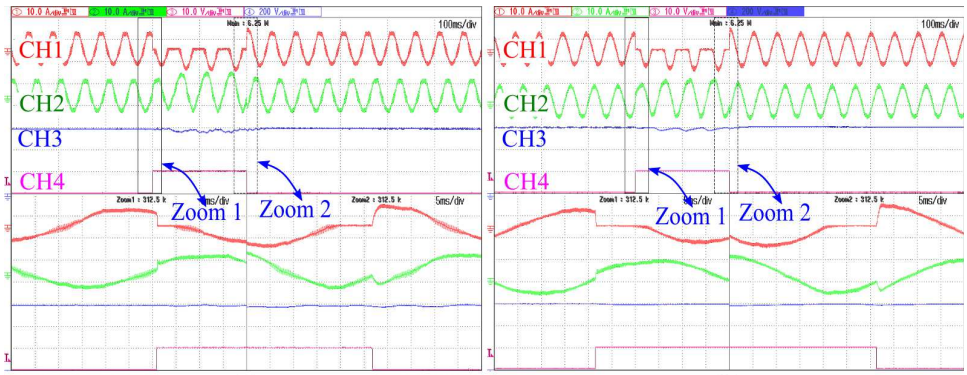

(a) (b)

Fig. 4.14: Experimental results obtained for A-phase top switch gate drive fault of the driving inverter (a) prototype PMSM being fed by the faulty drive inverter, and (b) emulated PMSM being fed by the faulty drive inverter. CH1: A-phase current (Scale 5 A/div), CH2: B-phase current (Scale 5 A/div), CH3: speed of the PMSM (Scale 200 rpm/div), CH4: fault indication [Time scale: 100 ms/div].

have several lower order harmonics during fault. A good match between the two harmonic spectra, proves the accuracy of the machine model used for emulation and the adequacy of the proposed controller for performing this emulation.

Fig. 4.16 presents experimental results obtained the gate drive failure of both switches in the A-phase. In the event of this fault, the faulty phase current is completely clamped to zero. Fig. 4.16(a) and Fig. 4.16(b) present the results obtained from the prototype PMSM and the emulator system, respectively. The emulator can continue operating in closed loop current control in the event of this particular type of driving inverter fault as well. The current reference for the emulation output from the machine model changes appropriately. A close match between the two results again proves the accuracy and the utility of the proposed machine emulator system.

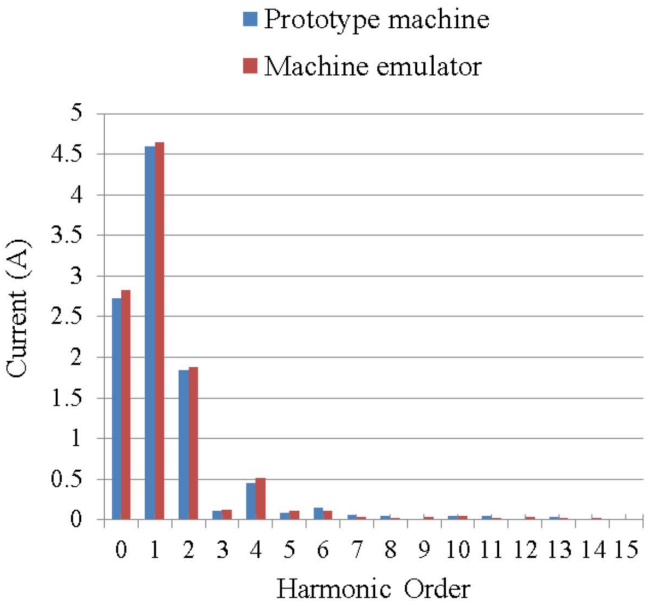

Fig. 4.15: A comparison of the harmonic spectrum for the current drawn by the prototype machine (CH1 of Fig. 4.14(a)) and the machine emulator (CH1 of Fig. 4.14(b)) for an A-phase top switch gate-drive failure fault.

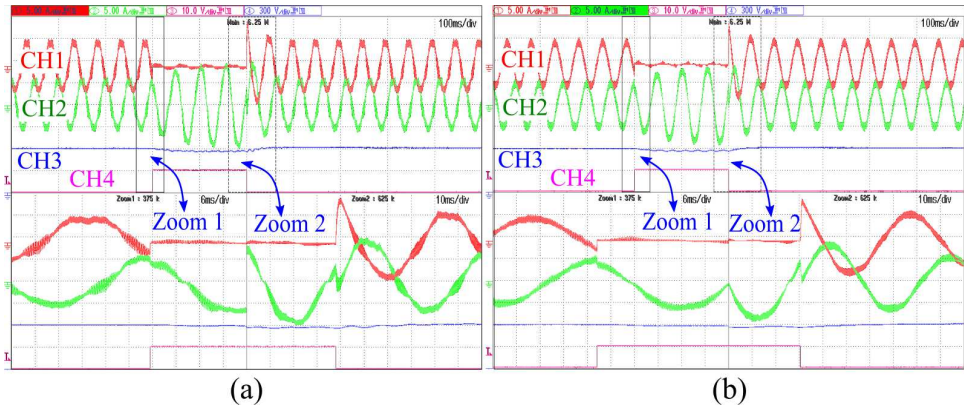

Fig. 4.16: Experimental results obtained for gate drive fault of both switches of A-phase in the driving inverter (a) prototype PMSM being fed by the faulty drive inverter, and (b) emulated PMSM being fed by the faulty drive inverter. CH1: A-phase current (Scale 5 A/div), CH2: B-phase current (Scale 5 A/div), CH3: speed of the PMSM (Scale 300 rpm /div), CH4: fault indication [Time scale: 50 ms/div].

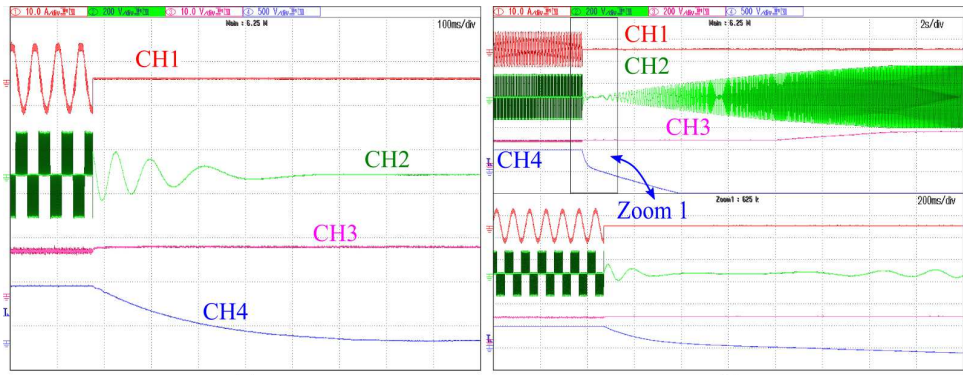

Fig. 4.17: Experimental results obtained for a complete gate unit failure of the driving inverter (a) prototype PMSM being fed by the faulty drive inverter, (b) emulator operating in current control mode (pre and post-fault) and fed by the faulty drive inverter. CH1: A-phase current (Scale 10 A/div), CH2: drive inverter terminal line-line voltage (Scale 200 V/div), CH3: drive inverter DC bus voltage (Scale 200 V/div), CH4: speed of the machine (Scale 500 rpm/div) [Time scale: 100 ms/div and 2 s/div].

Fig. 4.17 and Fig. 4.18 present results for the case of a complete gate-unit failure of the driving inverter. During the event of this type of fault, the machine terminals or the emulated machine terminals are essentially open-circuited. The machine therefore decelerates to zero, post-fault. The terminal voltage measured across the drive inverter terminals would now be the back-emf of the PMSM. This is evident with the results shown in Fig. 4.17(a). In Fig. 4.17(b), current control is sustained for emulator operation post-fault. A sensor non-ideality is artificially included by adding an offset to the sensed currents. The machine emulator is operating in current control mode post-fault, furthermore, post-fault the drive inverter switches are turned off and hence it acts as an open-circuit for the emulator (since its diodes are reverse biased due to its DC bus voltage). Therefore, the sensor offset for current sensing would lead to the PI controller of the emulator integrating this error. This is visible from the sensed drive inverter terminal voltage (shown in CH2 Fig. 4.17(b)), which starts rising post-fault. This voltage keeps rising, until the diodes of the driving inverter are forward biased. This would mean an increase in the DC bus voltage of the driving inverter (shown in CH3 of Fig. 4.17(b)). Such a situation might potentially damage the driving inverter and must therefore be avoided. Furthermore, the speed of the emulated machine increasing in the opposite direction (CH4 of Fig. 4.17(b)) clearly shows that the emulated machine is not operating at the same state as the prototype machine post fault. This clearly shows that current control for the emulator operation

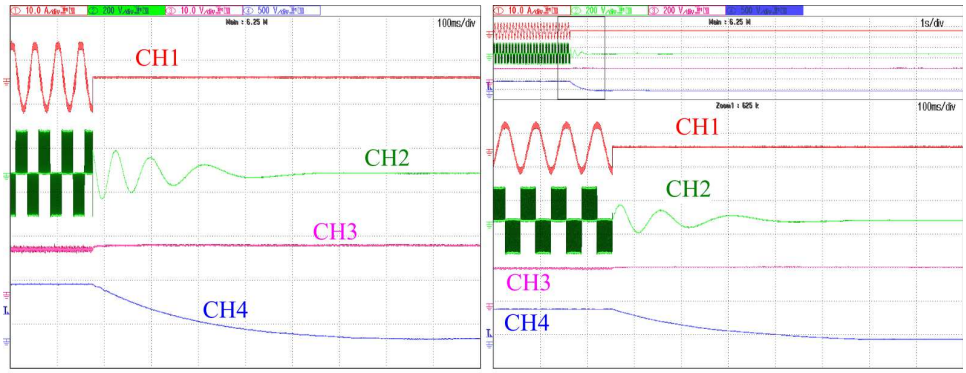

Fig. 4.18: Experimental results obtained for a complete gate unit failure of the driving inverter (a) prototype PMSM being fed by the faulty drive inverter, (b) emulator operating in current control mode pre-fault, and switching over to voltage mode post fault after successful fault detection of the faulty driving inverter. CH1: A-phase current (Scale 10 A/div), CH2: drive inverter terminal line-line voltage (Scale 200 V/div), CH3: drive inverter DC bus voltage (Scale 200 V/div), CH4: speed of the machine (Scale 500 rpm/div) [Time scale: 100 ms/div and 1 s/div].

cannot be maintained post fault for a complete gate-unit failure of the driving inverter.

In Fig. 4.18(b), the emulator control strategy is modified to that as discussed earlier in Fig. 4.12. The fault detection algorithm discussed in Fig. 4.11 is used to change the emulator control strategy from current control mode to voltage control mode post fault-detection. As discussed earlier in this chapter, the fault detection solely detects the fault based on the sensed currents and the rate of change of machine speed alone. The control mode change over ensures that the DC bus voltage of the drive inverter does not charge from the emulator end (CH3 of Fig. 4.18(b)), thus protecting the drive inverter. Furthermore, the drive inverter terminal voltage and the emulated speed of the machine (both shown in Fig. 4.18(b)), have a close match with the results obtained from the prototype PMSM shown in Fig. 4.18(a). The protection algorithm and the control mode changeover would work for other open-circuit based faults as well, such as the opening of a circuit breaker connecting the drive inverter and the machine emulator.

4.5 Summary

This chapter investigated emulation of PMSM drive inverter faults. Of the many drive inverter faults that are possible, open-circuit by means of gate-drive failure was chosen

since they are quite common and stress the current control of the emulator significantly. The chapter initially begins with using closed loop current control, with the control structure presented in Chapter 3. Modifications are then proposed for the current control structure to ensure that lower order harmonics drawn by the emulator during the fault are also emulated accurately. This chapter also presents means to identify certain types of driving inverter faults which necessitate a control mode change from current mode to voltage mode for the emulator. The main conclusions of this chapter are detailed below as follows:

A. Current control with a simple PI controller ensures zero steady state error for DC alone. It was shown in this chapter that the current drawn during gate-drive failure of drive inverters have several lower order harmonic currents. To be able to emulate these lower order harmonics with a zero steady state error, this chapter combined resonant controllers at different harmonics along with the PI controller. The machine speed was measured and used as an input for the resonant controllers making its resonant frequencies adaptable to the speed of the machine. The modified current control for the emulator thus ensured accurate emulation for all transient conditions of the drive inverter operation.

B. In the event of complete gate-unit failure, it was seen that sustaining current control for the emulator can possibly damage the driving inverter. Thus a fault detection algorithm based solely on the measured emulated currents and the machine speed was initially developed. This algorithm was used to switch the control mode of the emulator from current control mode to voltage control mode upon fault detection. Transferring this control mode was able to ensure a safe and accurate emulation for the machine turn-off during this particular fault case as well.

C. Multiple experimental results for various machine transient conditions were presented in this chapter. A close match between the results obtained from the emulated machine and the prototype machine, proves the capability of the improved controller, the bandwidth sufficiency of the emulator and the benefit of using detailed look-up table based machine FEA models for the purpose of emulation. For the case of the fault with a complete gate-unit failure, experimental results are also presented for fault identification and transfer from current mode to voltage mode. A good match between the results obtained from

the prototype machine and that from the emulated machine are shown for this case as well.

Chapter 5

Open-winding PM machine: control and emulation

The earlier chapters discussed the various aspects of emulation of a star-connected (or delta-connected) PMSM. In such a machine at a time only two phases can be independently controlled. The current in the third phase is automatically equal to the negative sum of the first two phase currents. A standard two-level is used as a drive inverter for such a PMSM. Various aspects of emulation were discussed including the control strategy for emulation, modifications of the control strategy to improve bandwidth, the importance of a detailed look-up table based model for the purpose of emulation and modification for the emulation control strategy in the event of driving inverter faults.

This chapter looks into the control and emulation of open-winding PM machines. In open-winding PM machines, the three phases of the machine are independently controlled, allowing a wider speed range of operation. This makes open-winding PM motors particularly suitable for transportation applications [45, 46, 48]. There has therefore been a lot work on the control and modeling of open-winding PM machines [1, 45, 46, 48, 67]. This chapter proposes a control methodology to control the three phase currents of an open-winding PM machine independently. This control strategy consists of PI and PR controllers working in tandem, and will be discussed in detail in the chapter.

In several cases, advanced controllers are used to generate current reference in order to achieve additional control objectives for an open-winding machine based drive, such as torque-ripple minimization [45–48]. The proposed control methodology presented in this chapter will also be used to implement a torque ripple minimization

strategy presented in [48] and [47]. This will help prove the utility of the proposed current control.

Finally, this chapter will address the thesis objective of machine emulation by emulating an open winding machine as well. There is no reported literature related to the emulation of an open-winding machine and hence the work presented in the chapter towards the emulation of such a machine will be an important contribution in this area. The emulation of such a machine would require modifications to the drive inverter power converter structure and the machine emulator power converter structure. The same proposed current controller will also be used to control the open-winding machine emulator system. Design of the emulator control will also be discussed in this chapter.

5.1 Independent phase current control for the open-winding PM drive

This section presents the system description and the proposed current control for the independent phase current control of an open-winding machine. The implementation of a higher-level torque ripple minimization algorithm existing in literature [47, 48], to verify the driving inverter current controller will also be presented in this section.

5.1.1 System description

An open-winding PM machine has all six terminals of its three phases accessible. This allows the possibility to control the three winding currents of the machine independently. To control such a machine a simple two-level converter will not suffice. Several works have been published on the topologies of open-winding PM machines and its control [3, 46, 46–48]. This chapter will however look into a simple driving inverter topology to drive the emulated open-winding PM machine. Single-phase full-bridge converters fed by separate isolated DC power supplies, are used to energize each winding of the open-winding machine. The system diagram for the driving inverter feeding the open-winding PM motor is shown in Fig. 5.1. Since the three full-bridge converters are fed with three separate DC power supplies common mode currents introduced due to PWM switching of the driving inverter topology do not exist. The proposed current controller generates gating signals for the driving inverter such that the open-winding machine draws the three independent currents as required.

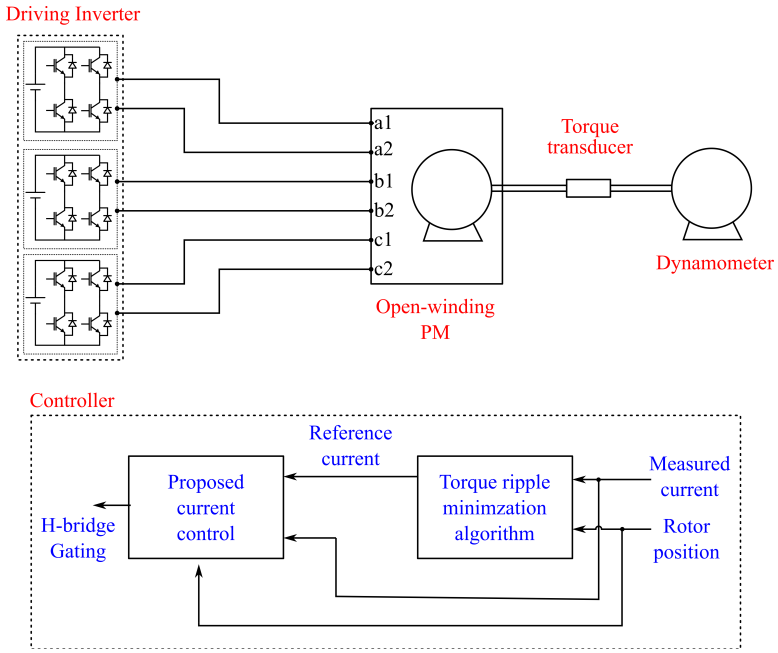

Fig. 5.1: System diagram of three single-phase full bridge converters feeding the open-winding PM machine

The proposed current control can receive a constant current reference corresponding to the torque required. The measured phase back-emf of the PM machine is shown in Fig. 5.2. The machine back-emf shows several harmonics, the most significant being the third harmonic. In an open-winding machine there is no natural cancellation of the third harmonic current. In addition, the phase back-emf also shows 5^{th} and 7^{th} harmonics which results in corresponding harmonic currents in the machine as well. The resulting harmonic currents, if uncontrolled, are only limited by the machine leakage, and can therefore be quite high, especially the lower order harmonics like the third, 5^{th} and 7^{th}. These high harmonic currents can cause overheating of the machine and are hence need to be suppressed.

The system diagram also shows the possibility to include a higher-level controller for torque-ripple minimization, for generating reference to the proposed current controller. This chapter implements the torque ripple minimization algorithm discussed in [45–48]. This algorithm, based on the machine back-emf generates current references for the machine winding excitation to minimize torque ripple. The current reference could thus have several lower order harmonics. The proposed current control should therefore be capable of controlling each of these harmonic order currents at a specified value as well.

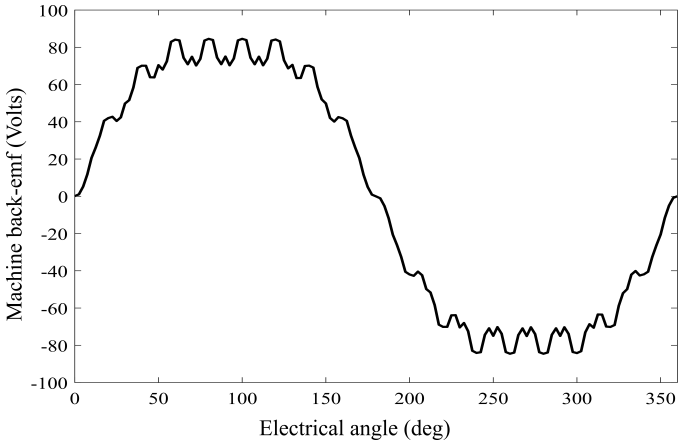

Fig. 5.2: Machine back-EMF waveform, obtained experimentally, showing the third harmonic and other spatial harmonics

5.1.2 Proposed current controller

The current controller proposed to address the requirement of independent phase current control of an open-winding machine is presented in Fig. 5.3(a). The proposed controller similar to the works proposed in [68, 69] selectively controls the current harmonic components of interest.

In the *dq* axis, the proposed controller consists of a PI and a 6^{th} harmonic resonant controller. 5^{th} and 7^{th} harmonic currents in the *abc* frame are converted to 6^{th} harmonic in the *dq* frame. Hence, one 6^{th} harmonic resonant controller suppresses (or controls) both, the 5^{th} and the 7^{th} harmonic currents in the *abc* frame. For the zero-sequence axes, the proposed controller consists of a PI controller, a resonant controller for the fundamental frequency and a resonant controller for the 3^{rd} harmonic. The flat-top waveshape of the back-emf as shown in Fig. 5.2 earlier, introduces 3^{rd} harmonics which can be suppressed by the third harmonic resonant controller. A PI controller in addition is required to suppress any zero sequence DC current due to unbalances or sensor offsets in the three phases. In addition, a fundamental resonant controller is required as part of the zero sequence controller when the open-winding machine is to operate under unbalanced conditions, or at conditions when only two windings are to be excited. Thus the proposed current controller ensures that the harmonics in the currents drawn by the open-winding machine are controlled or suppressed as required. The resonant controller implementation is shown in Fig. 5.3(b). Since the machine is a synchronous machine, the measured speed of the machine can be easily used to calculate the resonant frequency of the various resonant controllers. Thus,

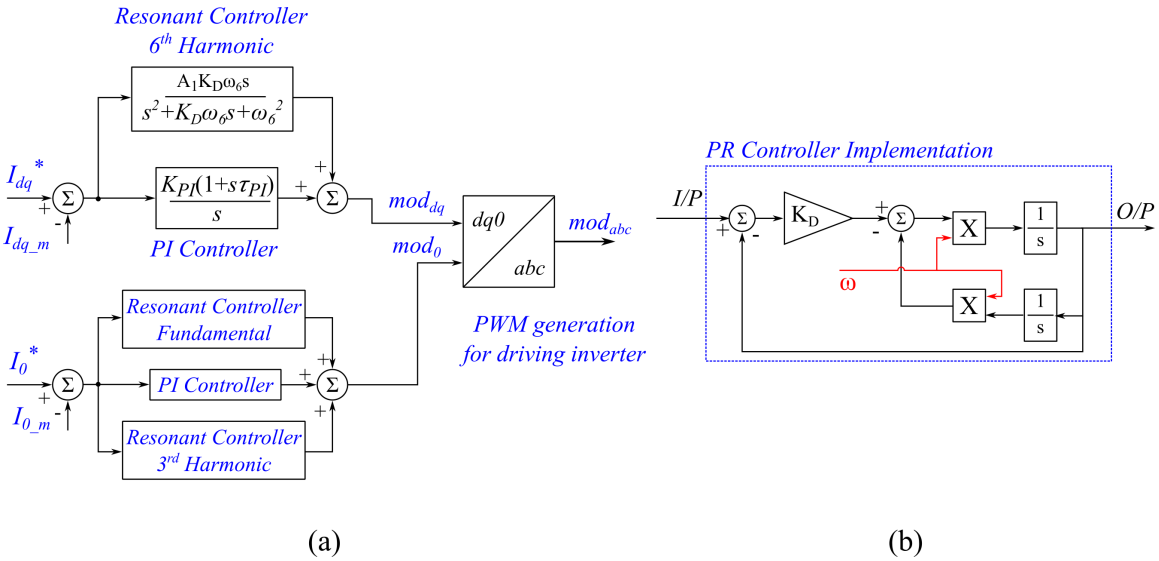

Fig. 5.3: (a)Proposed current controller for the open-winding PM machine drive inverter (b) Resonant controller implementation

the resonant frequency of the controllers can be changed based on the dynamically changing speed of the open-winding machine.

The proposed current controller is designed for a current control bandwidth of 400 Hz for the dq-axis and the *zero*-axis. The magnitude and the phase plots when only PI controllers are used and when the proposed controller is used are both shown in Fi. 5.4. It can be seen that the PI controller when used alone has a poor open loop gain for the frequencies of interest, viz., the 6^{th} harmonic for the dq-axis, and the fundamental and 3^{rd} harmonic for the *zero*-axis. This would mean that there would be a poor accuracy as well to control the corresponding harmonic components of the currents as well. When the proposed controller is used, the open-loop gain at the frequencies of interest is increased by at least 20 dB. This would mean that there would be a higher accuracy to control the corresponding harmonic components of interest in the machine winding currents. Experimental results are presented in Section 5.4.

5.2 Emulation of an open-winding PM machine

Emulation of the open-winding machine would require that the three machine windings be emulated independently. Therefore the machine emulator structure discussed in Chapter 2-Chapter 4 cannot be used as it is. To preserve the high emulation bandwidth

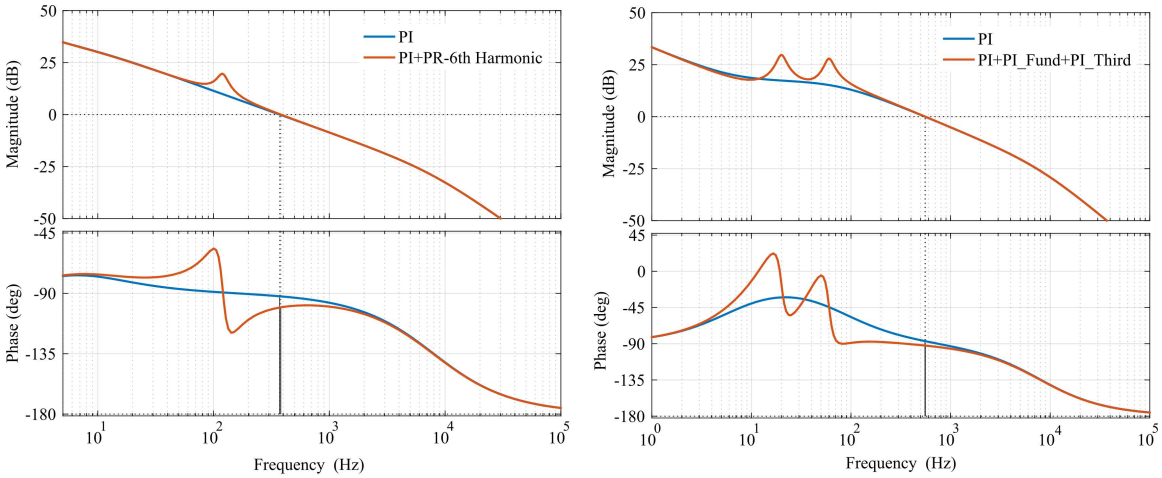

Fig. 5.4: (a) Magnitude and phase plots of simple PI controller and the proposed current controller in the *dq*-axis, (b) Magnitude and phase plots of a simple PI controller and the proposed current controller in the *zero*-axis.

achieved in Chapter 3 and Chapter 4, the emulator system presented for open-winding machine also uses linear amplifiers as power amplifiers. The linear amplifiers have to however be connected in a manner such that each linear amplifier emulates each winding of the machine independently. Therefore, each full bridge converter is connected via a coupling inductance to the linear amplifier emulating the corresponding winding of the machine. A system diagram describing the same is illustrated in Fig. 5.5(b).

The drive inverter control was discussed earlier, but is shown again in Fig. 5.5(a). The emulator control is shown in Fig. 5.5(d). Though both controllers are implemented on the same RTS, there is no communication between the two controllers. The discussions involving the bandwidth criterion for the driving inverter and the emulator both operating in current control mode, discussed in Chapter 2 and Chapter 3, holds good for this system as well. It is necessary to ensure that the emulator current control bandwidth is at least five times faster than the current control bandwidth of the driving inverter.

The machine model used in Chapter 2-Chapter 4 is for a star-connected machine alone, and therefore does not allow an independent phase current control of the three machine winding currents. Since the machine emulated in this chapter is an open-winding PM machine, for the emulator control used in Fig. 5.5(d), a *dq0* model of the machine as presented in (19)-(23), needs to be used.

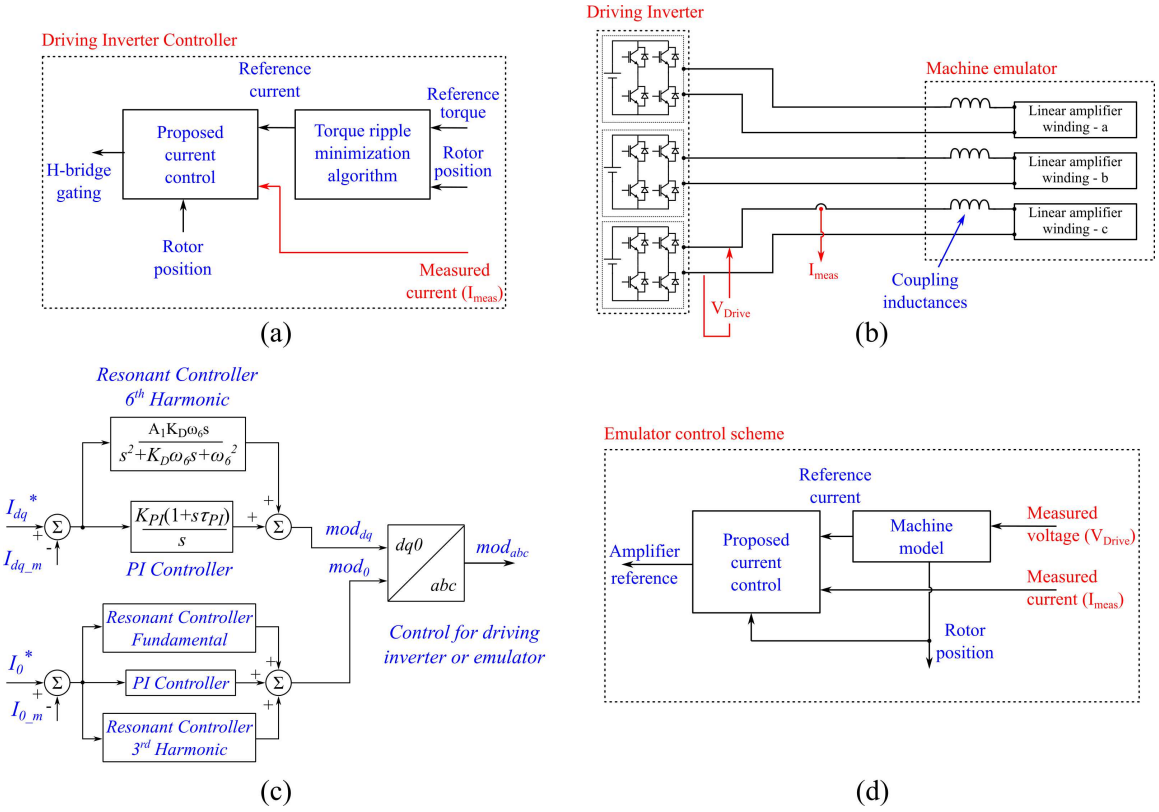

Fig. 5.5: (a) Control structure for the driving inverter, (b) System diagram of the proposed machine emulator, (c) proposed current controller for the machine emulator, (d) Control structure for the emulator

$$v_d = R_s\, i_d - \omega\lambda_q + L_d \frac{di_d}{dt} \tag{19}$$

$$v_q = R_s\, i_q + \omega\lambda_d + L_q \frac{di_q}{dt} \tag{20}$$

$$v_0 = R_s\, i_0 + L_0\, \frac{di_0}{dt} \tag{21}$$

$$\lambda_d = L_d\, i_d + \lambda_{af} \tag{22}$$

$$\lambda_q = L_q\, i_q \tag{23}$$

where, v_d, v_q and v_0 are the direct axis, quadrature axis and the zero axis voltages respectively, ω is the electrical speed of the rotor, L_d, L_q and L_0 are the d, q and 0 axis inductances respectively, λ_d and λ_q are direct and quadrature axis flux linkages respectively, λ_{af} is the magnet flux linkage, and L_d, L_q and L_0 are the direct axis, quadrature axis and the zero axis inductances respectively. Such models have been

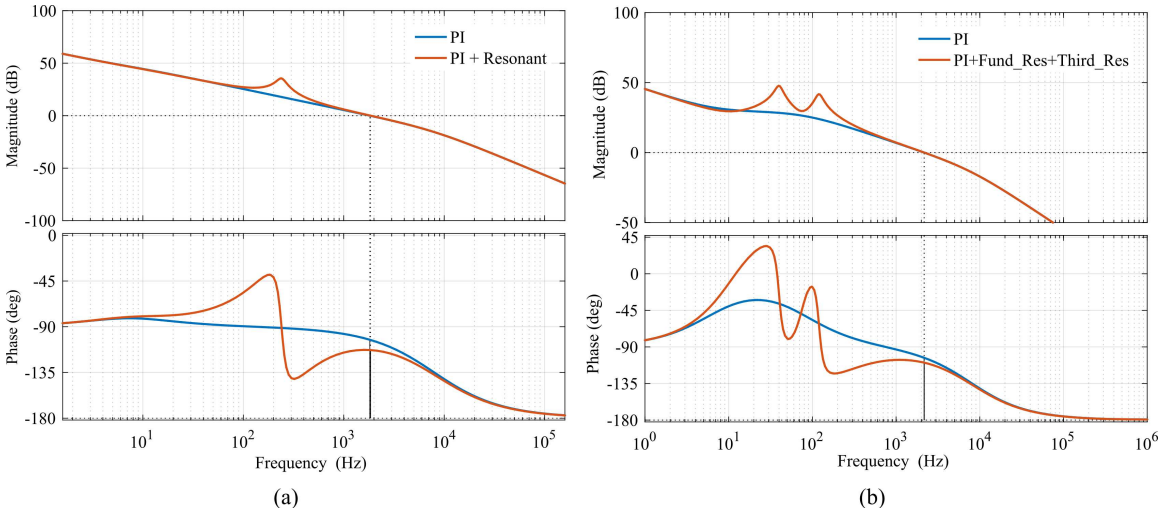

Fig. 5.6: (a) Magnitude and phase plots of the open loop transfer function for the *dq*-axis current control loop of the machine emulator (b) Magnitude and phase plots of the open loop transfer function for the *zero*-sequence current control loop of the machine emulator

discussed in adequate detail in literature [70] and is not repeated here.

A similar current controller, as that used for the driving inverter, is used for the emulator as well Fig. 5.3(c). The only difference being that the current control bandwidth of the emulator is five times higher than the current control bandwidth of the driving inverter. Since the current control bandwidth of the driving inverter was designed to be 400 Hz, the current control bandwidth of the emulator is designed at 2000 Hz. The magnitude and the phase plots for the emulator current control loop are shown in Fig. 5.6. It can be seen that the *dq*-axis controller and the *zero-sequence* controller are both designed for a bandwidth of 2 kHz.

The magnitude and the phase plots also show resonant controller action at the frequencies of interest. In a similar manner as the drive inverter controller, the presence of the resonant controllers in the emulator control loop again ensures control or suppression of the harmonic components of interest in the emulated currents. Furthermore, the PI controller action alone is also superimposed in the same magnitude and phase plots of the proposed emulator current controller in Fig. 5.6. This shows a higher open loop gain and thus a lower steady state error at the frequencies of interest when the proposed current controller is used.

5.3 Experimental setup

The experimental setup for the open-winding machine emulator system is shown in Fig. 5.7. Three linear amplifiers [54] are used, each emulating one phase of the open-winding PM machine. The driving inverter is built using IGBT Switches SKM75GB-12V.The driving inverter is composed of three full-bridge converters. Each full bridge converter of the driving inverter drives one emulated winding of the machine. The DC bus of each of the full-bridge converters is supplied by a diode bridge rectifier connected to an isolation transformer. These isolation transformers are also shown in the figure. Coupling inductances are used to interconnect the driving inverter and the emulator. The value of these coupling inductors chosen is 3 mH, which is close to the machine inductance. The driving inverter control and the machine emulator control are both implemented on the same RTS also shown in the same figure. A protection circuit in addition is used to protect the system in the event of an over current or an over-voltage fault.

The same driving inverter topology along with the same control is used to drive a prototype open-winding PM machine as well. The results obtained from the prototype machine and the emulated machine are compared to prove the validity and the utility of the developed emulator system.

5.4 Experimental results

The experimental results obtained from the drive and that obtained from the emulator setup are both presented in this section. Initially an investigation is done to prove the effectiveness of the proposed current controller when feeding an open-winding PM motor. Dynamic performance of such resonant controllers is often under scrutiny. The resonant controller is designed to adaptively change its resonant frequencies based on the measured rotor speed. To investigate the dynamic performance of the proposed controller, the current drawn by the machine when a dq-axis PI current controller alone is used, is compared with when the proposed current controller is used. The PI controller bandwidth for both cases are kept fixed at 400 Hz. In the proposed current controller, additional resonant controllers are used for the 6^{th} harmonic in the dq-axes, and fundamental and the 3^{rd} harmonic in the zero-sequence controller. The experimental results obtained for both cases are shown in Fig. 5.8. It is clear that when the proposed current control is not used, the current drawn by the machine is

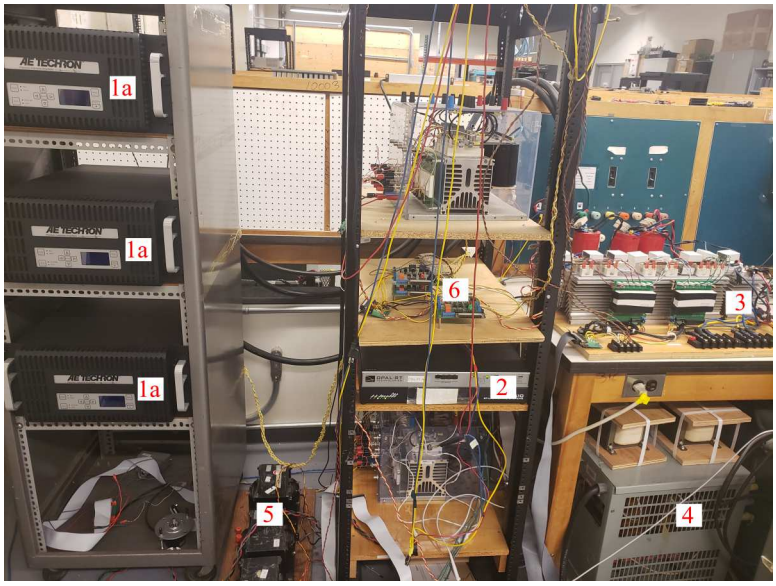

Fig. 5.7: Experimental setup of the open-winding machine emulator (1) Linear amplifiers emulating machine behavior, (2) RTS controlling emulator and drive inverter, (3) drive inverter, (4) isolation transformers to supply DC buses of the driving inverter, (5) inductors connecting the driving inverter and the emulator, (6) protection circuitry

rich in lower order harmonics. However, when the proposed current controller is used, the additional resonant controllers ensure that the current drawn is more sinusoidal, i.e., the lower order harmonics are suppressed. Fig. 5.8(b) also shows the dynamic performance of the proposed current controller. It can be seen that the current drawn by the machine is sinusoidal (i.e. devoid of lower order harmonics) throughout the duration of machine start-up. Zoomed windows of machine current at low speed and at high speed are also shown in Fig. 5.8(b), and it can be seen that the current drawn by the machine is sinusoidal in both cases, thus proving the dynamic adaptability of the proposed current controller.

The harmonic spectrum of the current drawn by the machine in both cases, i.e., when a *dq* PI controller alone is used, against when the proposed current controller is used is shown in Fig. 5.9. It can be seen that with the help of the proposed current controller, the DC component, the 3^{rd} harmonic and the 5^{th} harmonic are suppressed. The harmonic spectrum is shown at a particular frequency of operation of the machine, however with the implementation of the resonant controllers as presented in this chapter, it would be possible to obtain a similar harmonic spectrum at all frequencies of operation.

The proposed current controller can also be used for machine operation under

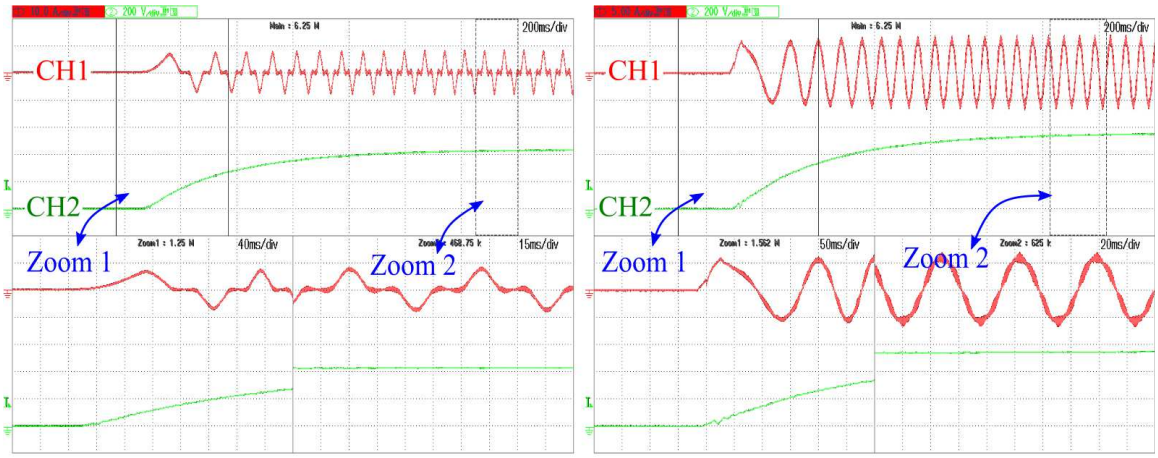

(a) (b)

Fig. 5.8: Start-up of the machine when operating in torque control mode (a)Current drawn by the machine when only a simple dq PI controller is used (b) Current drawn by the machine when the proposed current controller is used; CH1: Current drawn by the machine (Scale: 10 A/div), CH2: Speed of the machine (Scale: 250 rpm/div) [Time Scale: 200 ms/div]

conditions when only two of the machine windings are supplied. With only two machine windings excited, the current in the zero-sequence circuit would be at the fundamental frequency. The resonant controller tuned at the fundamental frequency in the zero sequence controller (see Figure 5.3) can help controlling/ suppressing this current harmonic. The results obtained for this operating condition of the drive are shown in Fig. 5.10(a). It can be seen that the currents are sinusoidal (i.e., devoid of lower order harmonics).

A large torque ripple is expected when only two windings of the machine are energized. The machine is operating in current control mode (torque control mode) with a constant value of current (torque). Under this control mode, the resulting torque ripple would be visible as speed ripple. A zoomed version of the speed ripple is also shown in Fig. 5.10(a). As can be seen, there is a speed ripple of close to 20 rpm/div. The mechanical time constant of the machine filters out the speed ripple to a large extent, but the presence of this speed ripple indirectly means that there is a large torque ripple in the drive.

As mentioned earlier, the proposed current control can also be used in instances when the reference current for the proposed current controller is the output of a torque ripple minimization algorithm. The algorithm discussed in [47,48] is implemented as it is. This algorithm generates current reference for the proposed current controller. The

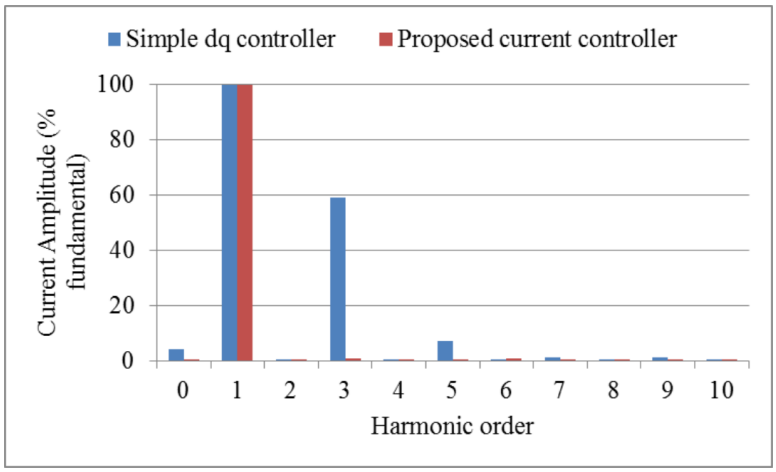

Fig. 5.9: Harmonic spectrum of the current drawn by the machine when the proposed current control is used compared with a dq-axis PI controller.

results obtained are shown in Fig. 5.10(b).The currents drawn by the two windings of the machine are non-sinusoidal, since the reference currents output by the torque ripple minimization requires the same. The speed ripple in this case however is significantly reduced. This proves the versatility of the proposed current controller to not only suppress the current harmonics of interest to zero, but also control them at the required values as dictated by a higher-level control objective such as with the torque-ripple minimization algorithm.

The emulator system is next driven by the same driving inverter and its control. The proposed current controller is used for the current control of the machine emulator and the drive inverter. However as discussed in Section 5.2, the emulator current control loop bandwidth is five times higher than the current control bandwidth of the drive inverter. Results obtained for the emulation of an open-winding machine when only two phases are energized are shown in Fig. 5.11. The currents drawn by the emulated machine windings with constant current excitation is shown in Fig. 5.11(a). It can be seen that the currents are sinusoidal and match closely to the results obtained when the same driving inverter feeds the prototype open-winding machine (Fig. 5.10(a)). The speed ripple which is similar to the case of the prototype machine case is also evident in this result. To further evaluate the capability of the emulator system, the torque ripple minimization algorithm generates a current reference for the drive inverter control. The drive inverter in this case is again driving the emulated machine. There is again a good match of results between the emulated machine (Fig. 5.10(b)) and case when the sae driving inverter feeds a prototype machine

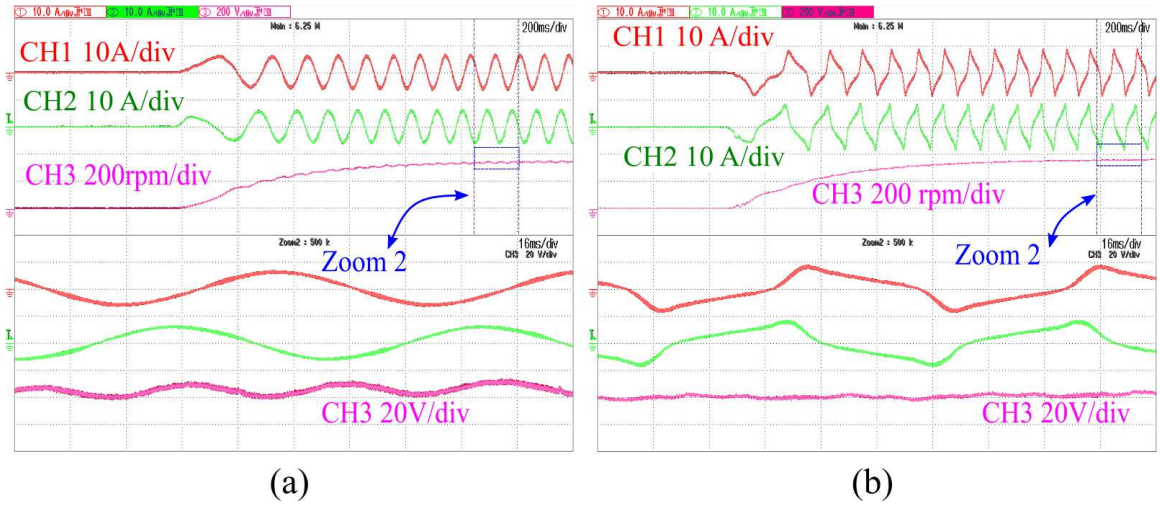

Fig. 5.10: Machine operation with only two winding excitation (a) Current drawn by the machine when a constant current reference is given to the proposed current controller (b) Current drawn by the machine when the current reference to the proposed current controller is output of the torque ripple minimization algorithm

(Fig. 5.11(b)). The reduction of speed ripple is also evident in this case.

A good match between the results obtained from the prototype open-winding machine (Fig. 5.10) and the emulator system Fig. 5.11 proves the utility and the accuracy of the emulator system to emulate open-winding machine behavior. The emulator system allows the possibility to study a wide variety of drive inverter control schemes and algorithms. For instance, with the torque ripple minimization algorithm implemented in this chapter, optimizations can be done based on the emulated machine parameters and geometry without a need for physical changes to the actual prototype machine.

5.5 Summary

In an open-winding machine there is no natural cancellation of the third harmonic current. In addition, the phase back-emf also contains other lower order harmonics like the 5^{th} and 7^{th}, which results in corresponding harmonic currents in the machine. This chapter proposed a current controller to control or suppress the current harmonic components of interest. An emulator setup to allow emulation of open-winding machines was also presented in this chapter. Experimental results were presented to validate the emulator setup and the proposed current controller used for the emulator and the driving inverter. The main summarizing comments of this chapter are as

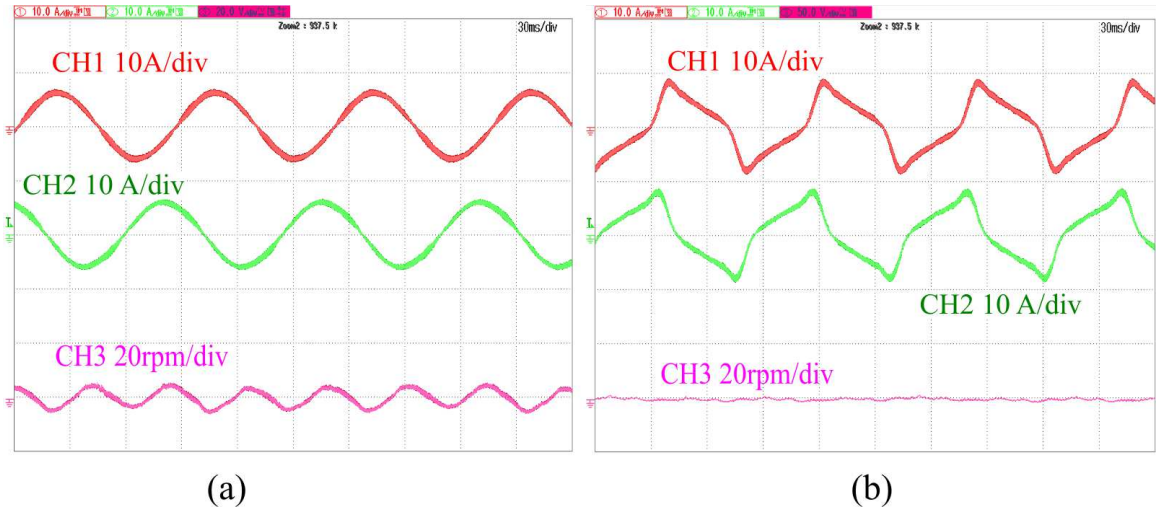

Fig. 5.11: Machine emulation with only two winding excitation (a) Current drawn by the machine when a constant current reference is given to the proposed current controller (b) Current drawn by the machine when the current reference to the proposed current controller is output of the torque ripple minimization algorithm

follows:

A. The current controller proposed in this chapter consisted of PI and resonant controllers, both in the *dq*-frame and the *zero-sequence* frame. This allows control or suppression of the individual harmonic components of interest. The proposed current control was used on a full-bridge converter based inverter driving an open-winding PM machine.

B. An emulator setup was developed using three linear amplifiers emulating each phase of the open-wining PM machine. The same proposed current control was used for the emulator control as well. However the emulator current control, designed at a bandwidth of 2 kHz, is five times faster that the current control bandwidth of the driving inverter, designed at 400 Hz. This ensures stable emulation.

C. Experimental results are presented for the emulator operation. Results obtained from the emulator are compared with the results obtained when the driving inverter feeds a prototype machine. A good match between the two results proves the accuracy of the developed emulator system. To further prove the utility of the proposed emulator system, experimental results are also presented for the case when a torque ripple minimization algorithm available in literature

generates reference currents for the driving inverter current control.

Chapter 6

PM generator emulation and hybrid power amplifier design

This chapter presents works done with respect to emulation in collaboration with other students of the power electronics and energy research (PEER) group, at Concordia. The works discussed in this chapter are;

- Emulation of a permanent magnet synchronous generator
- Hybrid linear-switched power amplifier and control strategy

The primarily involvement of the author of this thesis in both these areas were on the experimental setup development. Other implementation aspects such as control implementation which were contributions of the author, will also be presented in this chapter.

6.1 Emulation of a permanent magnet synchronous generator in real-time using power hardware-in-the-loop

Permanent magnet synchronous generators (PMSGs) are gaining popularity in the field of hybrid/ electric traction vehicle electrification, due to several advantages such as high power density and high efficiency [71–80]. In hybrid electric vehicles, both on-road and off-road, a PMSG is used as part of the on-board range-extender [73–76]. In such a system, the PMSG is coupled to an internal combustion engine so as to

power the vehicle battery and associated auxiliary units [73–76]. In larger traction systems such as a ship-propulsion systems or electric-aircrafts, a PMSG is used as part of the mobile power system to supply power to various sub-systems within the vehicle [77–80]. A lot of work has also been done pertaining to power generation from renewable energy sources using PMSGs [27, 28, 81], which could be of considerable importance for traction electrification as well. Hence analysis and design of PMSGs is important for traction electrification.

With respect to analyzing PMSG models, the primary focus in existing literature is on the steady-state operational aspects of the PMSG with the characteristics of the mechanical and the prime mover system such as micro-hydro power plants and wind power plants [23, 28, 80, 81]. The work presented in this chapter on the other hand, focuses on transients and non-linear load performance of the generator from the machine model perspective. Furthermore, this work also suggests a method to convert the permanent magnet machine-model which is voltage-fed, current-out model into a torque-fed, voltage-out model to allow for the generator emulation for isolated loads. This is accomplished by adding a compliance element to the real-time PMSG model. The developed model is used for power-hardware simulation of a PMSG in this chapter.

6.1.1 PMSG modeling and the requirement of a compliance element

A three phase permanent magnet synchronous motor with symmetrically distributed stator windings has been modeled in the synchronous reference frame. The validity of the model is presented in several papers [82, 83]. The mathematical equations that describe the model are presented below in this section for reference.

$$v_d = -R_s\, i_d - \omega\lambda_q - L_d\frac{di_d}{dt} \tag{24}$$

$$v_q = -R_s\, i_q + \omega\lambda_d - L_q\frac{di_q}{dt} \tag{25}$$

$$\lambda_d = -L_d\, i_d + \lambda_{af} \tag{26}$$

$$\lambda_q = -L_q\, i_q \tag{27}$$

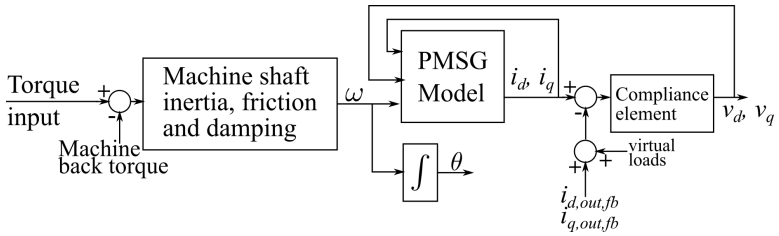

Fig. 6.1: Overall structure of the PMSG model driven by a torque source. In the PHIL emulator, the model is fed back with sensed currents $i_{d,out,fb}$ and $i_{q,out,fb}$ from the physical load.

where, v_d and v_q are the direct and quadrature axis voltages respectively, ω is the electrical speed of the rotor, L_d and L_q are the d and q axis inductances respectively, λ_d and λ_q are direct and quadrature axis flux linkages respectively, λ_{af} is the magnet flux linkage. The inductances L_d and L_q are obtained from the magnetizing inductance L_m and the leakage inductances as shown below from the equivalent circuit (Fig. 6.2).

$$L_d = L_{md} + L_{ls} \tag{28}$$

$$L_q = L_{mq} + L_{ls} \tag{29}$$

In the proposed system, the PMSG with P number of poles is driven by a torque source such as a current controlled DC motor which is the prime mover of the generator. The electro-magnetic torque generated by the machine (back-torque) is given below.

$$T = 1.5\frac{P}{2}\left[\lambda_d\, i_q + (L_d - L_q)\, i_d\, i_q\right] \tag{30}$$

The PMSG rotor is accelerated by the difference of the driving torque and the electro-magnetic torque (T) generated by the PMSG (back-torque). This torque difference is the input to the mechanical sub-system of the model as shown in Fig. 6.1. The mechanical system is modeled by the following equation.

$$T_{\text{in}} - T = J\frac{d}{dt}\omega + B\omega \tag{31}$$

where, J is the rotational inertial of the shaft, B is the viscous friction on the shaft. The rotor position θ is obtained by integrating the speed of the machine ω.

Fig. 6.2 shows the equivalent circuit of a PMSG in the synchronous reference frame that is used by the real-time model. The standard machine model represented by equations (24) to (27); the input of such a system is the terminal voltages (v_d

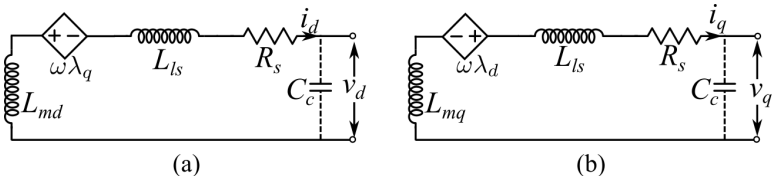

Fig. 6.2: Equivalent circuit of a permanent magnet synchronous generator in synchronous reference frame; (a) d-axis equivalent circuit; (b) q-axis equivalent circuit.

and v_q referenced to d and q axes respectively), and the output of the model is the motor line currents, the torque and the mechanical speed. This model is known as the voltage-fed, current-out model. On the other hand, the inputs to the generator is the torque and the output is the terminal voltages; which is torque-fed, voltage-out model. The terminal voltage of the machine is determined by the load currents, and load currents are in turn determined by the terminal voltage. This causes a causality violation in the system model.

The capacitor C_c is a compliance element added in the model to ensure integral causality for the real-time discrete time simulation, required for implementation on real-time solvers. As seen from equations (24) to (27), the output voltage of the generator has a differential causality without the compliance capacitance [84, 85]. The equations (24) to (27) solve for the line currents when the terminal voltages are known. In this case, for the PHIL emulation the proposed emulator terminals should replicate the machine terminal voltages; the line currents will be determined by the actual physical load characteristics. These real currents are sensed and fed back to the machine model to evaluate the terminal voltages. Without the use of the compliance capacitor C_c it is not possible to obtain the terminal voltage of the generator using a real-time model.

In physical terms, the compliance capacitance includes the inter-winding capacitance, capacitance to the frame/ground, and the capacitance from the measuring elements such as probes and many other parasitic capacitances. In the model, for the real-time simulation purposes, this capacitance C_c holds the initial value of the terminal voltage (v_d and v_q). Similarly, the initial conditions for the currents i_d and i_q are given as the initial values of the currents through the inductances L_d and L_q respectively. Without the added compliance element, it is not possible to specify the initial conditions (v_d and v_q) of the system. The compliance element enables the dynamic variables (states) of the system to exist. This initial value of v_d and v_q is required to solve for the currents i_d and i_q for the time $t = 0^+$ onwards in real-time.

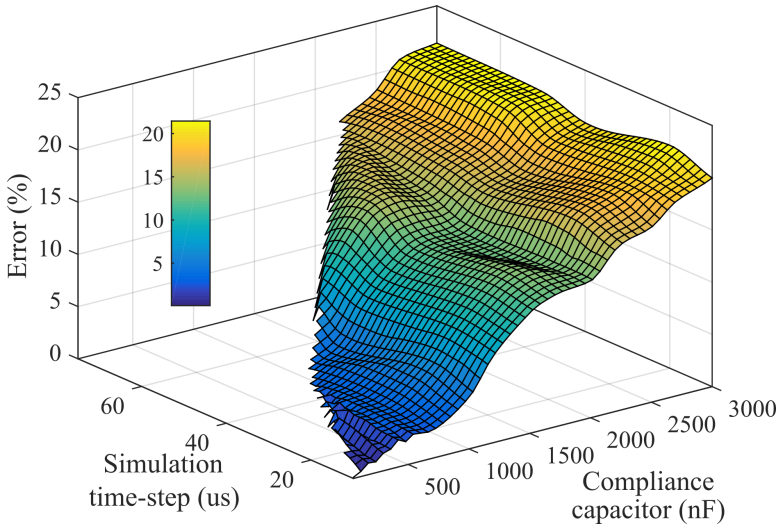

Fig. 6.3: Error for step change in the PMSG response for compliance capacitance and simulation time step variation.

6.1.2 Accuracy analysis with compliance element variation

Paper [29], also co-authored by the author of this thesis, presents a detailed analysis of the compliance element impact. One of these impacts is the error in the model accuracy. To analyze this, the effect of the compliance capacitance on the accuracy of the real-time simulation for a given time step T_S, a real-time simulation is performed for the proposed PMSG model feeding a switched resistive load. The transient current waveforms are obtained and compared with the results from offline simulation, which does not have a simulation time-step limitation. For the comparison presented in this section, the offline simulation runs at a 1μs time step with a compliance capacitance of 1 nF. A three dimensional plot is obtained with the error compared with an offline simulation (Fig. 6.3). Two inferences can be made from the plot: (i) larger values of compliance capacitance leads to larger errors for a given time step in the real-time simulation, and (ii) for larger time-steps of the real-time simulation, a larger value of compliance capacitance is required for ensuring stable real-time simulation, implying a larger error with respect to an offline simulation running at a small time step.

6.1.3 System description of the emulator system for PMSG

The PHIL emulator consists of a real-time processor simulating the model of the PMSG, and a power amplifier that converts the numerical data in the processor (control signals) to physical power handling nodes (Fig. 6.4(a)). The power amplifier used in

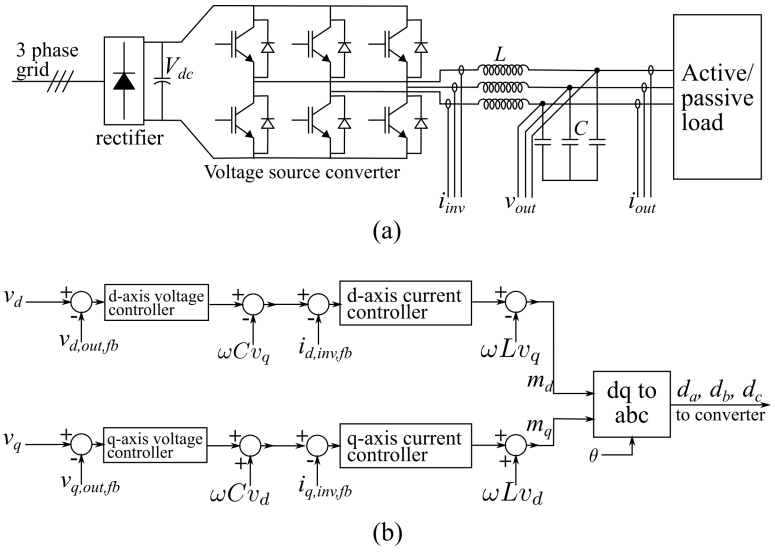

Fig. 6.4: (a) A voltage source inverter operating as a power amplifier; (b) decoupled vector control of the voltage source inverter.

the proposed work is a two-level voltage source inverter (VSI) with a coupling LC filter network. The LC network filters the switching voltages generated due to the pulse width modulation (PWM) at the VSI's terminals. As the inverter supplies power to the load, due to the flow of current, a voltage drop and a phase shift is introduced between the voltage at the inverter terminals and at the output of the system. This voltage drop and phase shift is dependent on the load current which is determined by the load characteristics, and hence cannot be pre-programmed and has to be evaluated in real-time.

The modulation command to the inverter should be appropriately modified in real-time. This is accomplished by the vector control scheme shown in Fig. 6.4(b). The decoupling terms for the vector control scheme ensures good performance during load transients [86]. The control shown in (Fig. 6.4(a)), maintains the output voltage v_{out}, at a desired value. The reference value for v_{out} is defined by the PMSG model described in the earlier section. The overall impedance of the LC network should be smaller when compared to the machine impedance. This will ensure that the presence of the LC filter does not reduce the bandwidth available for the emulation of the PMSG dynamics.

A block diagram of the proposed PHIL emulator with the voltage and current controllers (Fig. 6.4(b)) is shown in Fig. 6.5. The voltage and the current controllers for the vector control scheme can be designed with the aid of this block diagram.

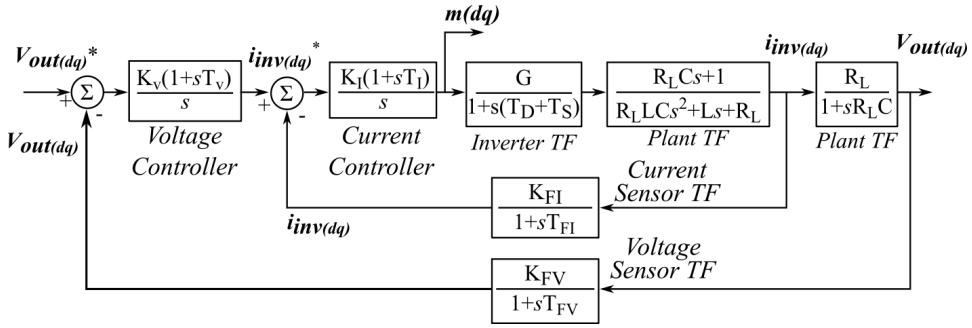

Fig. 6.5: Block diagram of the emulator system with the current and the voltage controllers.

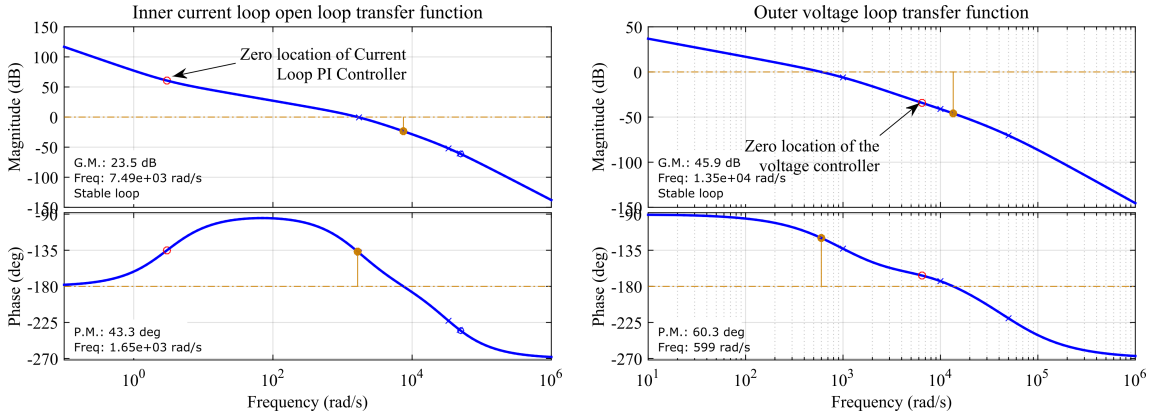

(a) (b)

Fig. 6.6: (a) Magnitude and phase plot for the inner current loop open loop transfer function. (b) Magnitude and phase plots for the outer voltage loop open loop transfer function.

Fig. 6.4(b) contains feed-forward terms for decoupling the control efforts along two orthogonal axes. Since these terms do not affect the controller design, these have been omitted in the block diagram in Fig. 6.5 for simplicity. In the block diagram of the emulator system, the inverter transfer function is characterized by a gain G (representative of the DC link voltage of the VSI) and delays T_D (inverter delay), and T_S (the controller sample time). The plant transfer function contains a load dependent component (R_L). The voltage and current controllers are designed for the rated load of the emulator system. The sensing network for the current and voltage measurement is represented by a simple first order transfer functions with a time constant of T_{FI} and T_{FV}, respectively. Simple proportional-integral (PI) type controllers are used for both the voltage and the current loops of the system. Magnitude and phase plots of the inner current loop and the outer loops are shown in Fig. 6.6a and Fig. 6.6b,

respectively. The designed bandwidths are adequate to emulate PMSG transient behavior.

6.1.4 Experimental setup description

The PMSG with the compliance element is modeled and solved within the real-time simulator. The PMSG is assumed to be driven by a torque source which can be set as a fixed or an arbitrary time varying input to the power hardware-in-the-loop (PHIL) system. The output of the PMSG model is the line voltages (voltage cross the compliance capacitor C_c) that sets the voltage reference for the power amplifier system. The system emulates a three-phase, 10 hp generator driven by a 15 hp dynamo-meter. The results are also validated against a physical dynamo-meter test bench.

The inverter consists of 1200 V, 50 Ampere semiconductor IGBT half-bridge modules (SKM50GB123D). An inductance of 3 mH and capacitance of 4 μF was used for the LC filter network. The LC filter should have enough bandwidth to replicate the electrical transients of the system. In practice, the response of the emulator which constitutes the following three delay elements namely, (i) LC filter time-constant, (ii) the time delay caused in the controller (T_s), and (iii) the inverter switching delay, should be five times lower compared to the electrical dynamics of the equivalent circuit (Fig. 6.2). Hall effect sensors LA25P are used to sense the inverter currents, the load currents, and LV25P is used to sense the output voltage of the emulator. The schematic of the hardware setup and the controller is shown in Fig. 6.4(a, b). A photograph of the proposed PHIL emulator setup is shown in Fig. 6.7.

An OP4510 real-time processor is used for the real-time simulation of the machine model and for the rapid control prototyping of the power amplifier. Both systems

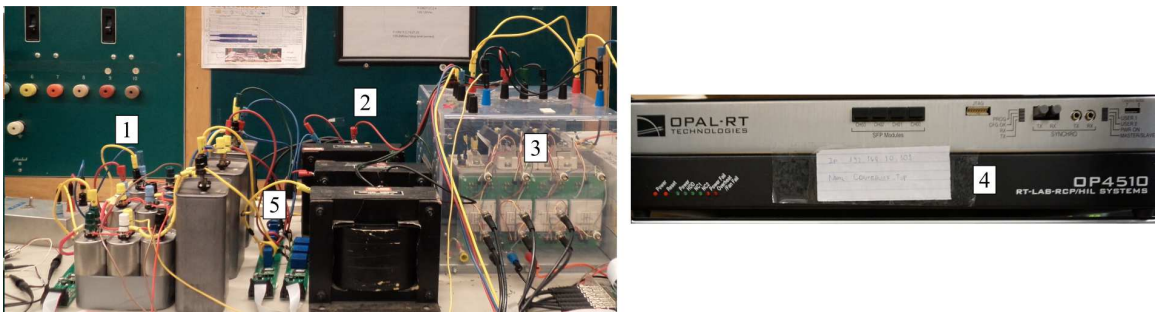

Fig. 6.7: A photograph of the experimental test bench. (1) Capacitors as a part of the LC-filter network; (2) Inductors as a part of LC-filter network; (3) 2-level inverter; (4) Real-time simulator; (5) Hall effect sensors for voltage and current sensing.

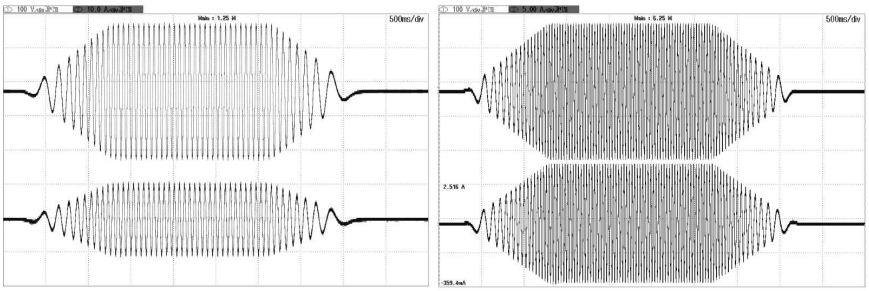

(a) (b)

Fig. 6.8: Transient waveforms of the emulator system, (a) current and voltage waveforms from the proposed emulator, top trace: current, 10 A/div., bottom trace: line voltage, 150 V/div., (b) voltage and current waveforms from the physical dynamometer test bench. top trace: line voltage, 150 V/div., bottom trace: current, 5 A/div., time: 2s/div.

together constitute the power hardware-in-the-loop emulator as the power inverter currents are fed-back into the real-time machine model. The controller was programmed using Matlab-Simulink and a fixed-step solver was used with a sampling frequency of 6 kHz, which is also the switching frequency of the inverter. In most cases, where the PWM is performed by the processor, the sampling duration should be as low as 2 μs for a switching frequency of 6 kHz to maintain fidelity and resolution of the PWM scheme [11]. But in the current scheme, the pulse width modulation is done using the peripheral hardware PWM module allowing the sampling duration to be as large as the switching duration (165 μs). This allows the use of more complicated machine models to be emulated in real-time.

6.1.5 Experimental Results

The system is tested with the dynamometer during start up and run down. The increase in magnitude and frequency of the output voltage can be observed in the physical as well as the emulated system. The torque input for the emulator was given as a repeating sequence with two second rise and fall time. The physical dynamometer's input voltage was manually accelerated and decelerated. Fig. 6.8(a) shows the emulated voltages and currents from the proposed system and Fig. 6.8(b) shows the measured voltage and currents from the physical PMSG dynamometer test bench.

In addition to the emulator response to varying torque inputs, the performance of the emulator to sudden changes in load is also observed. In Fig. 6.9(a) and 6.10(a) the electrical load to the physical dynamometer setup has be switched in (ON) and

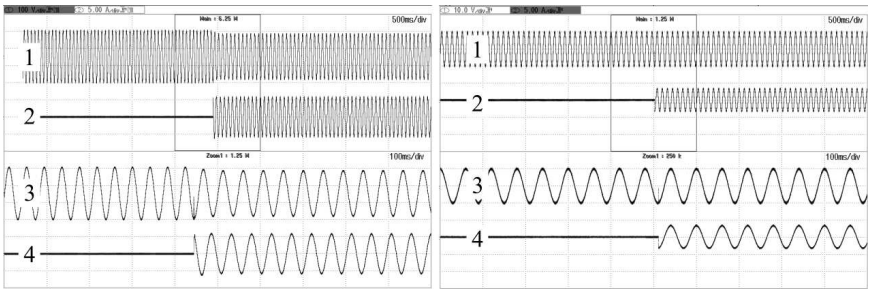

(a) (b)

Fig. 6.9: Transient response of the emulator system for a sudden load increase, (a) voltage and current waveforms from a physical dynamo-meter test bench, trace 1: terminal voltage 100 V/div, trace 2: phase current 5 A/div, trace 3 and trace 4 are the zoomed versions of traces 1 and 2 respectively, (b) voltage and current waveforms from the proposed emulator system, trace 1: terminal voltage 200 V/div, trace 2: phase current 10 A/div, trace 3 and trace 4 are the zoomed versions of traces 1 and 2 respectively.

removed (OFF) respectively. A similar change is presented to the proposed PHIL emulator and their respective transient responses are captured in Fig. 6.9(b) and 6.10(b). It can be seen that the PHIL emulator response and the behavior of the physical test bench are in good agreement. This test also validates the performance and behavior of the PHIL emulator to transient changes in electrical loads.

The emulator system can also be loaded with virtual loads. A virtual load is similar to a load connected to the generator terminals in parallel to already existing physical loads. This allows testing of the machine emulator dynamics at high loads without consuming power. The virtual load port is shown in Fig. 6.1. The virtual load in the proposed emulator is modeled as a current sink that draws power from the motor terminals. In the model, the current sink is connected to the compliance capacitor. This affects the terminal voltage (inputs to equation (24) to (27)) and changes the line currents within the machine model. Fig. 6.11 shows the generator output voltage and current for a ramp change of the virtual load. The virtual load resistor is increased from 50 Ω to 10 kΩ in two seconds.

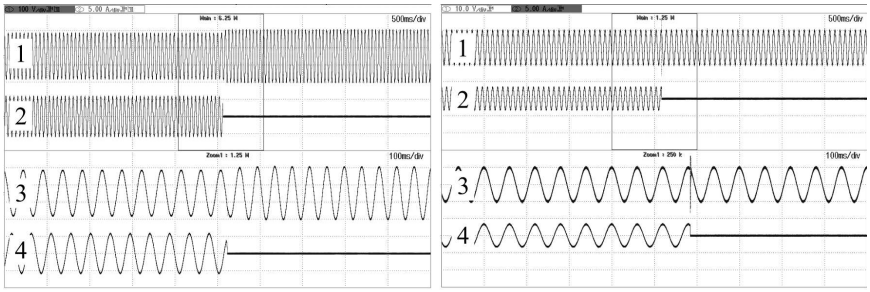

Fig. 6.10: Transient response of the emulator system for a sudden load decrease, (a) voltage and current waveforms from a physical dynamo-meter test bench, trace 1: terminal voltage 100 V/div, trace 2: phase current 5 A/div, trace 3 and trace 4 are the zoomed versions of traces 1 and 2 respectively, (b) voltage and current waveforms from the proposed emulator system, trace 1: terminal voltage 200 V/div, trace 2: phase current 10 A/div, trace 3 and trace 4 are the zoomed versions of traces 1 and 2 respectively.

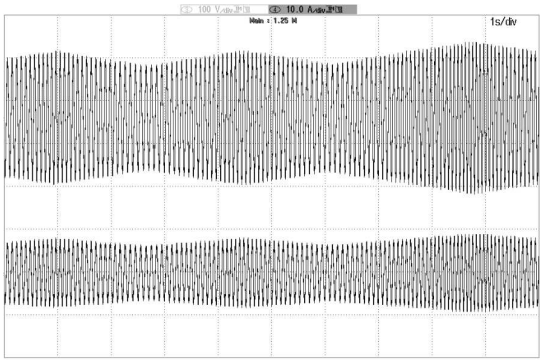

Fig. 6.11: Transient waveforms of the emulator system with increase and decrease in virtual load, top trace: line voltage, 150 V/div., bottom trace: current, 10 A/div., time: 2s/div.

6.2 Hybrid linear-switched power amplifier and control strategy for machine emulation

This work was also co-authored by the author of this thesis. Details are in a transactions paper currently in review. The contributions towards this section by the author of this thesis, alone are discussed in this section. An illustration of the proposed hybrid amplifier is shown in Fog. 6.12. The system consists of two sets of amplifiers, (i) a switched mode power amplifier (termed as the SMPA in Fig. 6.12) composed of two-level converters as discussed in Chapter 2, and (ii) linear amplifiers (termed as LPA in Fig. 6.12) as discussed in Chapter 3. The LPA is connected directly to the

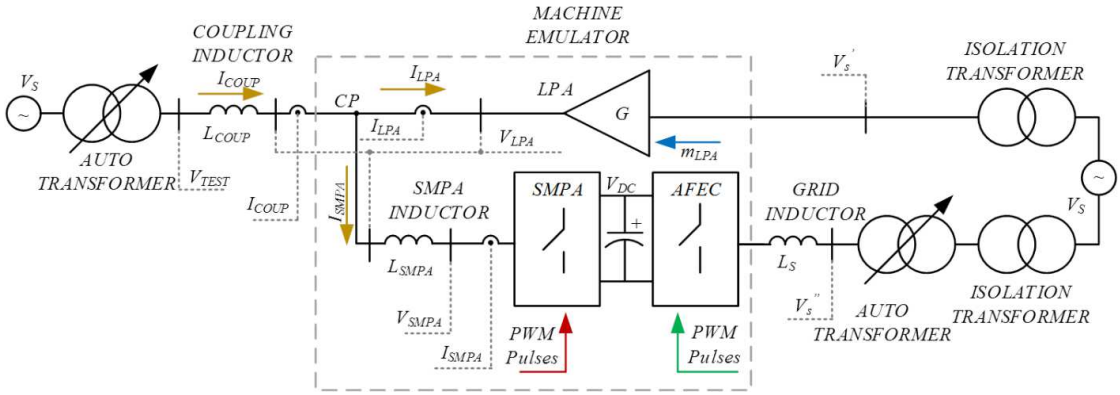

Fig. 6.12: Proposed machine emulator built with the parallel association of a SMPA and a LPA]

coupling inductance, L_{COUP}, while the SMPA is connected to the same node through another inductance, L_{SMPA}. There are isolation transformers in both grid sides of the LPA and SMPA to prevent circulating currents. At the left side of the coupling inductance, there is an auto-transformer used to control and adjust the grid voltage, V_{TEST}, applied to the emulated induction machine.

The HPA (indicated in Fog. 6.12) is current controlled as illustrated in detail in Fig. 6.13. The grid voltage, V_{TEST}, is measured and applied across the machine model, the RTS computes the machine currents, I^*_{COUP}. This current, I^*_{COUP} is used as the reference current for the LPA similar to as discussed in Chapter 3. The actual/sensed current, I_{COUP}, which is feedback current of the LPA current control loop also serves as a reference current for the SMPA current control loop, I^*_{SMPA}. The key requirement in the proposed scheme concerns the relation of the bandwidths for these two current control loops. It is necessary to ensure that the bandwidth of the LPA current control loop is much higher than the bandwidth of the SMPA current control loop. If this condition is ensured, the LPA will act for sudden changes to the I^*_{COUP}, whereas, the SMPA will provide the slower changes in the I^*_{COUP}. This control will hence ensure that at steady state, the LPA output current, I_{LPA} will tend to be equal to the switching ripple and other harmonics generated by the SMPA alone.

Simple PI controllers are used for the current control loops of the SMPA and the LPA. The highest closed loop bandwidth achieved for the LPA is 2.7 kHz. The highest closed loop bandwidth achieved for the SMPA is 1 kHz. In addition, the SMPA, due to its switching dead-time also generates 5^th and 7^th harmonics. To suppress these components, in addition to PI controllers, the current control loop of the LPA also

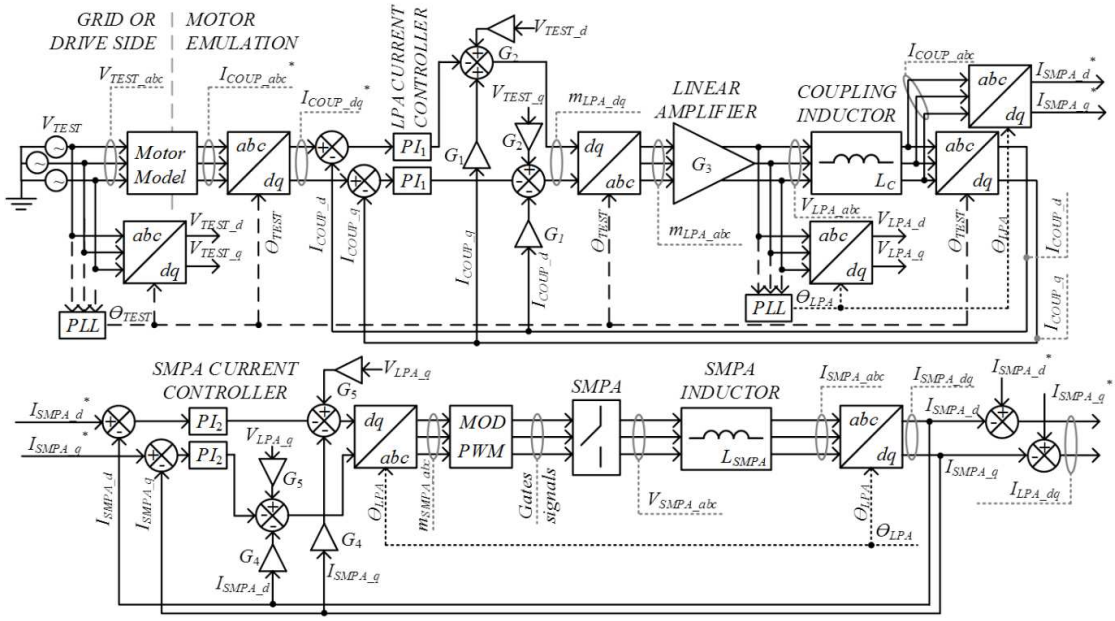

Fig. 6.13: Proposed current control scheme for the hybrid power amplifier

contains a resonant controller at the 6^th harmonic in the dq frame. Detailed control design is not presented here since it is essentially a repetition of the discussions in Chapters 2-5. With the proposed control for the HPA, the bandwidth of the HPA is equal to the bandwidth of the LPA. Furthermore, due to the presence of the SMPA, the HPA is able to achieve a power rating equal to that of the SMPA as well. Hence the proposed HPA system combines the benefits of the SMPA and that of the LPA, as discussed earlier in Chapter 2 and Chapter 3, respectively.

6.2.1 Experimental setup

Fig.!6.14 shows the experimental setup of the proposed HPA. The constituent LPA and the SMPA of the HPA are also indicated in the figure. The same LPA as used in Chapter 3 is used here as well. The same topology for the SMPA as discussed in Chapter 2 has been implemented in the HPA here. Results were collected using a Yokogawa DLM3000 mixed signal oscilloscope. It monitors the DC bus voltage, between AFEC and SMPA, and the currents of the SMPA, LPA and AFEC. The LPA and the SMPA are controlled using a model built using MATLAB/SIMULINK® and implemented in real-time using an OPAL-RT based RTS [55]. The system also contains an external protection circuit which blocks gating pulses to the SMPA and AFEC, and disconnects the LPA in the event of a fault.

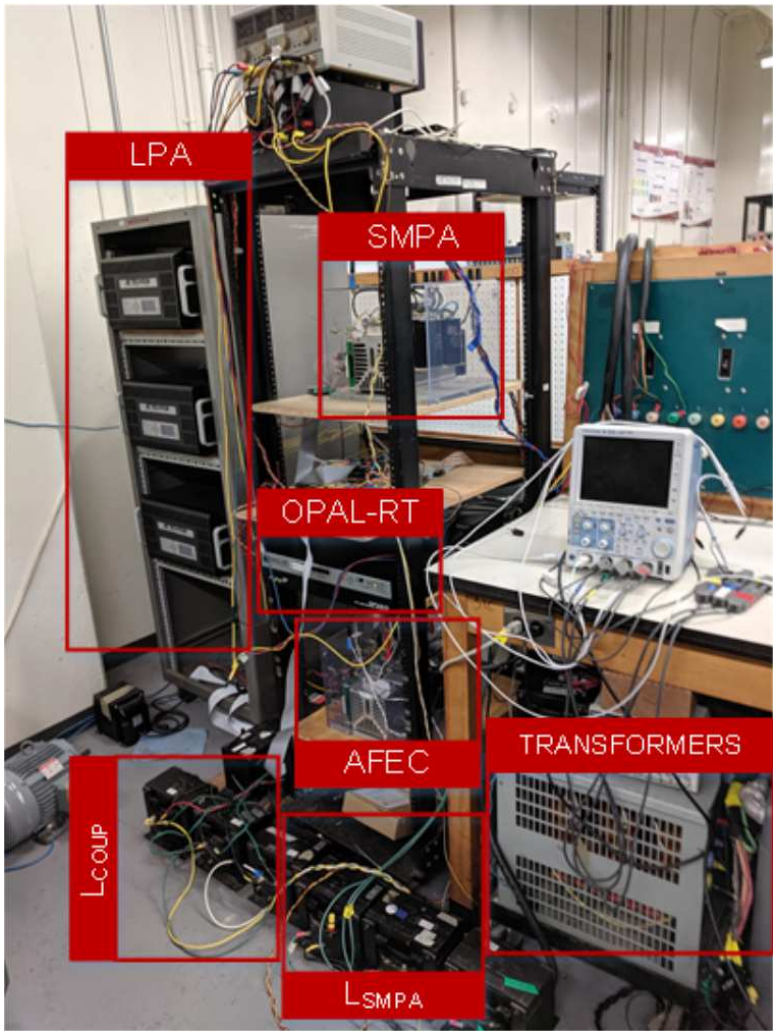

Fig. 6.14: Experimental setup of the proposed HPA motor emulator setup.

The coupling inductors (L_{COUP}) and the inductors connecting the SMPA to the LPA (L_{SMPA}) are also shown in the figure. The transformer shown in the schematic provides isolation and prevents circulating currents in the experimental setup. An auto-transformer (not shown in the schematic) reduces the voltage applied across the emulated induction machine. This reduces the currents to within the SMPA limits for direct-online-start-up of the emulated induction motor.

6.2.2 Experimental results

The experimental results obtained for the emulation of an induction motor (IM) using the proposed HPA are presented in this section. The transient condition emulated is a

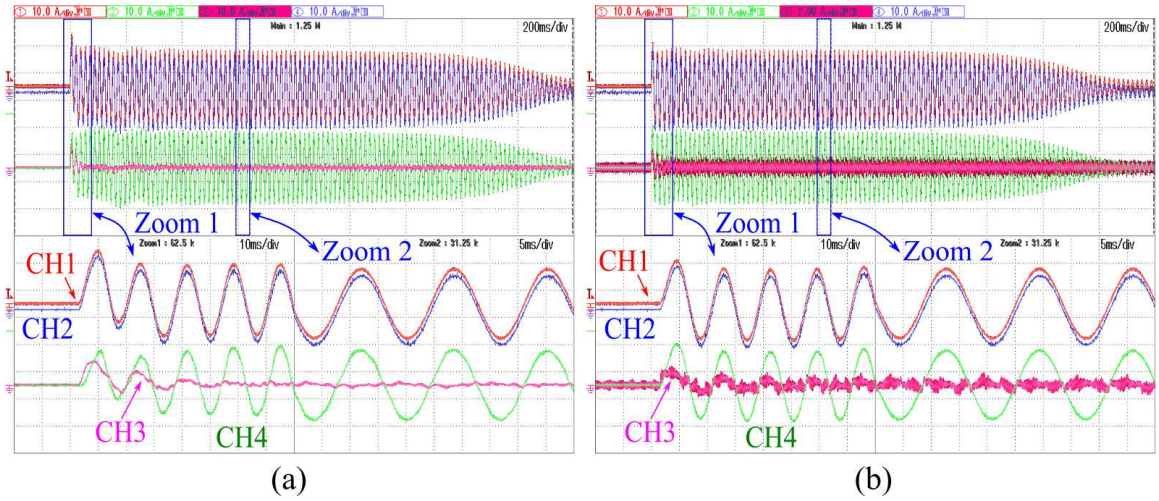

Fig. 6.15: Experimental results obtained from the HPA for an IM DOL start-up (a) SMPA BW= 150 Hz; SMPA F_{SW} = 10 kHz, (b) SMPA BW= 1000 Hz; SMPA F_{SW} = 10 kHz: CH1 (10 A/div) is the reference machine current, CH2 (10 A/div) is the emulated current drawn by the HPA, CH3 (10 A/div in (a) and 2 A/div in (b)) is the current drawn by the LPA, CH4 (10 A/div) is the current drawn by the SMPA

direct-on-line (DOL) start-up of an induction motor. The emulated IM is at no-load. Therefore, the machine has a high inrush current during start-up and this current comes down to a low value once the machine reaches close to its synchronous speed.

Fig. 6.15 presents the case when the switching frequency of the SMPA is kept fixed at 10 kHz. The SMPA bandwidth however is varied to 150 Hz in Fig. 6.15(a) and 1 kHz in Fig. 6.15(b), respectively. Looking at these results first, it is clear that the LPA only provides the initial in-rush current for a short period of time, and in steady state the LPA supplies the switching ripple and the current harmonics due to SMPA switching dead-time. However, the peak value of the LPA current is inversely proportional to the SMPA current control bandwidth. In Fig. 6.15(a) when the SMPA current control bandwidth is 150 Hz, the LPA peak current is close to 10 A. In Fig. 6.15(b) when the SMPA current control bandwidth is 1 kHz, the LPA peak current is limited to less than 2 A peak. Hence, it is important to ensure that the SMPA current control bandwidth is not too low compared to the LPA current control bandwidth. Or in other words, if the emulated system behavior (the IM DOL start-up in this case) requires a much higher bandwidth than the current control bandwidth of the SMPA, the LPA would end up supplying the required peak current. This would mean that the LPA will need to be designed for a higher peak current rating, increasing the cost of the HPA system.

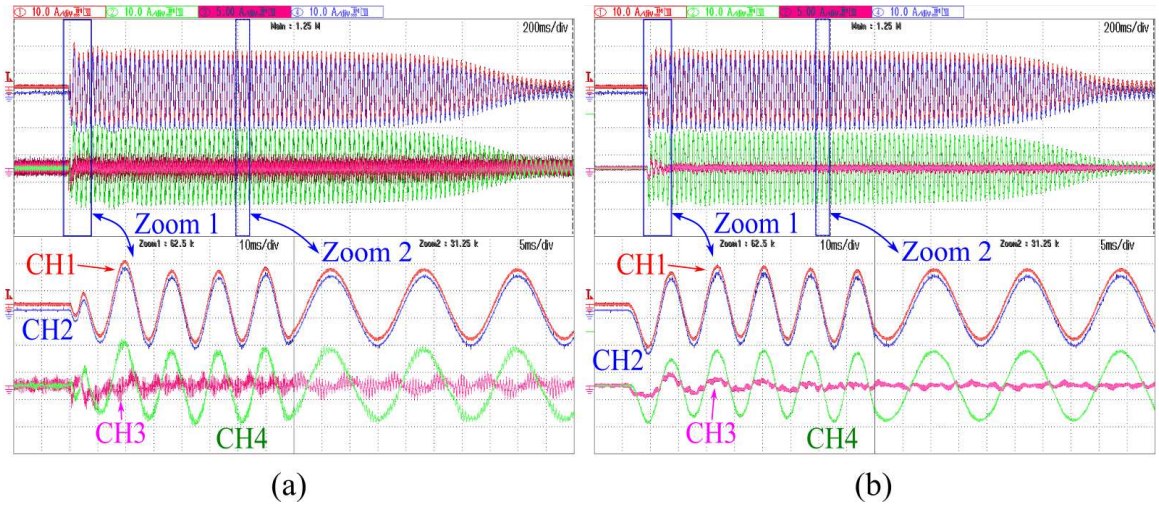

Fig. 6.16: Experimental results obtained from the HPA for an IM DOL start-up (a) LPA BW= 2.7 kHz; SMPA BW= 350 Hz; SMPA F_{SW} = 2 kHz, (b) LPA BW= 2.7 kHz; SMPA BW= 350 Hz; SMPA F_{SW} = 10 kHz: CH1 (10 A/div) is the reference machine current, CH2 (10 A/div) is the emulated current drawn by the HPA, CH3 (5 A/div) is the current drawn by the LPA, CH4 (10 A/div) is the current drawn by the SMPA

In the results presented in Fig. 6.16, bandwidth of the SMPA and the LPA is kept fixed at 350 Hz and 2.7 kHz, respectively. The switching frequency of the SMPA is however 2 kHz in Fig. 6.16(a) and 10kHz in Fig. 6.16(b). It can be seen that the peak current supplied by the LPA is similar in both cases. Moreover, the emulated HPA current is also similar in both cases. The LPA in Fig. 6.16(a) has to supply a higher steady state ripple current since the switching frequency of the SMPA is lower. But, this value of current is still lesser than the peak current rating required off the LPA. The lower switching frequency of the SMPA in Fig. 6.16(a) as compared to Fig. 6.16(b) however leads to lower switching losses in the SMPA and hence again indirectly reduces the cost of the HPA system. This leads to another design criterion of the HPA system where the objective is to keep the SMPA switching frequency at its minimum value to again reduce the cost of the overall HPA system. Detailed discussions of the same are presented in the transactions paper co-authored and currently under review.

6.3 Summary

The works presented in this chapter were completed in collaboration with other students of the PEER group in Concordia. This chapter presented a brief overview of the both the works. Contributions of the author of this thesis in both these works were primarily towards control design and hardware implementation. The main summarizing comments are as follows.

A. Emulation of a permanent magnet synchronous generator.

   - A torque-driven model of a permanent magnet synchronous generator was developed. The causality problem of the output voltage of the machine being load current dependent, was solved by placing a *compliance* capacitor at the model output terminals. This *compliance* capacitor could be representative of the inter-winding capacitance of a physical machine. It was shown that the *compliance* capacitor needs to be small enough to minimize the error introduced, but also large enough to ensure model stability.
   - The developed machine model was used in the PMSG emulator. This machine emulator was essentially a two-level VSC terminated with an LC filter. Cascaded two-loop control was used in the machine emulator to control its output voltage to a value dictated by the developed PMSG model.
   - Experimental results were presented to illustrate the utility of the developed PHIL based PMSG machine emulator to drive linear and non-linear loads, and for sudden load changes.

B. Development of a hybrid power amplifier for machine emulation.

   - The developed hybrid amplifier is essentially a parallel combination of a switched mode power amplifier(SMPA) discussed in Chapter 2 and a linear amplifier(LPA) discussed in Chapter 3. The objective of developing the hybrid power amplifier is to esssentially combine the features of an LPA (high bandwidth) and the SMPA (high power output).
   - A simple current control strategy was proposed for the LPA and the SMPA of the hybrid power amplifier. Experimental results were presented to prove the validity of the proposed current control technique.

- The ratio of the current control bandwidths of the LPA to the SMPA in relation with the bandwidth demanded off the HPA dictates the sizing of the LPA and the SMPA. This in turn influences the overall cost of the HPA solution. The two inferences that were made are:
  - The larger the bandwidth ratio of the LPA to the SMPA, larger is the peak current rating of the LPA. This implies a higher cost of the hybrid power amplfier.
  - Lower the switching frequency of the SMPA, lower is the cost of the SMPA leading to a lower cost of the hybrid power amplifier.
- The hybrid power amplifier sizing is hence an optimization problem which depends on the bandwidth required of the hybrid power amplifier, the peak current rating of the LPA and the switching frequency of the SMPA.

Chapter 7

Conclusions and future works

The focus of this PhD research work was towards the emulation of permanent magnet machines. The main conclusions of this thesis and the future works corresponding to each chapters are presented below.

7.1 Development of a machine emulator test-bench

The machine emulator developed as part of this chapter consisted of two two-level VSCs connected in a back-back fashion to form a machine emulator which can operate in all four quadrants. The main conclusions are as follows:

- The developed machine emulator can emulate machines at a closed loop bandwidth of 2 kHz and an emulation power of 20 kVA.
- A current control technique was introduced for the machine emulator control. It was shown that the current control bandwidth of the emulator needs to be at least five times faster than the current control bandwidth of the drive inverter. Therefore, with the developed emulator which has a closed loop current control bandwidth of 2 kHz, drive inverters with a closed loop current control bandwidth of up to 400 Hz can be tested.
- The developed emulator system was shown to use detailed FEA based PM machine models for the purpose of emulation.
- Experimental results were presented for the emulation of a surface-mounted PMSM. Experimental results were also presented to showcase the benefit of using detailed machine models for the purpose of emulation.

The proposed future works that can be investigated as part of this chapter are as follows:

- The emulator control presented in this chapter directly senses the switching voltage output of the driving inverter. This would mean that ADC sampling could introduce several errors, especially if low-cost low-resolution ADCs are used to save cost. Investigations to improve the process of driving inverter voltage sensing either using software or hardware filters and correcting the resulting errors introduced, can be one of the future works.

- The driving inverter in all chapter of this thesis is assumed to operate in field-oriented vector control. Machine emulation and the resulting control bandwidth constraints when the driving inverter operates with other control strategies such as direct-torque control, can be investigated.

- The machine emulator does not take into account the thermal behavior of the emulated machine. The same can be introduced by developing machine models which changes its parameter lookup table based on the emulated temperature of the machine. This would allow a more comprehensive testing of the electric drive system.

- The machine look-up table model used in the emulation system developed in this chapter is a voltage-in current-out model. Such a model which takes voltage as an input and outputs the corresponding current allows easily for current control of the machine emulator. Detailed machine models can be developed which are current-in voltage-out. Such models would take currents as inputs and output the corresponding voltage across the machine terminals. This would allow for emulator voltage control. Controlling the emulator in voltage control mode would mean that the bandwidth restriction of the driving inverter current control loop can be further relaxed.

7.2 Linear amplifier based emulation of a variable-flux machine

This chapter presented the development of a linear amplifier based machine emulator system. The developed experimental setup was used to emulate a variable flux-machine (VFM). The conclusions of this chapter are as follows:

- The developed machine emulator can emulate machines at a closed loop bandwidth of 7.5 kHz and an emulation power of 7.5 kVA.
- Experimental results were presented to validate the emulation of a VFM. Emulation was performed for a VFM at different magnetization states, implying the requirement of multiple machine parameter look-up tables.

The proposed future works that can be investigated as part of this chapter are as follows:

- The linear amplifiers have an open-loop bandwidth of 200 kHz. The closed loop emulation bandwidth is still limited to 7.5 kHz due to the controller loop time of 5 μs. With faster ADCs and DACs, the controller loop time can be reduced further which can increase the closed loop emulation bandwidth significantly. With a higher emulation bandwidth, the resulting emulation would be of a higher accuracy as well.
- The VFM was emulated at different discrete magnetization states. However, it is important to define the emulated machine behavior during the changeover in its magnetization state as well. A simplified model of the machine behavior can be developed to define the emulator operation during the magnetization state changeover. Detailed models of the machines can be used at different discrete magnetization states. The two models can be used together to be able to completely define VFM machine behavior for all operating conditions.

7.3 Machine emulation to investigate driving inverter faults

The emulator system developed in Chapter 3 was used to emulate machine behavior in the event of driving inverter faults. The main conclusions of this chapter are as follows:

- Emulation of machine behavior was presented for gate-drive faults of the driving inverter. It was shown that the current control proposed in the earlier chapters can sustain if there is a fault in one switch or two switches of the driving inverter.

- An improved current controller which uses resonant controllers working in tandem with PI controllers was presented. A closed loop current control bandwidth of 7.5 kHz was attained with selective high open-loop controller gains at various lower order harmonics of interest.

- Control structure modification from current to voltage control was required for the emulator control in the event of a complete gate-unit failure of the driving inverter. Experimental results were presented to prove the proposed emulator control structure and the improved current controller.

The proposed future works that can be investigated as part of this chapter are as follows:

- The current control to voltage control switchover for machine emulation in the event of a complete gate-unit failure of the driving inverter might not be the best solution. The reliability of this control switchover is questionable, particularly due its dependence on the fault-detection. Other control approaches can be investigated. For instance if the machine emulator were to operate in voltage control mode from the beginning (as suggested in the future work of Chapter 2), this control switchover will not even be required.

- Only a few driving inverter faults were considered as part of this chapter. Emulation of machine behavior for other driving inverter faults can also be considered.

- The emulation of faults in a machine is another topic which can be addressed as a future work as well. With emulation of machine faults the benefits of machine emulation as compared to the conventional approach to drive system testing can be completely harnessed.

7.4 Open-winding machine: control and emulation

This chapter presented an emulator setup to emulate open-winding PM machines. The main conclusions are as follows:

- The developed emulator system was capable of emulating open-winding PM machines of up to 5 HP, with an emulating bandwidth of 7.5 kHz.

- Current control similar to that proposed in Chapter 4 was used. Current controllers were also added in the *zero*-sequence frame to control corresponding currents.

- Experimental results were presented to validate the developed emulator system and the proposed current control technique. A torque-ripple minimization algorithm available in literature was implemented to showcase the utility of the developed emulator system.

The proposed future works that can be investigated as part of this chapter are as follows:

- A simplified machine model was used for the emulation presented in this chapter. A detailed model of the machine based on parameter look-up table data, capable of representing open-winding machine behavior, can be investigated as part of the future work.

- An open-winding PM machine is essentially a fault-tolerant drive. Emulation was presented for two-phase operation of the machine. Emulation of other fault modes, and fault mode operation algorithms can also be investigated as part of the future work.

7.5 PM generator emulation and hybrid power amplifier design

This chapter presented the works done in collaboration with other students of the PEER group. The main conclusions are as follows:

- An emulator setup for generator emulation was developed with a torque-driven model of a permanent magnet synchronous generator (PMSG). This model consists of a *compliance* capacitance at it's output terminals.

- Experimental results were presented for the developed PMSG emulator setup for various transient operating conditions.

- A hybrid emulator setup was developed with a parallel combination of the a two-level VSC based power amplifier and a linear amplifier based power amplifier.

- Experimental results were presented to validate the developed hybrid emulator system control and the emulation of an induction motor for start-up conditions.

The proposed future works that can be investigated as part of this chapter are as follows:

- The use of detailed machine models using parameter look-up table data can be investigated for the emulation of a PMSG.
- This chapter presented a few preliminary results pertaining to the hybrid machine emulator operation. Detailed investigation of this topology, such as bandwidth optimization, cost optimization, etc., can be investigated as part of the future work.

References

[1] A. M. El-Refaie, "Motors/generators for traction/propulsion applications: A review," *IEEE Vehicular Technology Magazine*, vol. 8, no. 1, pp. 90–99, March 2013.

[2] B. Bilgin, P. Magne, P. Malysz, Y. Yang, V. Pantelic, M. Preindl, A. Korobkine, W. Jiang, M. Lawford, and A. Emadi, "Making the case for electrified transportation," *IEEE Transactions on Transportation Electrification*, vol. 1, no. 1, pp. 4–17, June 2015.

[3] A. M. El-Refaie, "Fault-tolerant permanent magnet machines: a review," *IET Electric Power Applications*, vol. 5, no. 1, pp. 59–74, January 2011.

[4] E. Levi, "Multiphase electric machines for variable-speed applications," *IEEE Transactions on Industrial Electronics*, vol. 55, no. 5, pp. 1893–1909, May 2008.

[5] K. T. Chau, C. C. Chan, and C. Liu, "Overview of permanent-magnet brushless drives for electric and hybrid electric vehicles," *IEEE Transactions on Industrial Electronics*, vol. 55, no. 6, pp. 2246–2257, June 2008.

[6] C. C. Chan, "The state of the art of electric, hybrid, and fuel cell vehicles," *Proceedings of the IEEE*, vol. 95, no. 4, pp. 704–718, April 2007.

[7] J. A. P. Lopes, F. J. Soares, and P. M. R. Almeida, "Integration of electric vehicles in the electric power system," *Proceedings of the IEEE*, vol. 99, no. 1, pp. 168–183, Jan 2011.

[8] J. H. Kim, Y. Li, and B. Sarlioglu, "Novel six-slot four-pole axial flux-switching permanent magnet machine for electric vehicle," *IEEE Transactions on Transportation Electrification*, vol. 3, no. 1, pp. 108–117, March 2017.

[9] Z. Yang, F. Shang, I. P. Brown, and M. Krishnamurthy, "Comparative study of interior permanent magnet, induction, and switched reluctance motor drives for ev and hev applications," *IEEE Transactions on Transportation Electrification*, vol. 1, no. 3, pp. 245–254, Oct 2015.

[10] E. Bostanci, M. Moallem, A. Parsapour, and B. Fahimi, "Opportunities and challenges of switched reluctance motor drives for electric propulsion: A comparative study," *IEEE Transactions on Transportation Electrification*, vol. 3, no. 1, pp. 58–75, March 2017.

[11] H. J. Slater, D. J. Atkinson, and A. G. Jack, "Real-time emulation for power equipment development. ii. the virtual machine," *IEE Proceedings - Electric Power Applications*, vol. 145, no. 3, pp. 153–158, May 1998.

[12] A. Schmitt, J. Richter, M. Gommeringer, T. Wersal, and M. Braun, "A novel 100 kw power hardware-in-the-loop emulation test bench for permanent magnet synchronous machines with nonlinear magnetics," in *8th IET International Conference on Power Electronics, Machines and Drives (PEMD 2016)*, April 2016, pp. 1–6.

[13] O. Vodyakho, M. Steurer, C. S. Edrington, and F. Fleming, "An induction machine emulator for high-power applications utilizing advanced simulation tools with graphical user interfaces," *IEEE Transactions on Energy Conversion*, vol. 27, no. 1, pp. 160–172, March 2012.

[14] R. M. Kennel, T. Boller, and J. Holtz, "Replacement of electrical (load) drives by a hardware-in-the-loop system," in *International Aegean Conference on Electrical Machines and Power Electronics and Electromotion, Joint Conference*, Sept 2011, pp. 17–25.

[15] A. Schmitt, J. Richter, U. Jurkewitz, and M. Braun, "Fpga-based real-time simulation of nonlinear permanent magnet synchronous machines for power hardware-in-the-loop emulation systems," in *IECON 2014 - 40th Annual Conference of the IEEE Industrial Electronics Society*, Oct 2014, pp. 3763–3769.

[16] T. Boller and R. M. Kennel, "Virtual machine – a hardware in the loop test for drive inverters," in *2009 13th European Conference on Power Electronics and Applications*, Sept 2009, pp. 1–5.

[17] R. S. Kaarthik and P. Pillay, "Emulation of a permanent magnet synchronous generator in real-time using power hardware-in-the-loop," in *2016 IEEE International Conference on Power Electronics, Drives and Energy Systems (PEDES)*, Dec 2016, pp. 1–6.

[18] Y. S. Rao and M. C. Chandorkar, "Real-time electrical load emulator using optimal feedback control technique," *IEEE Transactions on Industrial Electronics*, vol. 57, no. 4, pp. 1217–1225, April 2010.

[19] S. Grubic, B. Amlang, W. Schumacher, and A. Wenzel, "A high-performance electronic hardware-in-the-loop drive – load simulation using a linear inverter (linverter)," *IEEE Transactions on Industrial Electronics*, vol. 57, no. 4, pp. 1208–1216, April 2010.

[20] M. A. Masadeh, K. S. Amitkumar, and P. Pillay, "Power electronic converter-based induction motor emulator including main and leakage flux saturation," *IEEE Transactions on Transportation Electrification*, vol. 4, no. 2, pp. 483–493, June 2018.

[21] A. Hoke, S. Chakraborty, and T. Basso, "A power hardware-in-the-loop framework for advanced grid-interactive inverter testing," in *2015 IEEE Power Energy Society Innovative Smart Grid Technologies Conference (ISGT)*, Feb 2015, pp. 1–5.

[22] G. F. Lauss, M. O. Faruque, K. Schoder, C. Dufour, A. Viehweider, and J. Langston, "Characteristics and design of power hardware-in-the-loop simulations for electrical power systems," *IEEE Transactions on Industrial Electronics*, vol. 63, no. 1, pp. 406–417, Jan 2016.

[23] R. S. Kaarthik, J. Maisonneuve, and P. Pillay, "Real-time emulation of a pressure-retarded osmotic power generation system," *IEEE Transactions on Industry Applications*, vol. 53, no. 6, pp. 5768–5776, Nov 2017.

[24] K. S. Amitkumar, R. S. Kaarthik, and P. Pillay, "A versatile power-hardware-in-the-loop based emulator for rapid testing of electric drives," in *2017 IEEE Energy Conversion Congress and Exposition (ECCE)*, Oct 2017, pp. 5468–5474.

[25] F. E. Fleming and C. S. Edrington, "Real-time emulation of switched reluctance machines via magnetic equivalent circuits," *IEEE Transactions on Industrial Electronics*, vol. 63, no. 6, pp. 3366–3376, June 2016.

[26] K. S. Amitkumar, R. S. Kaarthik, and P. Pillay, "A versatile power-hardware-in-the-loop based emulator for rapid testing of transportation electric drives," *IEEE Transactions on Transportation Electrification*, pp. 1–1, 2018.

[27] F. Huerta, R. L. Tello, and M. Prodanovic, "Real-time power-hardware-in-the-loop implementation of variable-speed wind turbines," *IEEE Transactions on Industrial Electronics*, vol. 64, no. 3, pp. 1893–1904, March 2017.

[28] M. Ashourianjozdani, L. A. C. Lopes, and P. Pillay, "Converter-based pmsg emulator: A testbed for renewable energy experiments," in *2017 IEEE International Electric Machines and Drives Conference (IEMDC)*, May 2017, pp. 1–7.

[29] R. S. Kaarthik, K. S. Amitkumar, and P. Pillay, "Emulation of a permanent magnet synchronous generator in real-time using power hardware-in-the-loop," *IEEE Transactions on Transportation Electrification*, vol. PP, no. 99, pp. 1–1, 2017.

[30] Y. Lee, Y. Kwon, and S. Sul, "Dc-link voltage design of high-bandwidth motor emulator for interior permanent-magnet synchronous motors," in *2018 IEEE Energy Conversion Congress and Exposition (ECCE)*, Sep. 2018, pp. 4453–4459.

[31] L. Wang and J. Jatskevich, "A voltage-behind-reactance induction machine model for the emtp-type solution," in *2009 IEEE Power Energy Society General Meeting*, July 2009, pp. 1–1.

[32] O. A. Mohammed, S. Liu, and Z. Liu, "A phase variable model of brushless dc motors based on finite element analysis and its coupling with external circuits," *IEEE Transactions on Magnetics*, vol. 41, no. 5, pp. 1576–1579, May 2005.

[33] M. Fazil and K. R. Rajagopal, "Nonlinear dynamic modeling of a single-phase permanent-magnet brushless dc motor using 2-d static finite-element results," *IEEE Transactions on Magnetics*, vol. 47, no. 4, pp. 781–786, April 2011.

[34] P. P. Silvester and R. P. Gupta, "Effective computational models for anisotropic soft b-h curves," *IEEE Transactions on Magnetics*, vol. 27, no. 5, pp. 3804–3807, Sept 1991.

[35] T. Ould-Bachir, C. Dufour, J. Bélanger, J. Mahseredjian, and J. P. David, "Effective floating-point calculation engines intended for the fpga-based hil simulation,"

in *2012 IEEE International Symposium on Industrial Electronics*, May 2012, pp. 1363–1368.

[36] D. N. Dyck, T. Rahman, and C. Dufour, "Internally consistent nonlinear behavioral model of a pm synchronous machine for hardware-in-the-loop simulation," *IEEE Transactions on Magnetics*, vol. 50, no. 2, pp. 853–856, Feb 2014.

[37] S. Abourida, C. Dufour, J. Bélanger, T. Yamada, and T. Arasawa, "Hardware-in-the-loop simulation of finite-element based motor drives with rt-lab and jmag," in *2006 IEEE International Symposium on Industrial Electronics*, vol. 3, July 2006, pp. 2462–2466.

[38] C. Dufour, S. Cense, T. Yamada, R. Imamura, and J. Bélanger, "Fpga permanent magnet synchronous motor floating-point models with variable-dq and spatial harmonic finite-element analysis solvers," in *2012 15th International Power Electronics and Motion Control Conference (EPE/PEMC)*, Sept 2012, pp. LS6b.2–1–LS6b.2–10.

[39] Y. Inaba, S. Cense, T. O. Bachir, H. Yamashita, and C. Dufour, "A dual high-speed pmsm motor drive emulator with finite element analysis on fpga chip with full fault testing capability," in *Proceedings of the 2011 14th European Conference on Power Electronics and Applications*, Aug 2011, pp. 1–10.

[40] M. Fischer, "Design of a three-phase 100a linear amplifier for power-hardware-in-the-loop machine emulation," *The Journal of Engineering*, vol. 2019, pp. 4041–4044(3), June 2019. [Online]. Available: https://digital-library.theiet.org/content/journals/10.1049/joe.2018.8142

[41] D. Kastha and B. K. Bose, "Investigation of fault modes of voltage-fed inverter system for induction motor drive," *IEEE Transactions on Industry Applications*, vol. 30, no. 4, pp. 1028–1038, July 1994.

[42] H. T. Eickhoff, R. Seebacher, A. Muetze, and E. G. Strangas, "Enhanced and fast detection of open-switch faults in inverters for electric drives," *IEEE Transactions on Industry Applications*, vol. 53, no. 6, pp. 5415–5425, Nov 2017.

[43] W. Sleszynski, J. Nieznanski, and A. Cichowski, "Open-transistor fault diagnostics in voltage-source inverters by analyzing the load currents," *IEEE Transactions on Industrial Electronics*, vol. 56, no. 11, pp. 4681–4688, Nov 2009.

[44] B. Lu and S. K. Sharma, "A literature review of igbt fault diagnostic and protection methods for power inverters," *IEEE Transactions on Industry Applications*, vol. 45, no. 5, pp. 1770–1777, Sep. 2009.

[45] H. Nian and W. Hu, "Torque ripple suppression method with reduced switching frequency for open-winding pmsm drives with common dc bus," *IEEE Transactions on Industrial Electronics*, pp. 1–1, 2018.

[46] S. Dai, J. Wei, B. Zhou, and J. Xue, "The control strategy of open-winding permanent magnet synchronous motor drive system based on five-leg inverter," in *2016 IEEE Vehicle Power and Propulsion Conference (VPPC)*, Oct 2016, pp. 1–5.

[47] F. Aghili, "Method and apparatus for improving output of a multi-winding motor," U.S. Patent 8 994 308 B2, 31, 2015.

[48] ——, "Optimal and fault-tolerant torque control of servo motors subject to voltage and current limits," *IEEE Transactions on Control Systems Technology*, vol. 21, no. 4, pp. 1440–1448, July 2013.

[49] J. S. S. Prasad, T. Bhavsar, R. Ghosh, and G. Narayanan, "Vector control of three-phase ac/dc front-end converter," *Sadhana*, vol. 33, no. 5, pp. 591–613, 2008.

[50] *OP4510 RT-LAB-RCP/HIL SYSTEMS: User Guide*, OPAL-RT Technologies, 12 2015.

[51] *OP5511 High-current and high-voltage input conditioning module*, OPAL-RT Technologies, 9 2016, rev. E.

[52] M. Ibrahim, L. Masisi, and P. Pillay, "Design of variable-flux permanent-magnet machines using alnico magnets," *IEEE Transactions on Industry Applications*, vol. 51, no. 6, pp. 4482–4491, Nov 2015.

[53] L. Masisi, M. Ibrahim, and P. Pillay, "Control strategy of a variable flux machine using alnico permanent magnets," in *2015 IEEE Energy Conversion Congress and Exposition (ECCE)*, Sept 2015, pp. 5249–5255.

[54] AETechron. (2015) Aetechron-7548 datasheet. [Online]. Available: http://aetechron.com/pdf/7548specsheet.pdf

[55] OPAL-RT. (2015) Op4510 datasheet. [Online]. Available: https://www.opal-rt.com/wp-content/themes/enfold-opal/pdf/L00161_0124.pdf

[56] V. Ostovic, "Memory motors," *IEEE Industry Applications Magazine*, vol. 9, no. 1, pp. 52–61, Jan 2003.

[57] R. Thike and P. Pillay, "Characterization of a variable flux machine for transportation using a vector-controlled drive," *IEEE Transactions on Transportation Electrification*, vol. 4, no. 2, pp. 494–505, June 2018.

[58] ——, "Automatic inductance measurements of synchronous reluctance machines including cross-saturation using real-time systems," in *2018 IEEE Energy Conversion Congress and Exposition (ECCE)*, Sep. 2018, pp. 6121–6127.

[59] Y. Chen and V. Dinavahi, "Digital hardware emulation of universal machine and universal line models for real-time electromagnetic transient simulation," *IEEE Transactions on Industrial Electronics*, vol. 59, no. 2, pp. 1300–1309, Feb 2012.

[60] B. Jandaghi and V. Dinavahi, "Real-time hil emulation of faulted electric machines based on nonlinear mec model," *IEEE Transactions on Energy Conversion*, vol. 34, no. 3, pp. 1190–1199, Sep. 2019.

[61] C. Dufour, S. Cense, and J. Blanger, "An induction machine and power electronic test system on a field-programmable gate array," *Mathematics and Computers in Simulation*, vol. 130, pp. 112 – 123, 2016, 11th International Conference on Modeling and Simulation of Electric Machines, Converters and Systems. [Online]. Available: http://www.sciencedirect.com/science/article/pii/S0378475416300659

[62] C. Dufour, S. Cense, T. Ould-Bachir, L. Grgoire, and J. Blanger, "General-purpose reconfigurable low-latency electric circuit and motor drive solver on fpga," in *IECON 2012 - 38th Annual Conference on IEEE Industrial Electronics Society*, Oct 2012, pp. 3073–3081.

[63] R. Teodorescu, F. Blaabjerg, M. Liserre, and P. C. Loh, "Proportional-resonant controllers and filters for grid-connected voltage-source converters," *IEE Proceedings - Electric Power Applications*, vol. 153, no. 5, pp. 750–762, Sep. 2006.

[64] A. Timbus, M. Liserre, R. Teodorescu, P. Rodriguez, and F. Blaabjerg, "Evaluation of current controllers for distributed power generation systems," *IEEE Transactions on Power Electronics*, vol. 24, no. 3, pp. 654–664, March 2009.

[65] M. Liserre, R. Teodorescu, and F. Blaabjerg, "Multiple harmonics control for three-phase grid converter systems with the use of pi-res current controller in a rotating frame," *IEEE Transactions on Power Electronics*, vol. 21, no. 3, pp. 836–841, May 2006.

[66] A. Kuperman, "Proportional-resonant current controllers design based on desired transient performance," *IEEE Transactions on Power Electronics*, vol. 30, no. 10, pp. 5341–5345, Oct 2015.

[67] O. Wallmark, L. Harnefors, and O. Carlson, "Control algorithms for a fault-tolerant pmsm drive," *IEEE Transactions on Industrial Electronics*, vol. 54, no. 4, pp. 1973–1980, Aug 2007.

[68] J. Gao, X. Wu, S. Huang, W. Zhang, and L. Xiao, "Torque ripple minimisation of permanent magnet synchronous motor using a new proportional resonant controller," *IET Power Electronics*, vol. 10, no. 2, pp. 208–214, 2017.

[69] G. Feng, C. Lai, J. Tian, and N. C. Kar, "Multiple reference frame based torque ripple minimization for pmsm drive under both steady-state and transient conditions," *IEEE Transactions on Power Electronics*, vol. 34, no. 7, pp. 6685–6696, July 2019.

[70] M. Hadziselimovic, G. Stumberger, B. tumberger, and I. Zagradinik, "Modeling of permanent magnet synchronous motor in d-q coordinates," vol. 81, pp. 38–42, 01 2005.

[71] A. M. EL-Refaie, "Motors/generators for traction /propulsion applications: A review," in *2011 IEEE International Electric Machines Drives Conference (IEMDC)*, May 2011, pp. 490–497.

[72] C. Lu, S. Ferrari, and G. Pellegrino, "Two design procedures for pm synchronous machines for electric powertrains," *IEEE Transactions on Transportation Electrification*, vol. 3, no. 1, pp. 98–107, March 2017.

[73] M. Morandin, A. Faggion, and S. Bolognani, "Integrated starter-alternator with sensorless ringed-pole pm synchronous motor drive," *IEEE Transactions on Industry Applications*, vol. 51, no. 2, pp. 1485–1493, March 2015.

[74] M. C. Kulan, N. J. Baker, and J. D. Widmer, "Design and analysis of compressed windings for a permanent magnet integrated starter generator," *IEEE Transactions on Industry Applications*, vol. 53, no. 4, pp. 3371–3378, July 2017.

[75] C. Liu, K. T. Chau, and J. Z. Jiang, "A permanent-magnet hybrid brushless integrated starter-generator for hybrid electric vehicles," *IEEE Transactions on Industrial Electronics*, vol. 57, no. 12, pp. 4055–4064, Dec 2010.

[76] C. F. Wang, M. J. Jin, J. X. Shen, and C. Yuan, "A permanent magnet integrated starter generator for electric vehicle onboard range extender application," *IEEE Transactions on Magnetics*, vol. 48, no. 4, pp. 1625–1628, April 2012.

[77] L. Yu, Z. Zhang, and Y. Yan, "Development and analysis of doubly salient brushless dc generators for automobile auxiliary power unit application," in *2013 IEEE Vehicle Power and Propulsion Conference (VPPC)*, Oct 2013, pp. 1–6.

[78] K. W. Hu and C. M. Liaw, "Incorporated operation control of dc microgrid and electric vehicle," *IEEE Transactions on Industrial Electronics*, vol. 63, no. 1, pp. 202–215, Jan 2016.

[79] F. Crescimbini, A. D. Napoli, L. Solero, and F. Caricchi.

[80] F. Gao, X. Zheng, S. Bozhko, C. I. Hill, and G. Asher, "Modal analysis of a pmsg-based dc electrical power system in the more electric aircraft using eigenvalues sensitivity," *IEEE Transactions on Transportation Electrification*, vol. 1, no. 1, pp. 65–76, June 2015.

[81] A. Hasanzadeh, C. S. Edrington, N. Stroupe, and T. Bevis, "Real-time emulation of a high-speed microturbine permanent-magnet synchronous generator using multiplatform hardware-in-the-loop realization," *IEEE Transactions on Industrial Electronics*, vol. 61, no. 6, pp. 3109–3118, June 2014.

[82] P. O. Ohiero, C. Cossar, and J. Melone, "A fast simulation model for a permanent magnet synchronous generator (pmsg) drive system," in *16th European Conference on Power Electronics and Applications (EPE'14-ECCE Europe), 2014*, Aug 2014, pp. 1–10.

[83] M. Rosyadi, A. Umemura, R. Takahashi, J. Tamura, S. Kondo, and K. Ide, "Development of phasor type model of pmsg based wind farm for dynamic simulation analysis," in *PowerTech, 2015 IEEE Eindhoven*, June 2015, pp. 1–6.

[84] W. Meng, X. Wang, Z. Wang, and I. Kamwa, "Impact of causality on performance of phasor measurement unit algorithms," *IEEE Transactions on Power Systems*, vol. PP, no. 99, pp. 1–1, 2017.

[85] S. Hamao, "A physical contradiction in network theory," *IEEE Transactions on Circuits and Systems I: Fundamental Theory and Applications*, vol. 47, no. 11, pp. 1610–1612, Nov 2000.

[86] N. Pogaku, M. Prodanovic, and T. C. Green, "Modeling, analysis and testing of autonomous operation of an inverter-based microgrid," *IEEE Transactions on Power Electronics*, vol. 22, no. 2, pp. 613–625, March 2007.